Searches for resonances decaying to two photons with the ATLAS detector at LHC

Nicolas Berger

LAPP-H-2016-03

Université Grenoble Alpes

Mémoire présenté par

Nicolas Berger

pour obtenir le diplôme de

Habilitation à Diriger des Recherches

Spécialité: Physique des Particules

Searches for resonances decaying to two photons with the ATLAS detector at LHC

Soutenue le 5 juillet 2016 devant le jury composé de :

Fawzi Boudjema	rapporteur
Louis Fayard	examinateur
Andreas Höcker	rapporteur
Jean-Pierre Lees	examinateur
Paraskevas Sphicas	rapporteur
Isabelle Wingerter-Seez	examinatrice

LAPP-H-2016-03

Université Grenoble Alpes

Mémoire présenté par

Nicolas Berger

pour obtenir le diplôme de

Habilitation à Diriger des Recherches

Spécialité: Physique des Particules

Searches for resonances decaying to two photons with the ATLAS detector at LHC

Soutenue le 5 juillet 2016 devant le jury composé de :

Fawzi Boudjema	rapporteur
Louis Fayard	examinateur
Andreas Höcker	rapporteur
Jean-Pierre Lees	examinateur
Paraskevas Sphicas	rapporteur
Isabelle Wingerter-Seez	examinatrice

Contents

Chapter 1

Introduction

The Standard Model (SM) of particle physics is an extraordinarily successful theory of nature, providing accurate predictions for almost all phenomena in high-energy physics. Among the particles which it contains [1], the Higgs boson [2] plays a singular role, being the sole physical manifestation of its scalar sector which through the Brout-Englert-Higgs (BEH) mechanism [3, 2, 4] is responsible for the breaking of electroweak (EW) symmetry.

The discovery of the Higgs boson was one of the main design goals of the LHC accelerator [5], together with the search for new physics at the energy frontier [6]. These twin goals were made possible by the design of the LHC as a machine with both a high nominal collision center-of-mass (CM) energy of $\sqrt{s} = 14$ TeV, more than 7 times that of its predecessor the TeVatron [7], and a very high nominal instantaneous luminosity of $\mathcal{L} = 10\,\mathrm{nb}^{-1}\mathrm{s}^{-1}$ ($\mathcal{L} = 10^{34}\,\mathrm{cm}^{-2}\mathrm{s}^{-1}$). LHC physics prospects could thus benefit from a "no-lose theorem" [8]: either an SM-like Higgs boson is present and would be discovered with about one year's worth of data; or another mechanism for EW symmetry breaking is at work, which would likely lead to the discovery of new physics at the TeV scale on a similar timescale[1]

The ATLAS [10] and CMS [11] detectors were designed as multipurpose experiments to study LHC collisions. The twin aims of Higgs and new physics discoveries require excellent performance both at very high momentum for the new physics and at the relatively low energies of Higgs boson decay products. The problem is especially acute for electromagnetic calorimetry, facing the double requirement of providing excellent mass resolution for the diphoton system of $H \to \gamma\gamma$ decays, as well as excellent performance for multi-TeV electrons from processes such as $Z' \to ee$. In ATLAS, this was resolved thanks to the use of a liquid-argon calorimeter. My contribution to the operation and commissioning of this detector is presented in Chapter 3.

In 2012, the no-lose alternative was resolved with the discovery of a light, SM-like Higgs boson with $m_H \approx 125$ GeV [12, 13] by ATLAS and CMS, using about $10\,\mathrm{fb}^{-1}$ of data collected at collision CM energies of 7 and 8 TeV during Run 1 of the LHC. This marked the triumphal completion of the Standard Model, which led to the attribution of the 2012 Nobel Prize to F. Englert and P. Higgs. Further studies using the full LHC Run-1 dataset showed excellent compatibility of the coupling properties of the new boson with those expected for the SM Higgs boson [14].

The $H \to \gamma\gamma$ mode was long considered as one of the main Higgs discovery modes, thanks

[1] the no-lose theorem was initially stated for the SSC, operating at $\sqrt{s} = 40$ TeV and with $\mathcal{L} = 10^{33}\,\mathrm{cm}^{-2}\mathrm{s}^{-1}$. The lower energy reach of the LHC is largely offset by its higher luminosity, but this would not apply if the onset of new physics was deferred to masses beyond ~ 3 TeV [9]. The "theorem" is therefore not strictly valid at LHC.

to its clean signature and simple backgrounds. The Higgs mass value $m_H \approx 125$ GeV was a fortunate occurrence, as it corresponds to a SM branching ratio close to its maximum value. This led to $H \to \gamma\gamma$ providing the highest discovery potential [15], and the leading role in the discovery of the Higgs boson. My contribution on this mode, which constitutes the central part of my work on ATLAS, is presented in Chapter 6.

The Higgs discovery paradoxically complicates the prospects for the second aim of the LHC physics program, to search for new physics beyond the SM: with $m_H \approx 125$ GeV, the SM could be valid as an effective theory up to the vicinity of the Planck mass [16]. No new physics accessible at LHC is thus required, and even if it is present there are few indications as to where to look. For this reason, new physics searches are increasingly focused on model-independent results over the widest possible range of final states.

In this context, a natural direction of inquiry is the extension of Higgs boson searches to wider mass ranges. These are well-adapted to the search for new bosons, in particular heavy partners of the Higgs boson which constitute a relatively generic feature of many models of new physics. In this context, I contributed to the extension of the $H \to \gamma\gamma$ search to a wide mass range ranging from 65 GeV to about 2 TeV, using data from LHC Runs 1 and 2. This search recently provided hints of a possible excess of events at a mass of about 750 GeV [17], which will be either confirmed or excluded using data collected in 2016. This work is presented in Chapter 8.

Due to the as-yet-unconfirmed nature of the excess at 750 GeV, prospects for 2016 and beyond can be envisaged along two possible alternative paths. If the excess yields a discovery, it will be a more momentous one than that of the Higgs boson itself, and will lead to the opening of a new field of inquiry. Studying the properties of the new resonance, and searching for its possible partners, will then be one of the main physics goals of Run 2 in which the $\gamma\gamma$ mode will play an essential role.

If however the resonance is not confirmed, the study of the Higgs boson will remain on the forefront of the LHC physics program. The search for new physics will continue, both through direct searches, and indirectly through the study of the coupling properties of the Higgs boson. The $\gamma\gamma$ channel will remain one of the strongest contributors to these studies. These prospects are reviewed in Section 9.

Chapter 2

The Standard Model Higgs Boson

2.1 Electroweak symmetry breaking in the Standard Model

The Standard Model (SM) of particle physics describes the ordinary matter content of the universe using fermion fields, and their interactions using gauge interactions. The gauge group is $SU(3)_C \otimes SU(2)_L \otimes U(1)_Y$, with the simple factors associated respectively to color, left-handed isospin and hypercharge. With only these ingredients, all particles are however massless: fermion mass terms are forbidden by the chiral $SU(2)_L$ invariance, while gauge invariance ensures that all the gauge bosons are massless.

The solution to this mass problem is realized through the Brout-Englert-Higgs (BEH) mechanism, put forward in 1964 [2, 3, 4]. This introduces a *scalar* sector consisting of a single complex $SU(2)_L$-doublet scalar field ϕ. The most general renormalizable additions to the SM Lagrangian are

$$\begin{aligned} \mathcal{L}_{Higgs} &= \mathcal{L}_{\text{Kinematic}} + \mathcal{L}_{\text{Potential}} + \mathcal{L}_{\text{Yukawa}} \\ &= |D_\mu \phi|^2 + \left[\mu^2 \phi^2 + \lambda \phi^4\right] + \left[\sum_i y_i \bar{f}_{i,L} \phi^{(c)} f_{i,R}\right] + h.c. \end{aligned} \tag{2.1}$$

where D is an $SU(2)_L \otimes U(1)_Y$ covariant derivative, and the sum in the Yukawa term runs over all fermions [1].

When $\mu^2 < 0$, the true vacuum of the theory occurs for $\langle \phi \rangle = (0, v)$, with $v = \sqrt{-\mu^2/\lambda}$, which breaks $SU(2)_L \otimes U(1)_Y$ invariance down to the electromagnetic $U(1)_{EM}$. The breaking is propagated to the gauge sector via the covariant derivative term, leading to mass terms for the W and Z gauge bosons. These gauge bosons absorb the three components of ϕ associated with the broken degrees of freedom to constitute massive gauge boson fields. The remaining component of ϕ is a massive scalar H, the Higgs boson [2]. The couplings g_V associated with the HVV vertex ($V = W, Z$) are related to the gauge boson masses m_V through the relation

$$g_V = 2\frac{m_V^2}{v}. \tag{2.2}$$

Fermions mass terms are also generated from the Yukawa terms after the symmetry breaking, and the equivalent relation between the coupling associated to the $H\bar{f}_i f_i$ vertex and the masses

[1] we neglect Yukawa mixing effects here

m_{f_i} is

$$g_{f_i} = \sqrt{2}\frac{m_{f_i}}{v} \tag{2.3}$$

In both cases, the couplings of the Higgs bosons to the other SM fields can thus be directly derived from their masses. Among the parameters in Eq. 2.1, the only unknown is the Higgs boson mass $m_H = \sqrt{-\mu^2}$. For this reason, the properties of the SM Higgs boson – production rates, decay branching ratios etc. – are completely determined for a given value of m_H, which was an important input in the design of the LHC search effort.

2.2 Pre-LHC Searches

The Higgs boson has been one of the main search targets of high-energy physics experiments since circa 1980 [18, 19] in spite of the notorious difficulty of such a search [20]. The most stringent pre-LHC direct bound was set by a combination of searches by the four LEP experiments [21, 22, 23, 24], leading to the exclusion of the region $m_H < 114.4$ GeV at 95% CL [25]. Measurements from the TeVatron experiments [26, 27] also led to the exclusion of the mass range $147 < m_H < 180$ GeV [28].

The Higgs mass can also be probed indirectly through quantum corrections to SM observables that involve Higgs boson loops. While the effects are small and the sensitivity to the Higgs mass is weak (typically going as $\log m_H$), they are accessible through the precise measurements of EW observables [29, 30] performed by the SLD experiment [31] and the four LEP experiments, together with measurements of the W boson mass [32] and width [33] performed at the TeVatron. Combined with the bounds from direct searches, this let to the bound $90 < m_H < 300$ GeV at 95% CL [34], illustrated on Fig. 2.1a. Having eliminated most of the parameter space for m_H, these constraints proved critical for the LHC search. Within the small remaining region of m_H, searches could be targeted towards only a few promising signatures, the properties of which were completely determined at a given value of m_H as noted above. This led to a guaranteed result: either the discovery of an SM-like Higgs boson or, more radically, the exclusion of the entire mechanism of EW symmetry breaking described above.

2.2.1 Higgs Production at the LHC

Higgs production at colliders is severely limited by the relation between Higgs couplings and particle masses: while couplings to heavy SM states such as third-generation quarks and W and Z bosons are sizable, direct couplings to ordinary beam particles – first-generation quarks, gluons and electrons – are either extremely small or zero.

The production of Higgs bosons at colliders therefore mainly follows a two-step process: first the creation of heavy states such as W and Z bosons or top quarks; secondly, the emission of a Higgs boson from these states. The simplest process of this type is $f\bar{f} \to WH$ and ZH, in which the Higgs boson is produced through "Higgsstrahlung" off a W or Z boson. A representative diagram[2] is shown in Fig. 2.2c. This process will be referred to as WH and ZH associated production, and collectively as VH. It was the most relevant production process at LEP [25] (as $e^+e^- \to VH$) and TeVatron [28] (as $q\bar{q} \to VH$). The process is however suppressed by electroweak-strength couplings and at LHC by the smaller parton luminosity in the $q\bar{q}$ initial state.

[2] The Feynman diagrams in this document were drawn with the JaxoDraw package [37]

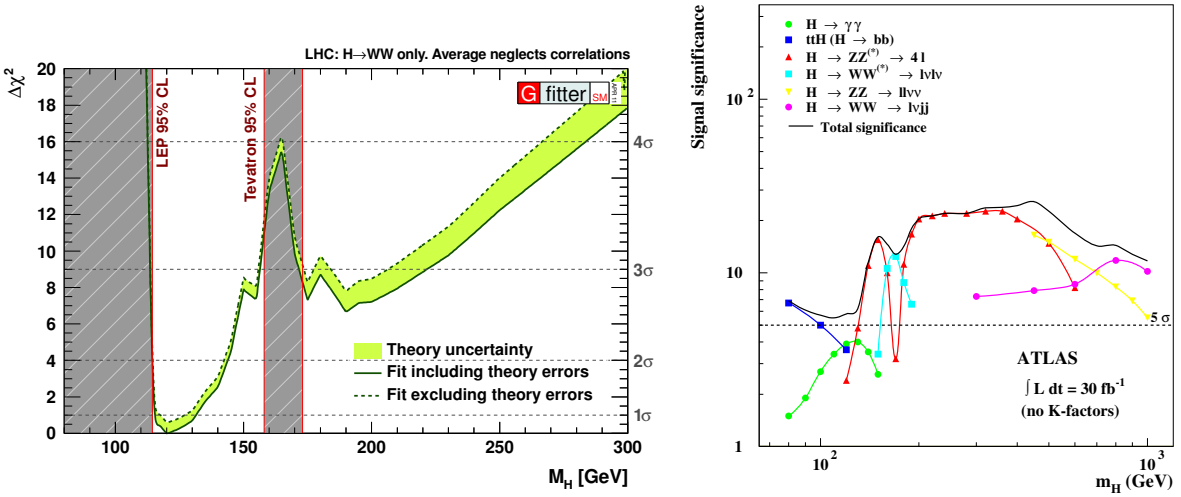

(a) (b)

Figure 2.1: (a) χ^2 scan of m_H from the global fit of SM parameters presented in Ref. [35], using the Gfitter [34] program. (b) Expected discovery significances with 30fb^{-1} of ATLAS data at $\sqrt{s} = 14$ TeV, as estimated in the ATLAS TDR [36] (1999).

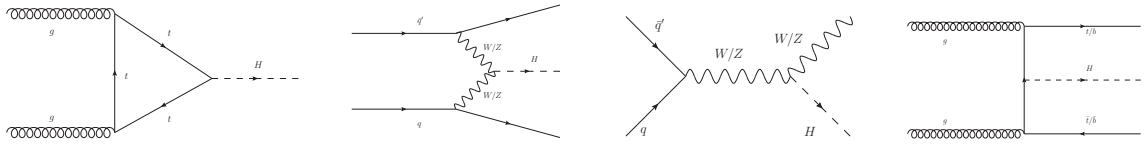

(a) (b) (c) (d)

Figure 2.2: Representative leading-order diagrams for the main SM Higgs production modes at LHC: (a) gluon-fusion, (b) Weak-boson fusion, (c) Associated production with a W and Z boson and (d) Associated production with a $t\bar{t}$ pair

Following a similar strategy, the $t\bar{t}H$ production mode proceeds through the creation of a $t\bar{t}$ pair from which a Higgs boson is radiated, as shown in Fig 2.2d. The process benefits from the large partonic luminosity in the gluon-gluon initial state, and the strong couplings at all interaction vertices. It suffers however from the large phase space required to accommodate two on-shell top quarks as well as the Higgs boson, and its total rate is the smallest of the main production modes. The similar $b\bar{b}H$ mode [38, 39], although initially overlooked in the Higgs search, has a larger cross-section than $t\bar{t}H$, thanks to a larger available phase space and logarithmic enhancements due to the small b-quark mass which more than compensate the smaller Yukawa coupling. It is interesting both for its sensitivity to the bottom-quark Yukawa and as one of the backgrounds to the double-Higgs production $pp \to HH \to \gamma\gamma b\bar{b}$. The b-jets accompanying the Higgs boson are however typically too soft to be reconstructed. In Run-1 analyses, $b\bar{b}H$ was therefore treated as an "untagged" production mode, together with the gluon-fusion mode described below.

The gluon-fusion (ggF) mode, shown in Fig. 2.2a, also proceeds through the creation of heavy quarks, but within a loop. This provides the same strong couplings as for $t\bar{t}H$, but without the phase-space suppression. It suffers from a loop suppression, but is nevertheless the largest production mode at LHC by more than an order of magnitude. The loop is also potentially sensitive to the presence of new heavy particles that cannot be produced directly.

Finally, the t-channel process shown in Fig. 2.2b, referred to as Weak Boson Fusion or VBF [3] [40] is also significant at LHC energies. It is mainly mediated by longitudinally-polarized gauge bosons, with an emission probability that rises with $\sqrt{s}$ [41]: while its contribution was relatively small at the TeVatron, it is sizable at LHC, where it is the second most abundant production mode after gluon-fusion [42]. Furthermore, it is characterized by the presence of forward jets initiated by the radiating quarks. The jets are separated by a large rapidity gap ($\Delta y \gtrsim 4$) featuring little hadronic activity, due to the lack of color exchange between the quarks. This distinctive signature can be used to achieve much larger signal-over-background ratios after selection.

Fig. 2.3a shows the production cross-sections for the various modes as a function of m_H.

2.3 Higgs decay modes

The branching fractions for the main Higgs boson decay modes are shown in Fig. 2.3b. For $m_H \approx 125$ GeV, the main decay modes are into pairs of heavy SM particles: $H \to b\bar{b}$, $H \to WW$, $H \to ZZ$ and $H \to \tau\tau$, with branching fractions ranging from 58% to 6.3%. These abundant modes are however difficult to access inclusively at hadron collider due to large backgrounds from QCD processes.

The $H \to WW$ and $H \to ZZ$ can be identified using leptonic decays[4], but this reduces the event rate by factors of about 20 and 200 respectively for the fully leptonic case. In the case of $H \to WW$, the presence of neutrinos in the final state also leads to poor resolution on the mass of the WW system, which makes the extraction of the signal challenging. The $H \to b\bar{b}$ and $H \to \tau\tau$ final states can be accessed in particular configurations: using the presence of an associated W or Z boson decaying to leptons or a $t\bar{t}$ pair, a VBF-like configuration, or a

[3] The acronym originates from the ambiguous denomination of "Vector Boson Fusion", which has unfortunately become the standard usage

[4] Here *leptonic* refers to e and μ only, since hadronic τ decays are more difficult to separate from QCD processes

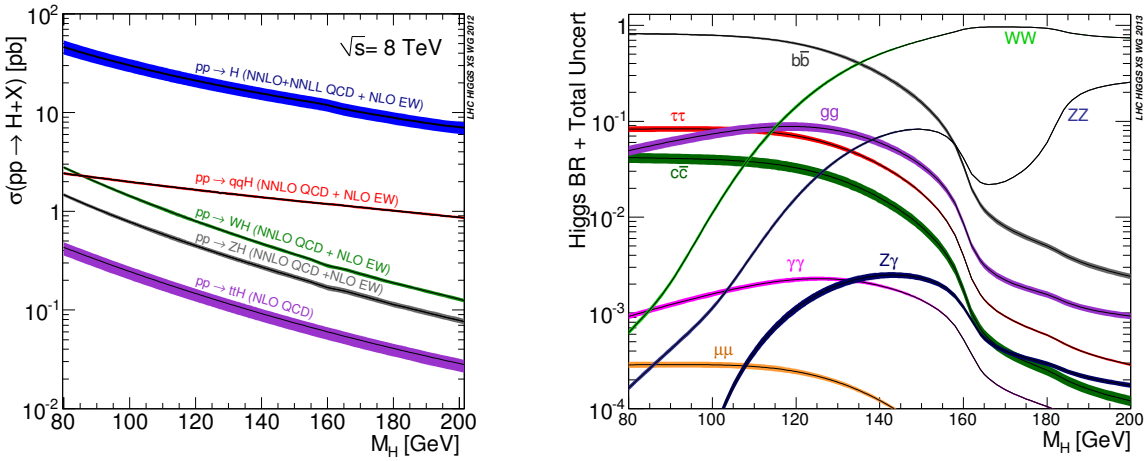

(a) (b)

Figure 2.3: (a) Higgs production cross-sections as a function of $m_H$and (b) Higgs decay branching ratios as a function of m_H

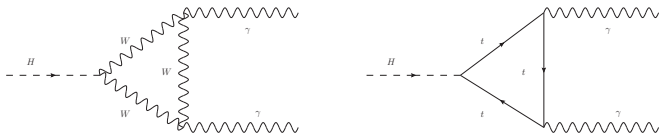

(a) (b)

Figure 2.4: Representative leading-order diagrams for $H \to \gamma\gamma$: (a) through a W-boson loop, (b) through a t-quark triangle.

"boosted" configuration with a large Higgs transverse momentum. The dominant gluon-fusion production yield is however largely inaccessible.

By comparison, the $H \to \gamma\gamma$ mode is a rather rare decay, proceeding through the loop diagrams shown in Fig. 2.4. Its highest branching ratio is only about 0.23% for $m_H \sim 125$ GeV [42], and furthermore it drops rapidly as one moves away from this value: the partial decay width scales approximately as m_H^3, and thus decreases rapidly for lower m_H; and for $m_H \gtrsim 130$ GeV, the total width is dominated by the rapidly-rising $H \to WW$ and $H \to ZZ$ partial widths, leading to the drop in the $\gamma\gamma$ branching ratio seen in Fig. 2.3b.

The $H \to \gamma\gamma$ mode however offers two main advantages. First, most of the event yield is accessible: photons do not suffer branching fraction losses, so that the accessible event yield is about 20 times larger than $H \to ZZ \to 4l$ and only about 4 times smaller than $H \to WW \to l\nu l\nu$. The clean diphoton final state allows the use of the full gluon-fusion production yield, in addition to less-abundant production processes. This possibility to access all of the main production modes was important not just for discovery, but also for the later measurement of Higgs boson couplings. Secondly, the signal can be clearly identified as a narrow peak in the diphoton invariant mass ($m_{\gamma\gamma}$) distribution. For $m_H \approx 125$ GeV, the total width of the Higgs boson is $\Gamma_H = 4$ MeV, so that the width of the mass peak is dominated by the experimental mass resolution of about 1%. Minimizing this resolution was therefore an important design parameter

of the LHC experiments. This is particularly important due to the large irreducible backgrounds in this channel (see Section 4), which can however be cleanly separated from the signal due to the smoothness of their $m_{\gamma\gamma}$ distributions.

2.4 Search Strategy

At LHC, the very large yield from gluon-fusion production led to a discovery strategy focused on this production mode, relying on clean signatures from the Higgs decay itself to suppress background. The most promising discovery channels were thus $H \to ZZ \to 4l$ or $H \to WW \to l\nu l\nu$ decays, and of course the $H \to \gamma\gamma$ mode which will be the focus in the rest of this document. The $VH \to b\bar{b}$ mode, while extremely interesting to probe the b-quark Yukawa coupling, had a sensitivity that is restricted to Higgs masses very close to the LEP bound. This picture of the main discovery modes, as envisaged at the time of the design of the ATLAS experiment, is shown in Fig. 2.1b.

As noted above, the coupling properties of the SM Higgs boson are completely defined once its mass m_H is known. If an excess is observed at a given mass m_H, one can compute the Higgs *signal strength* as the ratio

$$\mu = N_{evts}^{obs}/N_{evts}^{SM} \tag{2.4}$$

of the observed event yield in a given process to the one predicted by the SM. Values close to unity then serve as evidence of the Higgs-like nature of the excess. Higgs discovery and exclusion results are generally presented in terms of μ: the exclusion of the SM is evidenced by upper limits on μ below unity, while exclusion of $\mu = 0$ at the 5σ level constitutes a discovery.

Chapter 3

The ATLAS detector

3.1 Overview

The ATLAS detector is a multi-purpose particle detector with a cylindrical geometry and approximate forward-backward symmetry, providing almost 4π solid angle converge around the interaction point. It consists in an inner tracking detector, electromagnetic and hadronic calorimeters, and a muon spectrometer. The tracker is composed of a silicon pixel detector, a silicon-strip tracker (SCT) and a transition radiation tracker (TRT) consisting of straw drift tubes filled with xenon gas. It is surrounded by a solenoid magnet generating a 2T axial magnetic field and provides track reconstruction within the region $|\eta| < 2.5$[1]. During the shutdown period between LHC Run 1 and Run 2, a new innermost layer, the *insertable b-layer* (IBL) was added to the Pixel detector [43]. Electromagnetic calorimetry in the region $|\eta| < 3.2$ is provided by a sampling calorimeter with an accordion geometry, using liquid-argon (LAr) as the sensitive medium and lead as the absorber. It consists of a barrel section covering the range $|\eta| < 1.475$ and two endcaps covering $1.375 < |\eta| < 3.2$. A scintillating tile/iron calorimeter provides hadronic calorimetry over the range $|\eta| < 1.7$. LAr calorimeters with copper and tungsten absorbers provide electromagnetic and hadronic calorimetry in the forward region. Both hadronic and electromagnetic calorimeters cover the range $|\eta| < 4.9$. The muon spectrometer consists of an array of precision tracking chambers within a magnetic field provided by a set of air-core toroidal magnets arranged in an octagonal geometry. It provides muon tracking over the range $|\eta| < 2.7$. A detailed description of the ATLAS detector can be found in Ref. [10].

3.2 The ATLAS Liquid-Argon Calorimeter

3.2.1 Overview

The main design goal of the ATLAS electromagnetic calorimeter was to provide good identification and measurement of photons and electrons over a wide range of energies running from a few GeV to a few TeV [44]. One of the main physics targets for this design was $H \to \gamma\gamma$. These

[1] The ATLAS experiment uses a right-handed coordinate system with its origin at the nominal interaction point (IP) in the center of the detector and the z-axis along the beam pipe. The x-axis points from the IP to the center of the LHC ring, and the y-axis points upward. Cylindrical coordinates (r, ϕ) are used in the transverse plane, ϕ being the azimuthal angle around the beam pipe. The pseudorapidity is defined in terms of the polar angle θ as $\eta = -\ln\tan(\theta/2)$.

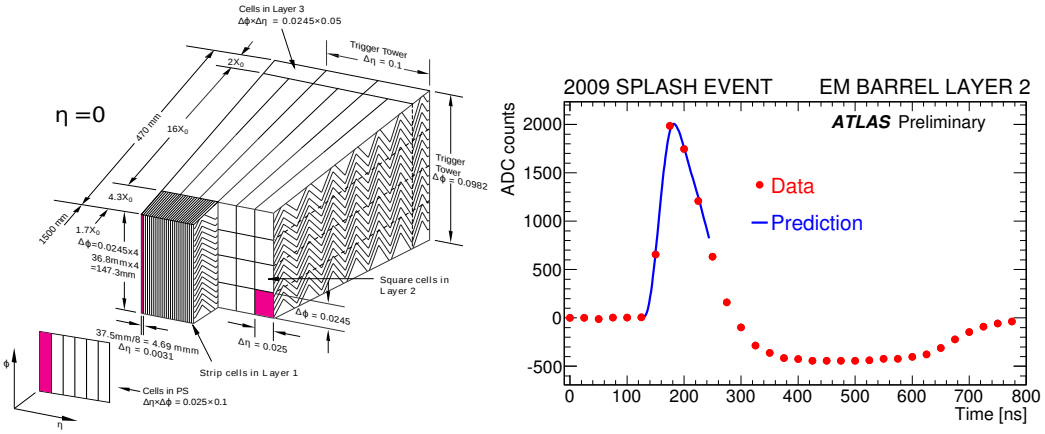

(a) (b)

Figure 3.1: (a) Schematic view of a section of the barrel EM calorimeter, illustrating its longitudinal and transverse segmentation. (b) An example pulse shape collected in the second layer of the EM barrel. The red points show the samples and the blue line the pulse shape prediction.

objectives are achieved using a lead/liquid-argon (LAr) sampling calorimeter covering the pseudorapidity range $|\eta| < 4.9$. The LAr technology was chosen since it provides a stable and uniform detector response, allowing precise calibration of the energy of electromagnetic objects. It also provides excellent radiation hardness, which is critical in the demanding environment of the LHC. The calorimeter is separated into a barrel covering $|\eta| < 1.475$, and endcap sections consisting of an outer wheel covering $1.375 < |\eta| < 2.5$ and an inner wheel covering $2.5 < |\eta| < 3.2$. In the region $|\eta| < 2.5$, designed for precision electromagnetic calorimetry, the LAr calorimeter is segmented into three longitudinal layers, as shown in Fig. 3.1a. The second layer has a thickness of approximately $24X_0$ and collects most of the electromagnetic shower energy. It is finely segmented into cells of 0.025×0.025 along η and ϕ, allowing the separation of electromagnetic and hadronic showers through their shapes. The first layer has a thickness of about $4X_0$ and is very finely segmented into cells of size 0.003125 along η. These fine *strips* provide discrimination between the single showers created by prompt photons from the two overlapping showers created by $\pi^0 \to \gamma\gamma$ decays. The third layer is used to collect the tail of the EM shower and correct for leakage beyond the EM calorimeter. A presampler detector covering the range $\eta < 1.8$ is also used to account for energy losses upstream of the calorimeter. The fine segmentation of the first layer is present only in the region $|\eta| < 2.37$. Performance is degraded in the region near the barrel-endcap transition at $\eta = 1.4 - 1.5$ due to larger amounts of material in front of the calorimeter, as shown in Fig. 4.4a, and the region $1.37 < |\eta| < 1.52$ is generally not used in analysis.

3.2.2 Measurement of Cell Energy and Time

In each of the 182,458 cells in the LAr calorimeter, the ionization signal created by the passage of charged particles through the LAr is processed by an electronics chain consisting of a preamplifier and a bipolar filter, as shown in Fig. 3.2. The linearly decreasing shape of the ionization signal as a function of time is then shaped into the form shown in Fig. 3.1b. The shape is then sampled at 25 ns intervals in one of three possible gains (low, medium or high). After pedestal subtraction,

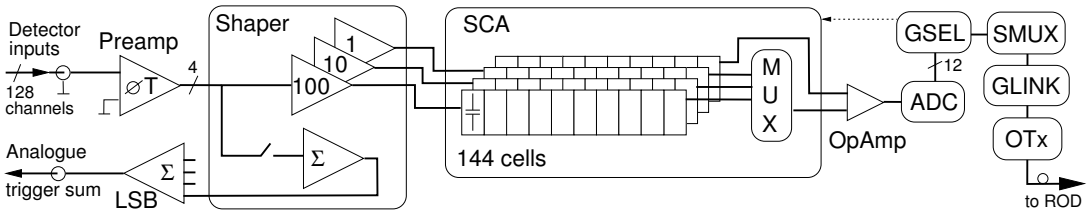

Figure 3.2: Schematic view of the LAr front-end electronics

the digitized sample values can be expressed as

$$s^i = Ag(t^i + \tau) + n_i \approx Ag^i + A\tau g'^i + n^i \tag{3.1}$$

where $g(t)$ is the pulse shape; t^i are the sampling times; $g^i = g(t^i)$ and $g'^i = g'(t^i)$ are the values of the pulse shape and its time derivative at the sampling points; A and τ are the amplitude and the time of the pulse; and n^i is the random noise at sampling i. The pulse shapes $g(t)$ are obtained for each cell and gain value using a calibration procedure [45]. If the linearized form of Eq. 3.1 is valid (*i.e.* for $|\tau|$ small compared to the scale of the variations of $g(t)$), the amplitude and time can be computed using the optimal filtering (OF) expressions [46]

$$A = a_i s^i \tag{3.2}$$

$$A\tau = b_i s^i \tag{3.3}$$

where the implicit sums run over N samples ($N = 5$ in Run 1 and $N = 4$ in Run 2). The a_i and b_i are optimal filtering coefficients (OFCs) chosen to minimize the noise contribution to A and $A\tau$. Their expressions can be obtained from the linear least squares technique in a non-orthonormal basis as [47]

$$\begin{pmatrix} a_i \\ b_i \end{pmatrix} = \Gamma^{-1} \begin{pmatrix} g_i \\ g'_i \end{pmatrix}, \tag{3.4}$$

where

$$\Gamma = \begin{pmatrix} g_k g^k & g_k g'^k \\ g_k g'^k & g'_k g'^k \end{pmatrix}. \tag{3.5}$$

The metric used to raise and lower indices is the inverse of the noise correlation matrix $C_{ij} = \bar{n}^{-2}\langle n_i n_j \rangle$, where $\bar{n}^2 = \langle n_i^2 \rangle$ the noise RMS at each sampling.

3.2.3 Quality Factor Calibration

The *Q-factor* [48] of the pulse is defined as

$$Q = \frac{1}{\bar{n}^2} r_i r^i, \qquad r^i = s^i - Ag^i - A\tau g'^i. \tag{3.6}$$

or alternatively in an un-normalized form without the $\bar{n}^2$ denominator. It is a measure of the goodness-of-fit of the measured samples to the expression given by Eq. 3.1, and allows to reject pulses originating from noise, rather than true ionization signals. If the true values of g^i and g'^i are used throughout the computations above, then the estimators given by Eqs. 3.2 and 3.3 are unbiased. In this case, Q only gets contributions from noise terms and is distributed as a χ^2 with $N - 2$ degrees of freedom if the noise is assumed to be Gaussian.

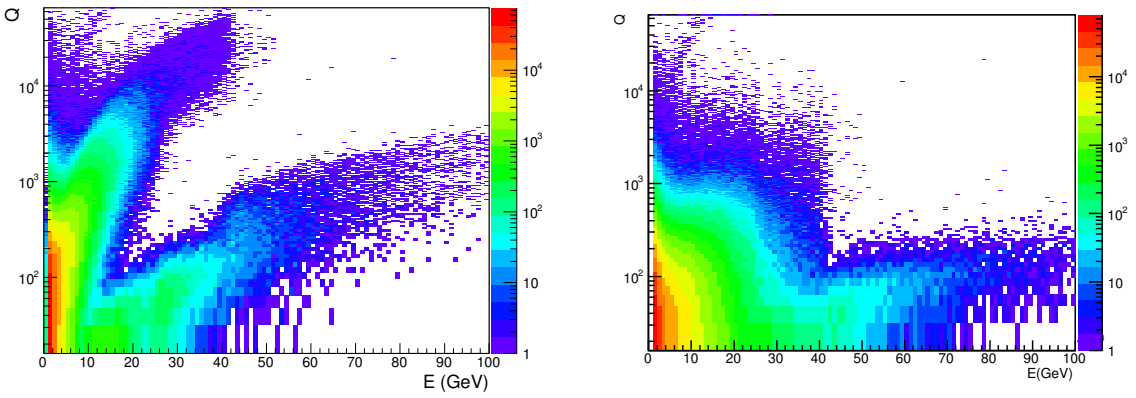

(a) (b)

Figure 3.3: Un-normalized Q-factor values as a function of measured energies for pulses collected in cells from well-identified electron clusters in 300pb^{-1} of 2011 data (a) before the corrections of Section 3.2.3 and (b) with the corrections applied. The correlations between Q values and energy visible in (a) are due to biases in the pulse shapes used in the reconstruction, as described in the text; the two lobes correspond to high gain (top) and medium gain (bottom).

The distribution of the un-normalized Q in data was measured in a sample of about 300 pb^{-1} of data collected in 2011, in cells taken from the electromagnetic clusters of well-identified electrons (see Ref. [47]). The result is shown in Fig. 3.3a: large values of Q are observed, correlated with large pulse amplitudes. Due to this behavior, even good pulses can be associated with large Q factor values. A cut at $Q > 4000$ was initially set on pulse Q-values to reject noise, but as seen in Fig. 3.3a this led to significant inefficiencies for good pulses with large amplitudes.

This behavior is incompatible with a χ^2 distribution for Q, but expected if the shape coefficients g^i and g'^i used in the computation differ from the true values $\hat{g}^i$ and $\hat{g}'^i$; in this case Q also receives contributions quadratic in $A(g^i - \hat{g}^i)$, as well as other similar contributions involving g'.

In order to recover an appropriately distributed Q-factor, one can simply measure these deviations using the *pseudo-residual* [48] expression

$$\rho^i = \frac{s^i - Ag^i - A\tau g'^i}{A}. \tag{3.7}$$

Pulse corrections can then be derived from the averages of the pseudo-residuals as

$$\xi'^i = -\frac{\left\langle \left[\rho^i - \langle\rho^i\rangle\right]\left[\tau - \langle\tau\rangle\right]\right\rangle}{\left\langle \left[\tau - \langle\tau\rangle\right]^2\right\rangle} \tag{3.8}$$

$$\xi^i = \langle\rho^i\rangle + \langle\tau\rangle\xi'^i. \tag{3.9}$$

and one can show [47] that using the corrected pulse shape coefficients $\tilde{g}^i = g^i + \xi^i$ and $\tilde{g}'^i = g'^i + \xi'^i$ instead of the original g^i and g'^i, one recovers a χ^2 behavior for Q. This represents a generalization to two dimensions of the method of Ref. [48] for the case of the measurement of the amplitude only.

These corrections must be separately computed for each sampling of each LAr cell and for each gain value, since different gains follow different electronics channels (see Fig. 3.2) which may lead to slightly different pulse shapes, leading to a potential total of 6M correction values.

Corrections were computed using a subset of 2011 data [47] collected using a dedicated trigger stream. The *partial event building* readout mode was used in which only the part of the event close to the region of interest flagged by the trigger is read out. Thanks to the small resulting event size, this technique allows the collection of LAr pulses to occur at trigger rate of about 40 Hz, which would not be possible for standard triggering techniques.

For the method outlined above to work reliably, about 20 pulses must be collected in a given cell. Even with the use of the dedicated trigger stream described above, a sufficient number of pulses could not be collected for the method to be applied reliably in all LAr cells, particularly in low gain and in the third layer of the calorimeter. For these cases, a separate set of corrections was derived from all pulses in cells at a given ϕ positions, for which shapes are expected to be quite similar. While these corrections are less precise than the per-cell values, excellent agreement is found between the two, for the cells in which both values are available [47].

The Q factor computed after applying these corrections is shown in Fig. 3.3b, on the same electron sample as described above. The amplitude-dependent behavior was largely removed by the correction, leading to an inefficiency of less than 1% when applying the $Q > 4000$ selection on good physics pulses.

3.3 Photon Reconstruction and Identification

3.3.1 Photon Reconstruction

Photons are reconstructed as clusters of cells in the EM calorimeter using a sliding-window technique within the region $|\eta| < 2.5$. Tracks are associated to the cluster if their extrapolated intersection point with the second layer of the calorimeter is consistent with the position of the cluster. Clusters associated with a single track with no hit in the innermost tracking layer are classified as *single-track conversion* candidates. Clusters associated with a pair of tracks consistent with originating from a photon conversion in the inner tracker are classified as *double-track conversions*. Other photons are classified as *unconverted*. A final algorithm resolves the ambiguity for candidates reconstructed both as electrons and as photons, and recovers unconverted photons that were wrongly reconstructed as electrons due to the presence of a spurious track. From MC simulations 96% of photons with $E_T > 25$ GeV are expected to be reconstructed as photon candidates, while the remaining 4% are incorrectly reconstructed as electrons [49].

The probability for a real electron with $E_T > 25$ GeV to be reconstructed as a photon candidate fulfilling the tight identification criteria is measured in data to vary between 2% and 15%, depending on its pseudorapidity and whether the photon candidate is reconstructed as converted or unconverted.

3.3.2 Photon Identification

Photons identification is a set of selections designed to separate prompt photons from background sources, in particular photons from hadronic decays (e.g. $\pi^0 \to \gamma\gamma$ and $\eta \to \gamma\gamma$). The selections are based on the shape of the shower developments within the calorimeters in both the longitudinal and transverse directions, making use of the segmentation of the calorimeter

along both directions. As described in Section 3.2.1, only photons in the pseudorapidity range $|\eta| < 2.37$, excluding the barrel-endcap transition region $1.37 < |\eta| < 1.52$ are considered. The shape is characterized by 9 shape variables that fall into three broad categories:

- Hadronic leakage: fraction of photon energy reconstructed in the hadronic calorimeter
- Width of the shower in the second layer of the EM calorimeter along the η and ϕ directions.
- Shape of the shower in the first layer of the EM calorimeter. This includes measures of both the width of the shower and of the presence of two local energy maxima. The latter may be used to identify $\pi^0 \to \gamma\gamma$ decays.

For Run 1 data collected in 2012 and Run 2 data, the selection is applied through rectangular cuts on the shower shape variables.

In early Run 1 data, the efficiency of these selections was determined from simulation. The corresponding uncertainties were determined based on the agreement between data and simulation in the distributions of the shower shape variables, as measured in photon samples. Typical values of 5% were obtained. The same method is used for the Run 2 data.

For the final 2012 dataset, efficiencies were determined from three data-driven methods: using a clean sample of photons from $Z \to ll\gamma$ decays; extrapolating photon shower shape properties from that of $Z \to ee$ electrons; and a method using an inclusive photon sample in which the relatively low photon purity is measured from data using photon isolation properties [49]. Scale factors determined from these methods are then applied to the simulation to match the measurements in data. The methods cover a range of photon energies ranging from 15 GeV up to 1 TeV, with typical uncertainties of about 1%. For the $H \to \gamma\gamma$ analysis of 2011 data, the identification was based on a combination of shower shape variables within a neural network [49].

Further separation of prompt photons from background is provided by estimating the amount of activity in a wide cone around the photon candidate position. Two methods are used for this purpose:

- Calorimeter-based isolation criterion: the isolation transverse energy $E_{T,iso}$ is computed as the scalar sum of the transverse energies of clusters within a cone of radius $\Delta R = 0.4$ around the position of the photon candidate, removing the energy from the photon cluster itself. A correction for photon cluster leakage into the isolation cone is applied, as well as an event-by-event correction of the event ambient energy based on the method of Refs. [50, 51]. In Run 1 data, the selection $E_{T,iso} < 6$ GeV is applied. In Run 2, the selection is $E_{T,iso} < 2.45$ GeV $+ 0.022\, E_T$, where E_T is the transverse momentum of the photon candidate.
- Track-based isolation criterion: the isolation transverse momentum $p_{T,iso}$ is computed as the scalar sum of the p_T of all tracks within a cone of radius $\Delta R = 0.2$ which originate from the selected primary vertex (see Section 3.3.3) and have $p_T > 1$ GeV. In Run 1 data, the selection $p_{T,iso} < 2.6$ GeV is applied. In Run 2, the selection is $p_{T,iso} < 0.05\, E_T$, where E_T is the transverse momentum of the photon candidate.

3.3.3 Diphoton Mass Reconstruction and Calibration

The energy of the photon candidate is computed from the energies of the cells within the cluster, applying a calibration procedure accounting for upstream material and lateral and longitudinal

leakage. Slightly different procedures were used for different phases of the $\gamma\gamma$ analyses: the early Run 1 results used what will be referred to as the *initial Run 1 calibration* [52], while later Run 1 analyses used the more precise *final Run 1 calibration* [53]. In the latter scheme, both the photon energy resolution and its uncertainty were reduced, in particular thanks to more precise estimations of the amount of upstream material and of the relative energy calibration of the first and second layers of the EM calorimeter. These estimations also formed the basis of the preliminary calibration available for the Run 2 data.

The invariant mass of the two photons is computed as $m = \sqrt{2E_{T,1}E_{T,2}\left(\cosh\Delta\eta - \cos\Delta\phi\right)}$ where $E_{T,1}$ and $E_{T,2}$ are the transverse momenta of the two photons, and $\Delta\eta$ and $\Delta\phi$ the respective differences in their pseudorapidities and azimuthal angles.

The invariant mass depends on the position of the primary vertex, through the value of $\Delta\eta$. This can be obtained by an extrapolation from the positions of the barycenters of the photon clusters in the first and second layers of the EM calorimeter. This *pointing* information for both photons is combined through a multivariate discriminant, together with information from the primary vertices reconstructed in the inner tracker and their associated tracks, and photon conversion tracks when they are present. The position of the selected vertex is within 0.3 mm of the true vertex 95% of the time, as determined from $Z \to ee$ events. This resolution is sufficient to ensure that the effect of the choice of diphoton vertex has a negligible impact on the mass resolution.

In the initial Run 1 calibration, the uncertainty on the mass scale for the inclusive $H \to \gamma\gamma$ analysis was 0.55% [54]. For the final Run 1 calibration, the corresponding number was 0.2% [55]. The uncertainty on the mass resolution similarly decreased from 21% for the initial calibration [56] to 11% for the final calibration [55].

3.3.4 Photon Trigger

Events used in the analyses described in this document are selected using diphoton triggers with energy thresholds of either 20 GeV both both photons, or 35 GeV and 25 GeV for the leading and subleading photon respectively[2]. These triggers are fully efficient for offline energies a few GeV above the trigger thresholds. Looser versions of the photon identification criteria presented in Section 3.3.2 are also applied. In all cases, the trigger efficiency on selected analysis events is about 99% or higher.

3.3.5 Personal Contributions

I developed the method presented in Section 3.2.3 to compute the pulse shape corrections to both g^i and g'^i, extending the technique of Ref. [48] for the correction of g^i. I developed a software package, `LArSamplesMon` [57] to implement the calculation. I also implemented the trigger stream through which the pulses are collected, helping to commission the partial event building technique which it uses. I also developed software, implemented in the `LArCafJobs` [58] package, to automatically process the collected data. This processed data was used not only in the computation of pulse residuals, but also to perform the timing alignment of the LAr cells for the Run 1 data-taking [59].

[2] Here and in the rest of this document, *leading* and *subleading* refers to an ordering with respect to transverse momentum.

I contributed to the development of the High-level trigger (HLT) steering code, the framework which schedules the execution of the HLT algorithms. The development occurred in 2006-2007, and this code is still in use today in the trigger. Since October 2015 I am supervising the work of a student working on the photon trigger algorithms.

Finally, I have been co-convener of the ATLAS photon identification group since April 2015, overseeing in particular the development of the data-driven determinations of the photon identification efficiencies in Run 2 data.

Chapter 4

Strategy for the $H \to \gamma\gamma$ Search

4.1 Introduction

In the mass range near $m_H = 125$ GeV where the $H \to \gamma\gamma$ branching ratio is maximal, the SM Higgs boson manifests itself as a narrow resonance, with a rather large event yield of about 19 identified events per fb^{-1} [12], providing an ideal setting for discovery.

These advantages are however offset by large backgrounds: after applying the photon selection criteria described in Section 3.3.2, the total background yield at $m_{\gamma\gamma} = 125$ GeV is about 170 events per fb^{-1} and per GeV of $m_{\gamma\gamma}$ [12], resulting in a signal-over-background ratio (S/B) of only about 3% at the peak. This background is partially due to reducible contributions from single-photon production (referred to as γjet in the following) and multijet events (henceforth denoted as jetjet). In these cases a jet is misidentified as a photon, most often due the presence of a high-momentum $\pi^0 \to \gamma\gamma$ decay which is not rejected by the photon identification cuts. However this reducible background only makes up about $20-25\%$ of the total [55], as illustrated in Fig 4.2. The remainder originates from $q\bar{q} \to \gamma\gamma$ and $gg \to \gamma\gamma$ processes, denoted as $\gamma\gamma$ in the following. The gluon-initiated process contributes about 15% of the total $\gamma\gamma$ yield at $m_{\gamma\gamma} = 125$ GeV [60]. Representative diagrams for the leading background processes are shown in Fig. 4.1.

The $\gamma\gamma$ background can be reduced by targeting non-ggF production, for instance requiring VBF-like jet configurations or the presence of gauge bosons or heavy $q\bar{q}$ pairs in the event. This can achieve sizable increases in the S/B to about 0.30. However such requirements lead to a much reduced discovery potential, due to the dominance of ggF production at LHC. The $\gamma\gamma$ background is thus largely irreducible, although one can still make use of regions with higher

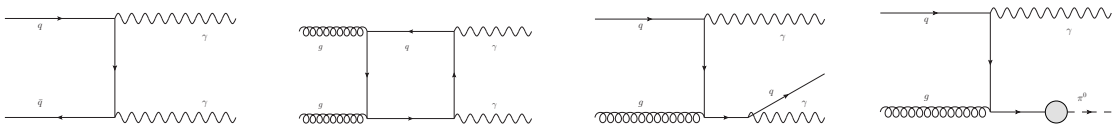

(a) (b) (c) (d)

Figure 4.1: Representative leading-order diagrams for the main backgrounds to $H \to \gamma\gamma$ at LHC (a) direct $\gamma\gamma$ production, (b) box diagram for $\gamma\gamma$ production (c) $\gamma\gamma$ production through internal bremsstrahlung (d) γjet production

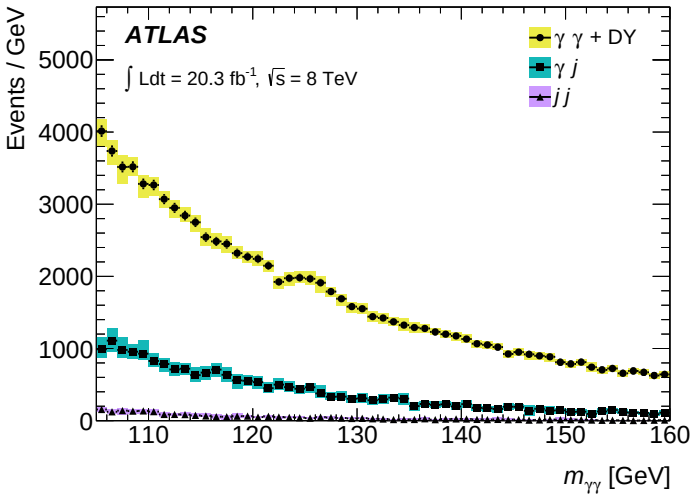

Figure 4.2: Decomposition of the background to the $H \to \gamma\gamma$ search into $\gamma\gamma$, γjet and jetjet components, for the selection of the final Run 1 analysis described in Section 7.

S/B using categorization techniques as described in Section 4.4 below.

The $m_{\gamma\gamma}$ spectrum of the background is however smooth, due to the absence of production thresholds between the low-energy QCD region and the $t\bar{t}$ threshold[1] The signal can therefore be extracted by making use of the wide sidebands available in the $m_{\gamma\gamma}$ spectrum to estimate the background below the narrow signal peak.

The full-scale implementation of these techniques in ATLAS was first performed in the $H \to \gamma\gamma$ analysis published in 2008 as part of the "CSC document" [15], a full review of ATLAS physics performance. This iteration of the $H \to \gamma\gamma$ analysis will be referred to as the *CSC analysis*.

The techniques used in modeling the background are further described in Section 4.2 below, while Section 4.3 presents the modeling of the signal. The use of categorization to improve the analysis sensitivity is presented in Section 4.4.

4.2 Background Modeling

4.2.1 Modeling Using Analytical Shapes

The sideband regions used to estimate the background in the Higgs discovery analysis covers the range $100 < m_{\gamma\gamma} < 160$ GeV. The lower edge was chosen as the point where the small background contribution from misidentified $Z \to ee$ events ($\sim$1% of the total [12]) can be considered together with the other background components, without special treatment of the Z resonance. The upper edge was chosen so that a signal peak in the expected region $120 < m_H < 140$ GeV lies approximately in the center of the mass range. The value is also close to the optimum value obtained when accounting for two competing effects: on the one hand, the increase in statistical uncertainty when the mass range is reduced; and on the other hand, the increase in the background modeling uncertainty when the mass range is widened.

[1] the $t\bar{t}$ threshold has a small impact on the $\gamma\gamma$ shape, for instance through higher-order corrections to the $gg \to \gamma\gamma$ "box" process [61].

In many ATLAS analyses, the shapes used to model the background components are described using "templates", histograms obtained from MC simulation. The shape of these templates is usually fixed in the fit to the data, modulo some flexibility accounting for shape uncertainties. This technique is however ill-suited to the case of $H \to \gamma\gamma$: firstly, theory systematic uncertainties on the shape of the $m_{\gamma\gamma}$ spectrum are typically of the order of a few percent for the latest computations at next-to-next-to-leading order (NNLO) [62]. For $S/B \approx 3\%$, these uncertainties are of the same order as the signal itself. Secondly, achieving sufficiently small *statistical* uncertainties on the background requires large simulated samples, given the small S/B. Achieving a statistical precision of δ relative to the signal yield, requires a sample size that can be estimated as $B \approx \frac{\Delta}{\sigma}\left[\delta\left(\frac{S}{B}\right)\right]^2$, where σ is the width of the signal peak and Δ the width of the sideband. For δ of the order of a few percent, samples of $O(10^7)$ events are required. This is achievable for $\gamma\gamma$ production, for which the selection efficiency is high. For γjet and jetjet production however, the selection efficiency is suppressed by the small probability to misidentify a jet as a photon, which is $O(10^{-3})$, and the required samples would be unreasonably large. Templates for the reducible backgrounds also cannot be easily obtained from data control regions, since even relaxing the photon selections to the ones used at the trigger level still leads to statistical fluctuations in the template that are not small compared to the expected signal (again due to the small S/B).

Since the background follows a simple smooth shape, one can instead rely on an ad-hoc description using a smooth function of $m_{\gamma\gamma}$, in practice an analytical[2] function. The wide and well-populated sidebands can be used to fit the parameters of the function, which are left free in the fit. The shape of the background is thus almost entirely data-driven: the systematic uncertainties associated with the template method above are replaced with statistical uncertainties, typically very small given the large event yields available in the sideband regions.

4.2.2 Choice of Function

The background shape is not fully flexible due to the specific choice of analytical form. This limited flexibility is unavoidable, since the interpolation of the background from the sideband region into the signal region necessarily relies on assumptions on the smoothness of the distribution[3]. However this can also induce a bias in the estimation of the background below the peak, whose effect on the signal is magnified by the small S/B ratio. This bias can be made smaller with more complex (and therefore more flexible) functional forms but at the price of lower statistical power.

The bias can be estimated using large samples of simulated background. These are fitted to a model consisting of the sum of a background component defined by the functional form under study, and a signal component defined as described in Section 4.3 below. The fitted number of signal events is a measure of the bias induced by the difference between the simulated $m_{\gamma\gamma}$ shape and that provided by the functional form. Since the result depends on the $m_{\gamma\gamma}$ shape predicted by the simulation, the method should in principle be applied using various generator choices. One should also consider variations in the renormalization and factorization scales, to account for missing higher-order terms in perturbative expansions, and appropriate variations of the parton distribution functions. Each of these configurations yields a different $m_{\gamma\gamma}$ shape, but due to the freedom provided in the background parameterization, a suitably low value of the bias

[2] In this context *analytical* will here denote a function that is not only analytical in the usual sense, but also expressible in closed form using usual functions.

[3] In the extreme case of a fully flexible function, any signal peak would be absorbed in the background shape.

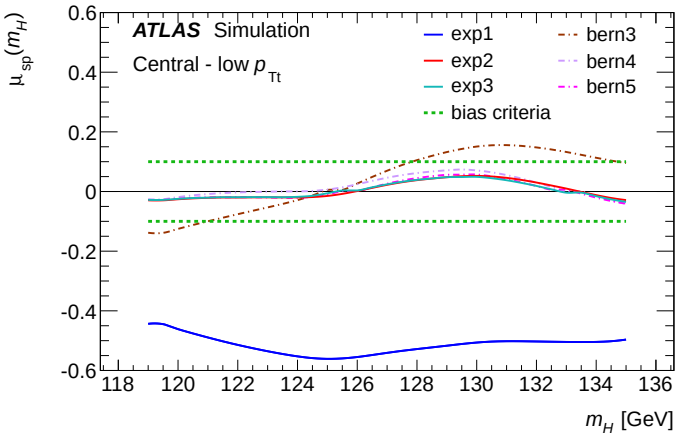

Figure 4.3: Illustration of the choice of functions used to model the background for one of the categories of the final Run 1 analysis described in Section 7. The quantity $\mu_{sp} = S_{spur}/S_{ref}$ is shown for various tested functions, along with the bounds of Eqs. 4.1 and 4.2. The `exp2` function (exponential of a second-order polynomial) is chosen since as the form with the least number of degrees of freedom passing the criteria, following the procedure described in Section 4.2.2. (From Refs [55])

may be obtained in each case. The maximum value of the bias over all possible configurations, the *spurious signal*, is then used as an uncertainty on the background modeling. This value is a conservative estimate of the uncertainty, assuming that the true shape of the data lies somewhere within the range of configurations considered.

However due to the difficulties associated with the generation of high-statistics samples for each possible MC variation, the scan of various simulation configurations was replaced in the $H \to \gamma\gamma$ analyses by a scan over m_H. The spurious signal is then defined as the maximum bias over the range $110 < m_H < 150$ GeV. Due to the somewhat ad-hoc nature of this definition, a strict limit is set on the allowed spurious signal: functions are considered only if the spurious signal S_{spur} value verifies the two conditions

$$S_{spur} < 20\%\, \delta S_{exp} \tag{4.1}$$

$$S_{spur} < 10\%\, S_{exp} \tag{4.2}$$

were S_{exp} and δS_{exp} are respectively the expected signal yield and the expected signal statistical uncertainty. The condition 4.1 ensures that the uncertainty from the background modeling provides a contribution of no more than $\sim$2%, when added in quadrature to the statistical uncertainty. Condition 4.2 ensures that a potential residual bias does not significantly affect the measured signal yield. If several functions are found to satisfy these conditions, the function with the least number of free parameters is selected so as to maximize the sensitivity. The procedure is illustrated in Fig. 4.3.

Some arbitrariness remains in the way conditions 4.1 and 4.2 are defined. In fact the form given above is a compromise between the two competing constraints that on the one hand, the criteria are tight enough to lead to small modeling uncertainties, in order for the analysis not to be strongly dependent on their exact description; and on the other hand, that they are loose enough to allow reasonably simple functions with high statistical power to be used. While the

definitions above were used for all the Run 1 $H \to \gamma\gamma$ analyses from the Higgs boson discovery onward, other choices can be made. In the high-mass search described in Section 8.4, condition 4.1 was loosened from 20% to 30%; and the future high-precision measurements of Higgs couplings described in Section 9.2 will require smaller background modeling uncertainties and thus tighter versions of condition 4.2.

This method of choosing the background description also has the disadvantage of requiring extremely large simulated background samples, to avoid large spurious signal values due to statistical fluctuations. For instance a MC sample with 25 times the data statistics will lead to an uncertainty on the bias equal to 20% of the uncertainty in data: in this case even a function with no true bias would typically not fulfill the spurious signal criteria, due to the contribution from statistical fluctuations. Obtaining a relative statistical uncertainty of 10% on the measured bias, *i.e.* less than 2% of the statistical uncertainty in data, requires a MC sample about 2500 times larger than the data.

For a few fb^{-1} of ATLAS data, this is the same order of magnitude as the $O(10^7)$ events computed in Section 4.2.1 above in the context of a template analysis. The requirements on the precision of the simulated samples are however less stringent in the present case, since the simulation is used only to select the functional form used to describe the background, not to predict its exact shape. The samples are therefore obtained without resorting to full detector simulation; instead, a reweighting procedure is applied to samples generated at truth level only. The reweighting accounts for photon efficiency and energy smearing effects, as well as jet fake rates for the case of reducible background. It is determined in wide bins of E_T and η using smaller samples produced with full detector simulation. It is then applied to a high-statistics sample of about 10^7 $\gamma\gamma$ events produced with the Sherpa generator [63], as well as samples of γjet and jetjet processes produced with Pythia [64, 65], all produced with truth-level information only. Such a procedure, referred to as *smeared MC* had already been implemented for the CSC analysis [15], and subsequently refined and applied to the much larger samples described above.

4.3 Signal Modeling

Precise knowledge of the signal $m_{\gamma\gamma}$ shape is needed to extract the signal yield from data. Due to the small Higgs natural width, this shape is almost entirely driven by detector effects and can be precisely modeled using simulation. Two important systematic uncertainties need to be included in the modeling: the uncertainty on the diphoton mass scale, which induces a global mass shift in the distribution, and the uncertainty on the mass resolution, which modifies the width of the signal peak (see Section 3.3.3). The latter is particularly important for the measurement of the signal yield, since a change in the width of the peak induces a proportional change in the number of fitted signal events. In the final $H \to \gamma\gamma$ analysis of Run-1 data, presented in Chapter 7, an uncertainty of 11% on the mass resolution was found to induce a 7% uncertainty on the signal yield [55], making it the largest single source of experimental uncertainty on the signal yield.

We again chose to instead model the signal shape using an analytical form, this time with fixed parameters, due to practical considerations:

- the signal description is typically simpler, with ∼5 parameters used to describe the full shape;
- the functional form can be easily adjusted: in particular the effect of photon energy scale and resolution variations can be implemented as variations of the peak position and width

parameters, instead of more complex interpolations between the templates obtained in the different cases;

- having both signal and background described by analytical shapes allows the use of *unbinned* shape fits, which do not rely on a particular binning of the data[4].

In practice, functions derived from the Crystal Ball shape [66, 67, 68] are used. The Crystal Ball distribution has a long history of use in flavor physics to describe the diphoton invariant mass distribution of $\pi^0 \to \gamma\gamma$ decays, dating back to a 1979 publication by the Crystal Ball collaboration [69]. Its form consists of a Gaussian core stitched to a power-law distribution on the low-mass side so that both the function and its derivative are continuous at the junction. This form was introduced in the CSC analysis following previous experience on the BaBar experiment, and similar forms were retained for all $H \to \gamma\gamma$ Run 1 analyses.

4.4 Categorization

4.4.1 Sensitivity Improvements Through Categorization

Principle The sensitivity of the $H \to \gamma\gamma$ analysis described above depends almost completely on the amount of background under the signal peak. This in turn depends on two factors: the width of the peak and the S/B at the signal peak. Since the Higgs natural width is about 4 MeV [42], the former is almost completely dominated by the contribution from the mass resolution discussed in Section 3.3.3. The latter can be improved using the photon identification algorithms described in Section 3.3.2, but as noted above the S/B is about 3% even when accounting for the irreducible backgrounds alone.

It is possible to further improve the overall sensitivity of the analysis by making use of regions of phase space with better *local* conditions, either in the form of higher S/B or of lower mass resolution uncertainties. Since these regions typically contain only a small fraction of the total signal yield, it is usually not advantageous to exclude the rest of the dataset. Instead, the "good" regions and the "rest" are treated as separate analyses (called *categories* in the following), from which a single combined result is obtained.

The observed yield $S_{obs,i}$ in each category i can be expressed as $S_{obs,i} = \mu S_{exp,i}$, where $S_{exp,i}$ is the expected yield and μ the signal strength. This provides a combined measurement of μ that is more sensitive than the *inclusive* analysis performed without such separation, with larger gains for larger performance differences between the categories.

Counting Analysis As an illustration, one can consider the case where the shape analysis is reduced to a simple counting analysis in the region of the peak, with a Gaussian-distributed event yield. The signal yields in each category are denoted and S_i; the uncertainties on these yields are $\sigma_i = \sqrt{B_i}$, where B_i is the background yield in the signal region; and the per-category significances are $Z_i = S_i/\sigma_i$. The combined significance for n_{cats} categories can then be written as

$$Z_{comb} = \sum_{i=1}^{n_{cats}} z_i^{comb}, \quad z_i^{comb} = Z_i \frac{Z_{i,exp}}{\sqrt{\sum_{i=1}^{n_{cats}} Z_{i,exp}^2}} \tag{4.3}$$

[4] Although in practice binned fits are often performed in any case for since they are usually faster

where $Z_{i,exp} = S_{i,exp}/\sigma_i$ are the expected significances in each category, under some signal hypothesis.[5] The inclusive significance can be cast in the same form,

$$Z_{incl} = \sum_{i=1}^{n_{cats}} z_i^{incl}, \quad z_i^{incl} = Z_i \frac{\sigma_i}{\sqrt{\sum_{i=1}^{n_{cats}} \sigma_i^2}}. \tag{4.4}$$

In both cases, the significance for the entire dataset is obtained as a linear combination of the per-category significances, with a different set of coefficients for the two cases. One can also note from Eqs. 4.3 and 4.4 that $z_i^{comb}/z_i^{incl} \sim Z_{i,exp}/\sigma_i = S_i/B_i$, modulo a factor that is the same for all categories. The category result is therefore equivalent to applying an S/B-weight to the data.

Performance When considering *expected* significances, then $Z_{comb,exp} \geq Z_{incl,exp}$, since

$$Z_{incl,exp}^2 = \left(\sum_{i=1}^{n_{cats}} f_i^2 Z_{i,exp}^{-2} \right)^{-1} \leq \sum_{i=1}^{n_{cats}} f_i^2 Z_{i,exp}^2 \leq \sum_{i=1}^{n_{cats}} Z_{i,exp}^2 = Z_{comb,exp}^2 \tag{4.5}$$

where $f_i = S_{exp,i}/S_{exp}$ are the per-category signal fractions. The first inequality derives from the well-known inequality between (weighted) arithmetic and harmonic means[6], and the second is due to $f_i \leq 1$. Thus in this case, the categorization always leads to a gain of expected sensitivity, with equality occuring only if all the $Z_{i,exp}$ are equal, so that the categorization is pointless. This of course does not prevent $Z_{comb} < Z_{incl}$ when *observed* significances are considered, for instance if a large negative fluctuation occurs in a category which has a large coefficient for Z_{comb} but a small one for Z_{incl}).

Even in the case of expected significances, finer categorization can in general lead to a small sensitivity penalty due to the fact that more categories usually require more nuisance parameters in realistic cases, unlike the simple example described above. This is the case in the $H \to \gamma\gamma$ search, where extra background normalization and shape parameters are introduced in each category. However it can be shown that this uncertainty should be typically small by considering a simplified version of the $H \to \gamma\gamma$ search: only 3 counting bins are considered, a signal region yield N_{SR} and two sidebands with yields N_1 and N_2, and the background shape is taken to be linear. The uncertainty on the signal yield can be expressed as

$$\sigma_S = \sqrt{N_{SR} + k_1 N_1 + k_2 N_2} \tag{4.6}$$

where the first term accounts for the statistical uncertainty in the signal region, and the other two the uncertainty from the subtraction of the background. Without background NPs, one would have $\sigma_S = \sqrt{N_{SR}}$. Splitting the data into identical categories, one thens obtain a combined expected significance $Z_{comb,exp} = \bigoplus_{i=1}^{n_{cats}} (S/n_{cats})/\sqrt{N_{SR}/n_{cats}} = Z_{incl,exp}$ with neither a gain nor a loss as expected from Eq. 4.5 above. If onw now considers the effect of background NPs,

[5] The formula illustrates the well-known fact that combined *expected* significances can be obtained by adding in quadrature per-category expected significances, but that the same is not true of observed significances.

[6] Defining the generalized mean of data $\{x_i\}$ with order p and weights $\{w_i\}$ as $M_p(\{x_i\};\{w_i\})$, one can show that $M_p(\{x_i\};\{w_i\})$ is a decreasing function of p for fixed $\{x_i\}$ and $\{w_i\}$. In particular one has therefore $M_{-1}(\{x_i\};\{w_i\}) \leq M_1(\{x_i\};\{w_i\})$, which gives the required inequality. Equality occurs if all the $\{x_i\}$ are identical.

one could expect instead $Z_{comb,exp} < Z_{incl,exp}$ due to the extra NPs and the absence of statistical gains when using identical categories. However one can see that again,

$$Z_{comb,exp} = \bigoplus_{i=1}^{n_{cats}} \frac{S/n_{cats}}{\sqrt{N_{SR}/n_{cats} + k_1 N_1/n_{cats} + k_2 N_2/n_{cats}}} = Z_{incl,exp} \tag{4.7}$$

so that no penalty is present. This result is expected to be specific to the case of a linear background shape, rather than hold generally, since in this case the sum of the per-category background shapes is again a linear shape, so that the additional per-category NPs do not bring new freedom to the background description. One could thus still expect a penalty to be present for nonlinear background shapes (e.g. exponentials). However for the case of the $H \to \gamma\gamma$ analysis, the linear shape is at least locally a good approximation to the background shapes actually used (see Section 6.1), and one can thus expect the penalty to remain negligible compared to the gains obtained in reslistic categorizations. This conclusion is confirmed by pseudodata studies in simple $H \to \gamma\gamma$inspired configurations.

Inclusion in the Likelihood Model As detailed in Section 5, the maximum-likelihood (ML) technique provides an appropriate setting to implement categorizations, by expressing the overall likelihood of the dataset as the product of the likelihoods of the individual categories. Since the signal parameterization and the data-driven background parameterization can be obtained in the same way in each category as in the inclusive analysis, the addition of new categories in $H \to \gamma\gamma$ represents a relatively small increase in analysis complexity overall. For the Higgs discovery, 17 categories were used in the $H \to \gamma\gamma$ analysis [12].

The use of categories to increase the sensitivity of the $H \to \gamma\gamma$ analysis is presented in Section 4.4.2 below. The same technique can also be used to provide sensitivity to Higgs couplings properties, by isolating categories enriched in specific production modes, as presented in Section 4.4.3, or to measure differential distributions of event variables as shown in Fig. 4.4.4.

4.4.2 Sensitivity Optimization Through Additional Information from the $\gamma\gamma$ system

The $\gamma\gamma$ mass resolution performance in ATLAS is strongly correlated with the amount of material traversed by the photons upstream of the calorimeter, shown in Fig. 4.4a, as discussed in Section 3.3.3. The resolution therefore varies strongly as a function of photon η, with higher resolution in the central barrel regions and lower resolution particularly in the barrel/endcap transition region. For this reason, the categories shown in Fig. 4.4b in the pseudorapidities η_1 and η_2 of the two photons were introduced as part of the CSC analysis [15].

The central region also collects a larger fraction of the signal than of the background, since the harder p_T spectrum of the former leads to more central events. This effect improves S/B independently of the resolution, and by a similar amount. The total sensitivity gain from these categories measured in the CSC analysis was estimated to be 8% [15].

Separating out converted and unconverted photons also improves the sensitivity due to differences in energy resolution values and in the conversion rates of prompt photons vs. background $\pi^0 \to \gamma\gamma$ processes. The gains were however found to be small, $\sim$2% [15]. The categorization was nevertheless maintained for the Higgs mass measurement [70] in order to provide a finer-grained description of photon energy scale systematics, which are different for the two classes of photons.

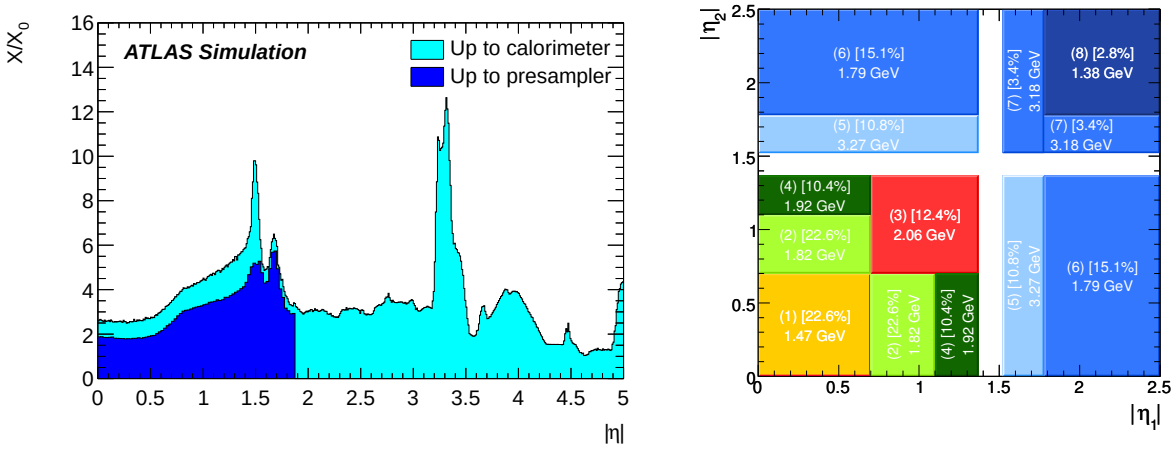

(a) (b)

Figure 4.4: (a) Amount of material upstream of the calorimeter as a function of pseudorapidity; (b) mass resolution for regions of the (η_1, η_2) plane of the pseudorapidities of the leading and subleading photons, for unconverted photons. The percentage values indicate the fraction of signal events in each region. (From Refs. [53] and [15] respectively)

The rest of the kinematic information of the diphoton system can be described in terms of the transverse momentum p_{T} of the $\gamma\gamma$ system and of $\cos\theta^*$, the absolute value of the cosine of the polar angle of the leading photon in the Collins-Soper frame [71], which can be expressed as [72]

$$\cos\theta^* = \frac{|2\sinh\Delta\eta|}{\sqrt{1+(p_T/m_{\gamma\gamma})^2}}\left(\frac{E_{T,1}}{m_{\gamma\gamma}}\right)\left(\frac{E_{T,2}}{m_{\gamma\gamma}}\right). \tag{4.8}$$

The p_{T} information is particularly useful, since higher p_{T} values are associated with processes such as VBF, VH, $t\bar{t}H$ and jet-associated ggF production, which are all associated with lower background levels than the inclusive selection. For low values of p_{T}, better sensitivity can also be achieved by using instead a closely related variable, p_{Tt} [73, 74], defined as the component of the vector $\vec{p}_T$ which is transverse to the thrust axis $\hat{t}$ of the diphoton system:

$$p_{\mathrm{Tt}} = \left\|\vec{p}_T \times \hat{t}\right\|, \qquad \hat{t} = \frac{\vec{p}_{T,1} - \vec{p}_{T,2}}{\|\vec{p}_{T,1} - \vec{p}_{T,2}\|} \tag{4.9}$$

In the configuration where the diphoton p_{T} is small compared to the photon p_{T} values, both p_{Tt} and the longitudinal component p_{Tl} are small. However p_{Tl} is small due to the the cancellation of the two large photon energies, while for p_{Tt} this is due to the small angle between the photon momenta [74]. The p_{Tt} component is therefore less affected by photon energy resolution effects, and benefits from higher resolution in particular at low p_{T}. Since this is the regime most relevant for the separation of signal and background, using p_{Tt} instead of p_{T} yields better sensitivity. In addition, p_{Tt} is less correlated with $m_{\gamma\gamma}$ than p_{T}, so that $m_{\gamma\gamma}$ shapes after p_{Tt} cuts are less distorted and easier to fit. For events with $m_H = 125$ GeV, one has [7] typically $p_{\mathrm{Tt}} \approx 0.65 p_{\mathrm{T}}$.

[7] From Eq. 4.9, one can derive $\left(\frac{p_{\mathrm{T}}}{p_{\mathrm{Tt}}}\right)^2 = 1 + \left(\frac{p_{T,1}^2 - p_{T,2}^2}{2p_{T,1}p_{T,2}\sin\Delta\phi_{\gamma\gamma}}\right)^2$, where $\Delta\phi_{\gamma\gamma}$ is the difference in azimuthal

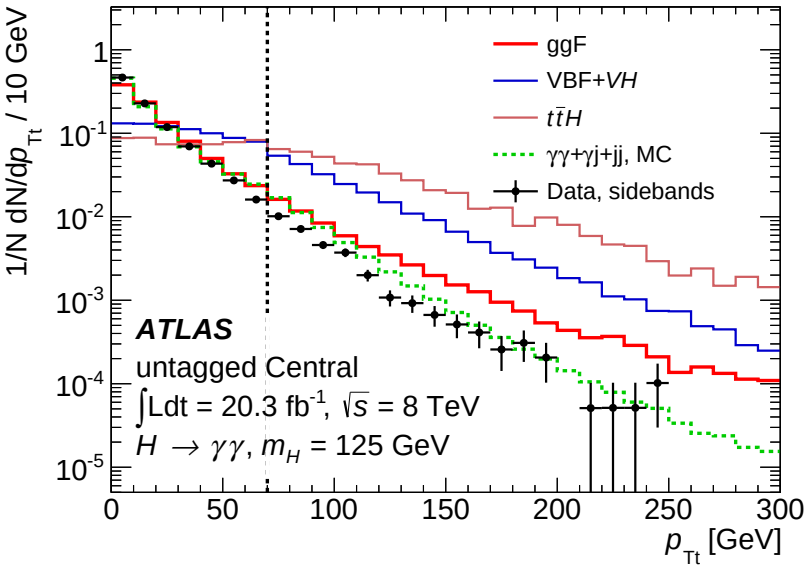

Figure 4.5: Distribution of p_{Tt} for the central η category of the final Run 1 analysis described in Section 7, shown for simulated signal and background samples and for the data. The continuum $\gamma\gamma$ component is modeled at leading order using the Sherpa [63] generator, which does not accurately describe the low end of the p_{T} spectrum [75]. (From Ref. [55])

Figure 4.5 shows the distributions of the p_{Tt} variable for various signal and background samples.

Making full use of this information is however technically difficult. The optimal treatment would make use of multidimensional PDFs in $m_{\gamma\gamma}$, p_{Tt} and $\cos\theta^*$, but this presents several difficulties: for the background, determining an appropriate analytical shape is a complex problem already in one dimension, and more so when considering two or more variables. For the signal, one has the added difficulty of implementing multidimensional deformations of this shape to account for e.g. systematic uncertainties on their theory predictions.

One can simply assume that the multidimensional PDFs factorize into a product of one-dimensional terms. Under this assumption, gains of 8% and 10% were estimated respectively for the inclusion of p_{T} and $\cos\theta^*$ in the CSC analysis [15]. However the assumption was later found to be invalid due to significant correlations between the variables in the background component [76].

A simpler way to make use of the extra kinematic information while avoiding these difficulties is to retain only $m_{\gamma\gamma}$ as a continuous observable, but to introduce categories corresponding to discrete ranges of the other observables. This is equivalent to describing the extra observables by a binned distribution, albeit with a very coarse binning.

This procedure was used for p_{Tt} for the discovery analysis and later iterations (see Chapters 6 and 7). The use of $\cos\theta^*$ was included in the same way for the measurement of the Higgs boson spin using the $H \to \gamma\gamma$ decay [76], but the correlation with $m_{\gamma\gamma}$ in background processes made even this procedure difficult to implement.

angle between the photons, so that $\left(\frac{p_{\mathrm{Tt}}}{p_{\mathrm{T}}}\right)^2 = 1 - \frac{\left(p_{T,1}^2 - p_{T,2}^2\right)^2}{2p_{\mathrm{T}}^2\left(p_{T,1}^2 + p_{T,2}^2\right) - p_{\mathrm{T}}^4}$.

4.4.3 Measurement of Production Modes through Categorization

VBF production represents only $7-8\%$ of total Higgs production at LHC, but presents a distinctive signature: a pair of energetic "tag" jets separated by a wide rapidity gap with little QCD activity (see Section 2.2.1). Due to the lack of an equivalent process for non-resonant diphoton production, background levels in this configuration are much lower than in the inclusive sample and S/B values much higher than the inclusive 3% value can be obtained.

A category tailored to VBF production was therefore designed as part of the CSC analysis, yielding $S/B \sim 0.5$ and the increase in sensitivity from this additional category was $\sim$25%. Based on these results, a category aiming at VBF was included in the Higgs discovery analysis, providing a significant increase in sensitivity as described in Section 6.5.

One can also use the information provided by the VBF category to perform separate measurements of production cross-sections in the VBF and ggF modes. This measurement, illustrated in Fig. 6.3b, was performed as part of the Higgs discovery analysis. In spite of the limited statistics available at the time, it provided important information on the compatibility of the newly-discovered state with the SM Higgs boson. The measurement also provided one of the first windows into Higgs coupling measurements, since the VBF production mainly involves the coupling of the Higgs boson to vector bosons, while the ggF mode mainly depends on its coupling to the top quark.

These measurements were further extended to include categories sensitive to other modes such as WH, ZH and $t\bar{t}H$ production, as described in Section 7, and constituted one of the main avenues of investigation of Higgs coupling properties in Run 1.

4.4.4 Measurement of Differential Cross-sections through Categorization

Finally, the same technique can be applied to the case of of categories corresponding to the bins of a given event variable (e.g. $N_{jets} = 0, 1, 2$ etc.). The event yields in each category then represent a binned differential distribution of the variable for signal events. The use of a combined fit to all categories simultaneously allows the definition of common systematic uncertainties. The technique was pioneered in $H \to \gamma\gamma$, since the signal and background modeling can be performed semi-automatically using the techniques described in Section 4.3 and 4.2 in each of the large number individual categories needed for such measurements [77]. Examples of the distributions obtained using this method are shown in Fig. 4.6.

4.5 Blind Analysis

All the analyses described in this document were performed using the *blind analysis* technique: all the event selections, background modeling and signal extraction techniques were determined based solely on either simulation or data samples that are insensitive to the signal. After the data was *unblinded*, the only allowed changes to the analysis were limited to the determination of subleading systematic uncertainties, minor technical fixes, or changes following a procedure that was precisely determined before unblinding. This method avoids the occurrence of *experimenter's bias* [78] whose effect on the result, though probably rather small, is hard to quantify.

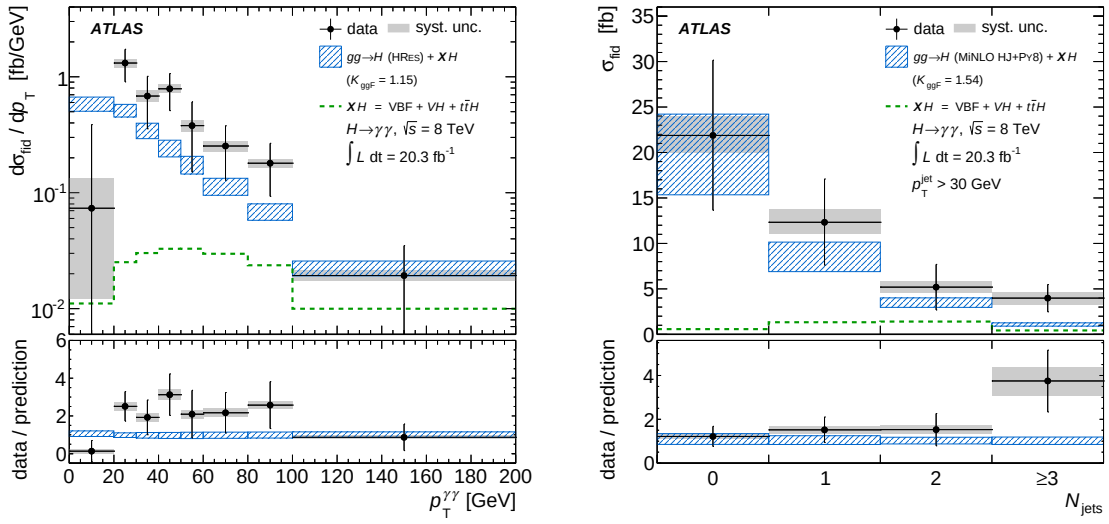

(a) (b)

Figure 4.6: Distribution of (a) Higgs boson p_{T} and (b) number of jets with $p_T > 30$ GeV in $H \to \gamma\gamma$ signal events obtained using the analysis of Ref. [77].

4.6 Personal Contributions

When I joined ATLAS in 2006, CMS had published a study making use of photon shower shape categories to enhance discovery sensitivity [79]. In collaboration with Andreas Höcker and others, we introduced the use of photon η and conversion categories and the p_T and $\cos\theta^*$ variable, as documented in the CSC document [15]. We also introduced the use of unbinned ML fits based on analytical shapes for signal and background to fit the data, an effort which led to the development of the `Hfitter` tool described in Chapter 5. I also implemented an early version of the method described in Section 6.2 to produce large background samples, and used them to select the background parametrizations used in the CSC analysis [15].

Chapter 5

Statistical Framework for $H \to \gamma\gamma$

As described in Section 4, the ATLAS $H \to \gamma\gamma$ analysis relies on two main features: the description of the $m_{\gamma\gamma}$ shape of both the signal and background components using analytical functions, and the splitting of the dataset into *categories*, *i.e.* subsets which are described separately but from which combined results are obtained. This description of the data can be naturally implemented within the framework of unbinned maximum-likelihood (ML) estimation, presented in Section 5.1. The usual classes of physics results – discovery p-values and significances, upper limits and two-sided confidence intervals on model parameters – can then be defined within this setting as frequentist hypothesis tests, as briefly explained in Section 5.2.

When the $H \to \gamma\gamma$ analysis was initiated, tools implementing this description within the `ROOT` framework were already available as part of the `roofit` package. These tools were however designed as a very general implementation of ML fitting, and their use for the particular class of models relevant for $H \to \gamma\gamma$ was rather cumbersome. The `Hfitter` package was therefore introduced as an additional software layer to simplify both the definition of the statistical models used in the $H \to \gamma\gamma$ analysis, and their use in the computation of analysis results. A brief description of its features is provided in Section 5.3. A more complete overview is provided in Ref [80].

5.1 Likelihood Modeling

The $H \to \gamma\gamma$ analysis relies on a description of the data based on the probability $P(\text{data}; x)$ to obtain a given observed dataset in terms of some model parameters x. These parameters include the *parameters of interest*, the quantities whose measurement is the goal of the analysis; and *nuisance parameters* which are necessary to define the model but are not themselves of immediate interest (e.g. the parameters describing the shape of the background to $H \to \gamma\gamma$).

Since the goal is to estimate the parameters of interest, the model is given in terms of the likelihood function $\mathcal{L}(x; \text{data})$, which is identical to the probability $P(\text{data}; x)$, but considered as a function of the parameters x. It encapsulates all the information contained in the data, as described by the model. Standard statistical techniques can be applied to it to extract the usual physics results as described in Section 5.2.

5.1.1 Unbinned Likelihood Modeling

The $H \to \gamma\gamma$ analysis uses a single continuous observable, the diphoton invariant mass $m_{\gamma\gamma}$. The data is described in terms of an extended unbinned likelihood model, in which the shape of the per-event $m_{\gamma\gamma}$ distribution is described using an analytical function. The likelihood of the full dataset can then be expressed as

$$\mathcal{L}(n; \{m_{\gamma\gamma,i}\}) = e^{-N} \frac{N^n}{n!} \prod_{i=1}^{n} P(m_{\gamma\gamma,i}). \tag{5.1}$$

The term in front of the product is a Poisson probability distribution, describing the fluctuations in the number of observed events n in terms of its true value N. The $m_{\gamma\gamma,i}$ are the observed values of $m_{\gamma\gamma}$ for each event, and $P(m_{\gamma\gamma})$ is the per-event probability distribution (PDF) for $m_{\gamma\gamma}$. The product represents the total probability to obtain the n values $m_{\gamma\gamma,i}$ in a random process described by the probability law $P(m_{\gamma\gamma})$.

The term $P(m_{\gamma\gamma})$ can be separated into distinct contributions from signal and background processes,

$$P(m_{\gamma\gamma}) = f_S P_S(m_{\gamma\gamma}) + f_B P_B(m_{\gamma\gamma}) \tag{5.2}$$

where f_S and $f_B - 1 - f_S$ are the relative fractions of the signal and background contributions, respectively, and $P_S(m_{\gamma\gamma})$ and $P_B(m_{\gamma\gamma})$ are the respective PDFs of the signal and background components. The full likelihood can therefore be expressed in the form

$$\mathcal{L}(N_S, N_B, \theta; n, \{m_{\gamma\gamma,i}\}) = \frac{e^{-(N_S+N_B)}}{n!} \prod_{i=1}^{n} [N_S P_S(m_{\gamma\gamma,i}; \theta) + N_B P_B(m_{\gamma\gamma,i}, \theta)] \tag{5.3}$$

where $N_S = N f_S$ and $N_B = N f_B$ are respectively the expected numbers of signal and background events and θ represents the nuisance parameters of the model.

An alternative description of the data would be a binned likelihood, in which the $m_{\gamma\gamma}$ spectrum is split into discrete bins of an appropriate size. The likelihood can then be expressed as the product of Poisson distributions for the numbers of events in each bin. This binned formulation tends towards the unbinned one as the size of the bins becomes small with respect to the experimental resolution in $m_{\gamma\gamma}$.

The binned method has the disadvantage of being dependent on the arbitrary choice of the binning used (smaller bins lead to reduced biases but larger statistical uncertainties on the reference shapes). It has however the advantage of relying only on the assumption of Poisson distributions for the event counts in each bin, with Poisson parameters obtained from simulation. This is generally better-motivated than the smooth parameterizations of the signal and background shapes that have to be assumed for the unbinned method.

There are however strong practical arguments for favoring the unbinned method over the binned one in the case of $H \to \gamma\gamma$, as discussed in Section 4, and the binned technique will therefore not be discussed further.

5.1.2 Categories

As already presented in Section 4.4, additional sensitivity can be gained by splitting the full datasets into categories. These are assumed to be non-overlapping, so that each event in the dataset belongs to exactly one category. The categories are therefore statistically independent

and the total likelihood can simply be written as the product of the likelihoods in each category,

$$\mathcal{L}(\{N_{S,c}\}_c, \{N_{B,c}\}_c, \theta; \{n_c\}_c, \{m_{\gamma\gamma,i,c}\}_{i,c}) = \prod_{c=1}^{n_{cats}} \mathcal{L}_i(N_{S,c}, N_{B,c}, \theta; \{m_{\gamma\gamma,i,c}\}_i) \tag{5.4}$$

where n_{cats} is the number of categories, and the quantities $N_{S,c}$, $N_{B,c}$ and n_c now refer respectively to the number of expected signal and background events and the number of observed data events in the category with index c. The notation $\{X_c\}_c$ denotes the set of all the quantities X_c, running over all values of the index c.

While this expression is similar to that of a set of n_{cats} independent measurements, the per-category likelihoods may be correlated through the use of common parameters. In particular a single parameter of interest can be extracted from all the categories simultaneously. The canonical example is the case of a global factor μ scaling all of the $N_{S,c}$, describing the strength of a Higgs signal that contributes known relative amounts to each category (see Section 4.4.2). This is similar to an *a posteriori* combination of the measurements performed in each individual category, but correctly accounts for inter-category correlations.

5.1.3 Systematic Uncertainties

The description presented so far includes only statistical uncertainties,*i.e.* uncertainties related to the random fluctuations of the event counts and their observed $m_{\gamma\gamma}$ values. Other uncertainties also arise from the the underlying assumptions used to build the model: for instance on the detector response, theory expectations, etc.

The strategy adopted for the $H \to \gamma\gamma$ analysis is to introduce new degrees of freedom providing additional flexibility to the model to account for these uncertainties. An example is the width of the peak used to describe the signal component: its value is not precisely known due to the uncertainty on diphoton mass resolution (see Section 4.3) and a nuisance parameter is therefore introduced to adjust its value.

These parameters cannot be left free lest this spoil the measurement (for instance by allowing a mass peak with arbitrary width). In some case such as the mass resolution uncertainty mentioned above, the parameter can be obtained from a separate measurement. One can then include the likelihood of this *auxiliary measurement* into the model to act as a constraint on the nuisance parameter. For simplicity, this term is usually parameterized as a Gaussian distribution or similar, with a width corresponding to the uncertainty on the parameter.

Some uncertainties may arise in contexts that cannot be related to a realistic auxiliary measurement. A typical case is that of theory uncertainties obtained by ad-hoc techniques such as scale variations. In this case, one can still introduce a constraint term by analogy with the previous case, using the variations on the parameter to define the width of the constraint term.

The full likelihood is thus finally given in the form

$$\begin{aligned}\mathcal{L}(\{N_{S,c}\}_c, \{N_{B,c}\}_c, \theta, \{\delta_s\}_s; \{n_c\}_c, \{m_{\gamma\gamma,i,c}\}_{i,c}, \{\alpha_s\}_s) = \\ \prod_{c=1}^{n_{cats}} \mathcal{L}_i(N_{S,c}, N_{B,c}, \theta, \delta_s; \{m_{\gamma\gamma,i,c}\}_i) \prod_{s=1}^{n_{\text{syst}}} C_s(\delta_s; \alpha_s)\end{aligned} \tag{5.5}$$

which is similar to that of Eq. 5.4 but includes additional parameters δ_s implementing systematic uncertainties, as well as the auxiliary measurements α_s used to constrain them using the form C_s.

Concerning the expressions of C_s, the following rules will be observed, based more on technical convenience than principle:

- For parameters which can take positive or negative values, a Gaussian constraint is used. This is achieved by expressing the model parameter as $Q = Q_0(1 + \sigma_Q \delta)$, where Q_0 and σ_Q are respectively the central value and relative uncertainty on the parameter, and δ is a normalized NP constrained by the normal form $C_s(\delta_s; \alpha_s) = \exp\left[-(\delta_s - \alpha_s)^2/2\right]$.

- For parameters which must take positive values only (e.g. PDF normalization parameters), the constraint is taken to be a Log-normal distribution, for which the parameter can be taken to be always positive. This is implemented by expressing the parameter as $Q = Q_0 \exp\left[\log(Q^{\pm}/Q_0)\delta\right]$, where $Q^{\pm}$ are the $\pm 1\sigma$ variations of Q, and again constraining δ using a normal distribution. The expression ensures that the values $Q^{\pm}$ are recovered for $\delta = \pm 1$.

The values of the α_s are set to 0 when fitting data, since the Q_0 are already by definition the nominal values. They are however set to non-zero values randomly generated from the expressions of C_s when generating pseudo-datasets in the unconditional ensemble, as described in more detail in Ref. [81].

5.2 Discovery, Limit-setting, and Confidence Intervals

5.2.1 Frequentist Setting

Statistical techniques based on frequentist methods [82] were used to produce the results of all ATLAS Higgs searches. These results fall into two main categories:

- Discovery: the computation of the probability to obtain a signal at least as large as the observed one, under the assumption that no signal is present. This probability will be referred to as the discovery p-value in the following.

- Parameter estimation: the derivation of a confidence interval of the form $[\hat{\theta} - \delta\theta_-, \hat{\theta} + \delta\theta_+]$ such that the true value of θ is contained within the interval at a given confidence level (usually 68%).

A possible alternative to this framework is the use of Bayesian techniques. These offer several advantages, in particular the benefit of offering more direct interpretations of the data. For instance, in the case of an observed excess of events, Bayesian methods allow to compute probabilities such as p(Higgs|data) for the presence of a Higgs boson in the data.

By contrast, frequentist techniques only provide a p-value, i.e. the probability p(data|bkg) for the occurrence of such an excess under the hypothesis that only background is present. The latter statement is clearly relevant to the question of the existence of the Higgs boson, since a disagreement with the background-only hypothesis is a necessary condition for discovery. It does not however directly answer the question of whether a Higgs boson is indeed present [1].

[1] an example of the statement that "Bayesians address the question everyone is interested in by using assumptions no-one believes, while frequentists use impeccable logic to deal with an issue of no interest to anyone." [83]

Small p-values can also be misleading, in particular if the alternatives to the background-only hypothesis are also very unlikely.[2]

However, this benefit of Bayesian techniques is critically dependent on the input of a prior probability for the hypothesis under test: for instance the probability distribution function for m_H. This treats the value of physical parameters such as m_H as random variables, whose value results from a random process occurring each time an experiment is performed. By contrast, in the frequentist scheme such parameters are considered to have a well-defined, if unknown, value, an ansatz more in line with the usual underpinnings of science [84]. In more practical terms, there is no fully objective way to provide prior probabilities [85], so that Bayesian results are intrinsically dependent on the experimenter's prior assumptions. In practice this is not problematic as long as the priors are specified; the dependence on a particular choice of prior is also typically weak in usual cases. For these reasons, and the fact that some Bayesian methods are less computationally intensive than equivalent frequentist ones, some ATLAS results have made use of Bayesian techniques. Higgs measurements were however performed exclusively in a frequentist context.

5.2.2 Likelihood Ratio Tests

The results listed in the previous section are obtained by testing particular hypotheses, usually based on a signal strength value $\mu = \mu_0$ and denoted as H_{μ_0}. The test is performed by comparing the result of a fit to the data assuming this hypothesis to that of a fit under an alternate hypothesis $H_{\hat{\mu}}$, corresponding to the best-fit signal-strength $\hat{\mu}$, using the *profile likelihood ratio* (PLR) test statistic

$$\lambda(\mu_0) = -2\log\frac{\mathcal{L}(\mu_0, \hat{\theta}_{\mu_0})}{\mathcal{L}(\hat{\mu}, \hat{\theta})}. \tag{5.6}$$

The values $\hat{\theta}$ and $\hat{\theta}_{\mu_0}$ denote respectively the unconditional best-fit values of the nuisance parameters θ, and their best-fit values under the hypothesis $\mu = \mu_0$. In the absence of nuisance parameters, the Neyman-Pearson lemma [86] would ensure that the likelihood ratio provides the optimal test. The choice of nuisance parameter values used to evaluate the likelihoods in Eq. 5.6 above, denoted as *profiling* however ensures near-optimal behavior even in their presence [87].

The p-value of the test is computed from the distribution $f(\lambda(\mu_0); \mu = \mu_0)$ of the PLR under the tested hypothesis, as the integral of f over a range going from the observed value of $\lambda(\mu_0)$ to infinity (see Fig. 5.1). Under rather general assumptions, $f(\lambda(\mu_0); \mu = \mu_0)$ follows a χ^2 distribution [88, 89]. This will be denoted as the *asymptotic approximation* in the following. Due to their rather general applicability, asymptotic distributions are used to derive most of the results presented in this document.

[2] We can take as an example a multiverse-type setting where Higgs boson masses in each universe are drawn at random from a flat distribution in the range $0 < m_H < M_{pl} \approx 10^{19}$ GeV, and that Higgs boson searches are only sensitive in the region $m_H < 1$ TeV. The probability that the Higgs boson in our particular universe is accessible to these searches is therefore $\approx 10^{-16}$. Even in the case of a 5σ "discovery", it would thus be far more likely that the Higgs boson is inaccessible and the discovery is in fact spurious ($p \approx 10^{-7}$), rather than the case of the true discovery of a Higgs boson that fortuitously happens to be accessible ($p \approx 10^{-16}$). This conclusion would be however reversed for the $> 9\sigma$ significance achieved by ATLAS with the full Run 1 dataset [14]

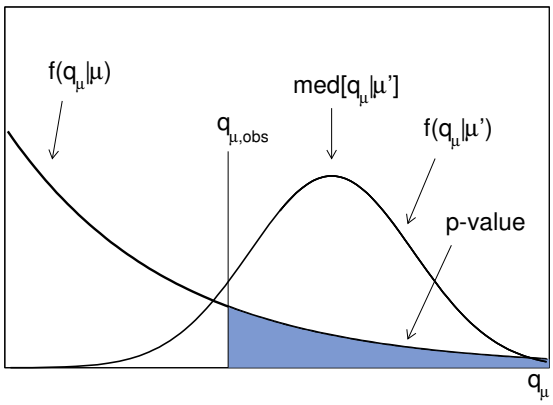

Figure 5.1: Illustration of the computation of a p-value using a test statistic q_μ. $f(q_\mu;\mu')$ denotes the distribution of q_μ under the μ' hypothesis, and $q_{\mu,obs}$ the value of q_μ observed in the data

5.2.3 Discovery P-value Computations

To test for discovery, one attempts to exclude the background-only hypothesis corresponding to $\mu = 0$. Since furthermore only $\mu > 0$ is usually considered as a valid signature for signal, one uses the one-sided test statistic

$$t_0^{\text{uncap}} = \begin{cases} +\lambda(0) & \hat{\mu} \geq 0 \\ -\lambda(0) & \hat{\mu} < 0. \end{cases} \tag{5.7}$$

where the $\mu > 0$ and $\mu < 0$ cases are separated. The discovery p-value is usually expressed as a *significance*, corresponding to the value of the parameter of a normal distribution for which the tail integral is equal to the p-value. In the asymptotic approximation, this is given as

$$Z = \Phi^{-1}\left(1 - p_{t_0^{\text{uncap}}}(t_0^{\text{uncap}})\right) = \begin{cases} +\sqrt{t_0^{\text{uncap}}} & \hat{\mu} \geq 0 \\ -\sqrt{-t_0^{\text{uncap}}} & \hat{\mu} < 0. \end{cases} \tag{5.8}$$

with $\mu < 0$ corresponding to negative significances.

In searches, p-values are often computed at several values of a parameter, and the minimum value is reported. This was the case in particular for the Higgs search: since m_H was unknown, the search was performed over the range $110 < m_H < 150$ GeV, and an excess found at $m_H = 126.5$ GeV. In this setting, the p-value as computed above only accounts for the probability for a background fluctuation to create an excess *at the m_H value where such an excess was seen in the data*. This is denoted as a *local* p-value. It does not account for the *look-elsewhere effect* (LEE), the possibility that an excess could also occur at a different m_H position. Since such an excess would also have been interpreted as a signal, given that m_H was unknown, this must be accounted for when computing the p-value.

This *global* p-value can be naively obtained by multiplying the local p-value by a trials factor corresponding to the number of independent experiments in the mass range above. Since the FWHM of the peak is about 4 GeV [12] and the range spans 40 GeV, this factor can be estimated to be about 10 for the Higgs search.

The more rigorous method to compute global p-values was employed for both the Higgs search described in Section 6 and the search for new scalar resonances in Section 8. In this method,

pseudo-experiments are generated and the number of excesses with a significance exceeding a predefined level is counted in each case, which provides a measure of the global significance. The key point is that this level need not be the value of the observed significance, but can be set to a rather low value (typically around 1σ). An analytical formula is then used to extrapolate the result to the higher observed significance. This allows the use of only a relatively small number of pseudo-experiments, even for testing large observed significances. The method can be applied in one [90] or multiple [91] dimensions.

Alternatively, a brute-force approach can be used, where the global significance is obtained from pseudo-experiments by directly counting the number of pseudo-experiments that reach or exceed the observed significance level. This approach requires the generation of large numbers of pseudo-experiments, but allows to forgo the use of asymptotic formulas.

5.2.4 Confidence Intervals and Upper Limits

Confidence intervals on a model parameter are computed using the PLR of Eq. 5.6 using the *likelihood interval* prescription:

- the central value of the interval is defined as $\mu = \hat{\mu}$, for which the minimum value $\lambda(\hat{\mu}) = 0$ is reached
- the endpoints of a 68% CL interval are defined as the values $\mu^{\pm}$ such that $\lambda(\mu^{\pm}) = 1$

The method is exact in the asymptotic approximation, and remains approximately correct when the approximation is mildly broken [92].

Upper-limits on μ are computed using the one-sided test statistic

$$\tilde{q}_{\mu_0} = \begin{cases} \lambda(\mu_0) & 0 \leq \hat{\mu} \leq \mu_0 \\ -2\log\frac{L(\mu=\mu_0,\hat{\theta}_{\mu=\mu_0})}{L(\mu=0,\hat{\theta}_{\mu=0})} & \hat{\mu} < 0 \\ 0 & \hat{\mu} > \mu_0 \end{cases} \tag{5.9}$$

defined in Ref. [81]. The one-sided prescription removes the region $\mu_0 < \hat{\mu}$, since the point of an upper limit is to determine which hypotheses *above* $\hat{\mu}$ can safely be excluded (excluding small hypothesis values below $\hat{\mu}$ would be relevant for *lower* limits). The region $\hat{\mu} < 0$ is also treated in a special way: the likelihood value at $\hat{\mu} < 0$ is replaced by the value at $\mu = 0$. This avoids potential problems with $\hat{\mu} < 0$ leading to negative PDF normalization.

The limit is to be reported as the hypothesis μ_{up} for which the p-value $p_{\mu_{up}}$ reaches a predefined level (usually 5% for a 95% CL exclusion). This requires to solve the equation $p_{\mu_{95}} = 5\%$ for μ_{95}; the practical implementation is presented in Section 5.3.2.

Finally, the CL_s method [93] is usually used to avoid unphysically small limits. The issue can be understood by noting that by definition, a 95% CL upper limit accidentally excludes the true parameter value 5% of the time. This means that in experiments with zero true signal, the upper limit is negative 5% of the time, by construction. While this is simply a manifestation of the natural randomness of an observed limit, it is sometimes perceived as disturbing. To avoid this, the p-value calculation can be modified to use

$$p_{\mu_0}^{CL_s} = \frac{p_{\mu_0}}{p_0} \tag{5.10}$$

where p_0 is the p-value for the $\mu = 0$ hypothesis. The value of p_0 is usually quite large, since $\mu = 0$ is not typically excluded, in which case the modified p-value is close to the original. However p_0 is small in the case where the limit is negative in the standard calculation, and the $1/p_0$ factor leads to a higher p-value that avoids negative limits in the modified calculation. This comes however at the expense of coverage properties: due to the modification, CL_s upper limits are weaker than purely frequentist limits based on p_{μ_0} and therefore overcover. In particular, coverage approaches 100% at small values of μ.

Asymptotic formulas are available for this procedure in the Gaussian limit [81], and are used for most $H \to \gamma\gamma$ results.

5.2.5 Pseudo-datasets and Asimov Datasets

Analysis results usually include not only the observed result in data, but also *expected* results, which correspond to the typical outcome in a predefined scenario. These results may be used to gauge the sensitivity of a measurement, independently of possible statistical fluctuations which may affect the observed result in a positive or negative way. They can also be used to check the consistency of the observed result with a particular scenario. For the latter case, one requires not only the expected central value of the result, but also the expected range of its variations, to which the observed value can be compared.

The baseline method to produce expected results is the generation of *pseudo-experiments*, artificial datasets which are randomly drawn from the PDF of the model for some value of the parameters (typically the values obtained either from simulation or from a fit to data). By definition these pseudo-datasets are distributed according to the model PDF, and correspond to the outcome that would be obtained by performing multiple repetitions of the measurement, under the assumption that the model exactly describes the measurement process. By repeating the computation of a statistical computation on many pseudo-datasets, a distribution of results is obtained. The median expected result and its variations can be obtained from the median and width of this distribution.

Since the pseudo-experiment method is typically computer-intensive, ATLAS results usually utilize the *Asimov dataset* method [81] instead. This involves the generation of a single carefully-chosen dataset, defined to be such that fitting the model to it yields exactly the parameter values used for its generation. In practice, this corresponds to a dataset where the distribution of events reproduces exactly the PDF of the $m_{\gamma\gamma}$ observable for a given set of parameter values, without statistical fluctuations. It can be shown [81] that in the asymptotic regime, the result obtained from the Asimov dataset exactly matches the median of the pseudo-experiment results described above. The expected variations of the result can also be obtained using asymptotic formulas. In the asymptotic regime, this method therefore provides a lighter alternative to the pseudo-experiment method, and is used for the results presented in this document unless otherwise specified.

Pseudo-datasets can also be obtained to generate the distributions of the test statistics described in Section 5.2. These distributions can then be used to compute p-values without relying on the asymptotic approximation.

5.3 The Hfitter Program

The techniques described in the previous program are mathematically straightforward but technically challenging to implement. A particular issue is the complexity of the models used to describe the data with the required degree of precision: as will be shown in Chapter 6, the models used for $H \to \gamma\gamma$ analyses employ ∼1000 real parameters and ∼500 functions. The reliable implementation of such complex descriptions and their use for the computation of statistical results represent a significant challenge.

A crucial ingredient for this effort is the `roofit` toolkit distributed as part of the ROOT [94] framework. It was developed to perform unbinned maximum likelihood fits, initially for the BaBar experiment [95]. It provides a powerful and computationally efficient framework to define PDFs and perform binned and unbinned fits to the data.

However, when the $H \to \gamma\gamma$ effort was started in ATLAS in 2006, the usage of `roofit` for the $H \to \gamma\gamma$ analysis was technically non-trivial since defining large models using basic roofit syntax was time-consuming and error-prone. No standard tools were available to compute the statistical results described in the previous section from the mode.

The `Hfitter` program was initially developed to address these issues. Development consequently followed two main directions:

- the development of model-building tools, producing `roofit` PDFs specified using a simple modeling language;
- the development of statistical tools implementing the algorithms described in the previous section.

These two aspects are described in Sections 5.3.1 and 5.3.2 below.

5.3.1 Model Building

The `roofit` toolkit provides a very elegant and general description of PDFs and their building blocks, implemented as C++ classes. The main ingredients are

- `RooRealVar`: a class describing a simple parameter, holding a real value and associated uncertainties
- `RooFormulaVar`: an implementation of a real function, built from a formula and objects describing its parameters (usually `RooRealVar`s or other `RooFormulaVar`s)
- `RooAbsPdf`: the PDF base class, supporting fit operations, integration and normalization. The `roofit` toolkit provides implementations for most of the standard PDF forms as classes derived from this base. Both the PDF observables and parameters are provided in the form of either`RooRealVar`s, `RooFormulaVar`s or other real values.
- `RooCategory`: a class describing a variable with discrete values, used to implement the categories of Section 5.1.2.

This framework is extremely flexible and well-designed, but building complex models from these building blocks circa 2006 required significant effort. The typical strategy was a pyramidal scheme, defining first the basic real parameters, then building up formulas, then the PDFs and

finally the full model, with each item requiring the instantiation of new objects. The possibilities offered by `roofit` are also wider than what is required for the class of models used in the $H \to \gamma\gamma$ analysis, described in Section 5.1 above, and the definition of such models could be done in a simpler setting.

The description of the model in `Hfitter` is provided in a *datacard*, a text file that is processed by a parser. The information is then used to generate a C++ object containing the model.

The form of the model is restricted to that of Eq. 5.5, and is defined using the following declarations:

- Observables: the observable variables used in the PDFs, instantiated by `Hfitter` as objects of type `RooRealVar`
- Categories: the categories into which to split the data and its model description, instantiated by `Hfitter` as objects of type `RooCategory` or similar.
- Components: this defines each signal or background component, specifying the PDF to be used for each (if necessary with different choices for each category). For each component, `Hfitter` instantiates the corresponding PDF object and the real parameter holding the number of events.
- Parameters: defines the initial values of real variables, and the formulas of more complex expressions. Formulas are used in the definition of the PDFs above, while initial values are assigned to the corresponding parameters.
- Constraints: defines the form of the constraints applied on model parameters. These are instantiated by `Hfitter` and included in the likelihood.

An example datacard for a simplified form of the $H \to \gamma\gamma$ measurements is shown below:

```
observable mgg = 125 min=100 max=160 bins=120 unit=GeV
category cat = (cat1, cat2, catX)

component Signal = RooGaussian ("mgg", "mHiggs", "sigmaG")     for cat = ( cat1, cat2 ),
                 RooBifurGauss("mgg", "mHiggs", "sigmaL", "sigmaR") for cat = ( catX )
component Background = PDF("mgg", "exp(xi*mgg)", "xi") for cat = ( cat1, cat2, catX )

split nSignal, nBackground along cat
formula nSignal_i (i in cat) = (mu * nSM_i)
nSM_cat1 = 150
nSM_cat2 = 50
nSM_catX = 200
mu = 1 L(-1 - 100)

nBackground_cat1 = 20000 L(0 - 1000000)
nBackground_cat2 = 10000 L(0 - 1000000)
nBackground_catX = 70000 L(0 - 1000000)

mHiggs = 125 C L(110 - 140) // unit=GeV
sigmaG = 1.5 // unit=GeV
sigmaL = 2   // unit=GeV
sigmaR = 1.5 // unit=GeV

split xi along cat
```

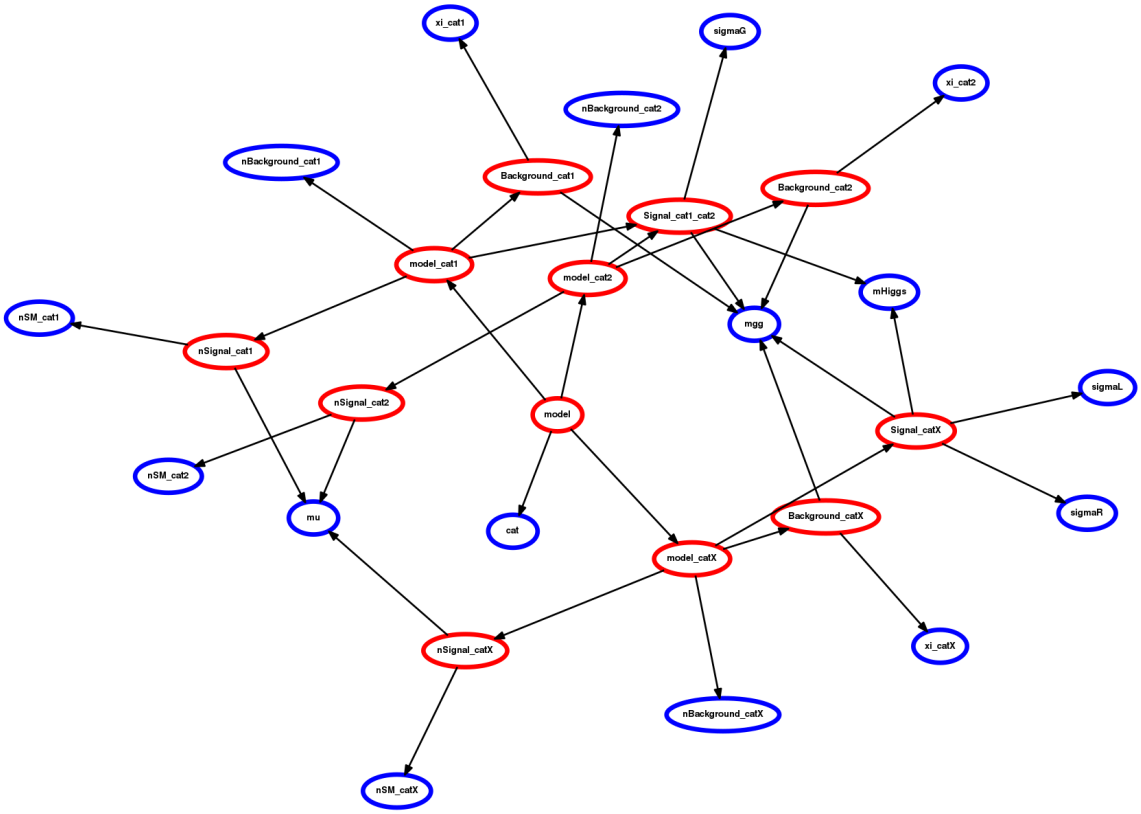

Figure 5.2: Graphical view of the simple model given in the text. The blue boxes represent real numbers, while red boxes are expressions - formulas or PDFs

.

```
xi_cat1 = -0.02 L(-0.1 - 0) // unit=GeV^{-1}
xi_cat2 = -0.02 L(-0.1 - 0) // unit=GeV^{-1}
xi_catX = -0.01 L(-0.1 - 0) // unit=GeV^{-1}
```

This defines a combined μ measurement in 3 categories. The signal shape the same Gaussian form in categories 1 and 2, while category 3 is described by a bifurcated Gaussian. The background is exponential in all 3 categories. A graphical view of the resulting model is shown in Fig. 5.2. The structure is already quite complex: the PDFs follow a tree structure (full model $\rightarrow$ categories $\rightarrow$ signal and background) but the leaves are cross-linked by variables such as $m_{\gamma\gamma}$, μ and m_H which enter at multiple points.

A more complete description of the datacard syntax is given in Ref. [80].

5.3.2 Statistical Calculators

The use of models to produce statistical results is implemented in `Hfitter` using specialized classes called calculators. They follow a modular approach, allowing the result on one computation to be used in another. The following basic functionality is provided:

- `HftMLCalculator`: perform the minimization of $-2\log\mathcal{L}$ for the model over a specified dataset
- `HftPLRCalculator`: compute the PLR of a model on a provided dataset, using two instances

of `HftMLCalculator` to compute the two terms of the difference in negative log-likelihood values.

- `HftUncappedPValueCalculator`: compute p-values based on the t_0^{uncap} test statistic described in Section 5.2.3. The calculator implements the computation of the test statistic, based on the PLR computed using a `HftPLRCalculator`. The computation of the p-values from the test statistic is also implemented, using either the asymptotic approximation or a provided sampling distribution. Similar classes are also provided for other discovery test statistics, such as the capped one-sided case and two-sided definitions presented in Ref. [80].

- `HftQTildaLimitCalculator`: performs the computation of the $\tilde{q}_\mu$ test statistic described in Section 5.2.4, as well as the corresponding exclusion p-values. As for discovery, the computation can be done using either asymptotic formulas or a provided sampling distribution. Classes for other test statistic definitions listed in Refs. [80, 81] are also provided.

- `HftCLsCalculator`: Computes p-values modified using the CL_s technique, taking as input a calculator computing frequentist exclusion p-values, either of the `HftQTildaLimitCalculator` type or another class implementing a similar test statistic.

- `HftIterLimitCalculator`: computes upper limits for a given exclusion CL (by default 95%), using an iterative approach. It takes as input a calculator for exclusion p-values (of type `HftCLsCalculator`, `HftQTildaLimitCalculator`, etc.) and an initial hypothesis value, and solves for the hypothesis corresponding to the requested exclusion CL.

- `HftScanLimitCalculator`: computes upper limits for a given exclusion CL (by default 95%). It takes as input a set of exclusion p-value calculators (of type `HftCLsCalculator`, `HftQTildaLimitCalculator`, etc.) to compute the exclusion CL at various predefined hypothesis values. The exclusion p-values are then interpolated to find the hypothesis corresponding to the requested exclusion CL. The computation is more robust that the one of `HftIterLimitCalculator` above, but generally slower and requires to specify the tested hypothesis values by hand.

- `HftToysCalculator`: generates pseudo-datasets, which are then used to compute expected results for any of the algorithms listed above, or generate sampling distributions for the corresponding test statistics as described in Section 5.2.5.

- `HftAsimovCalculator`: generates Asimov datasets and performs any of the computations above to obtain expected results as described in Section 5.2.5.

- `HftScanningCalculator`: performs the computation defined by another calculator at various values of a scanning parameter.

The calculators described above can be combined as building blocks to produce complex results such as the expected limit shown in Fig. 5.3, which combines the following steps: computation of a frequentist exclusion p-value on μ (using `HftQTildaLimitCalculator`); modification of the result to use CL_s (using `HftCLsCalculator`); computation of the 95% upper limit on μ (using the scanning approach of `HftScanLimitCalculator`); computation of the expected result of this result in the $\mu = 0$ hypothesis (using `HftAsimovCalculator`); and finally scan over m_H (using `HftScanLimitCalculator`) to obtain results for a range of mass points. The observed limit is computed in the same way, but without the `HftAsimovCalculator` step.

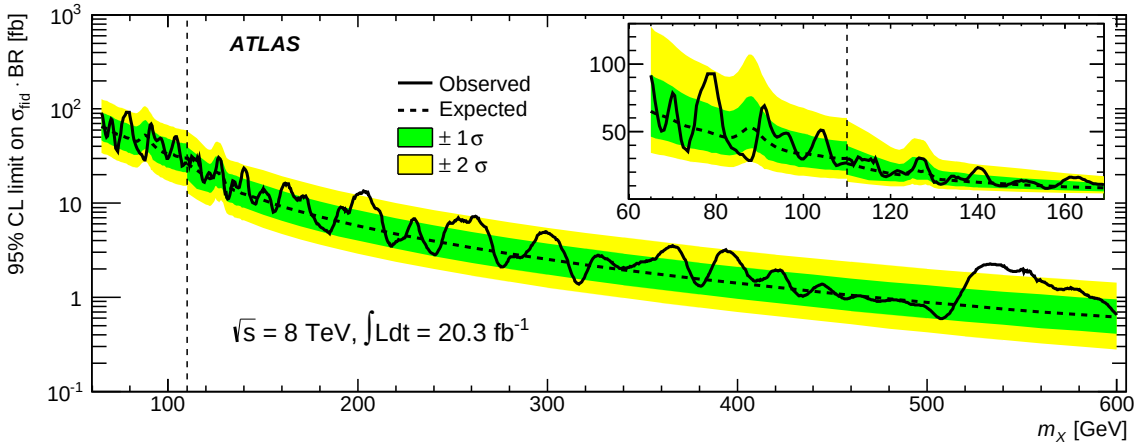

Figure 5.3: Observed and expected 95% CL CL_s limits for the Run 1 $\gamma\gamma$ resonance search, provided as an example of the statistical computation functionality described in the text. ((From Ref. [96]))

A more complete documentation of the statistical computations currently implemented is provided in Ref. [80].

5.3.3 Usage

`Hfitter` is distributed as a `ROOT` package. Most simple computations can be performed on the command line using shell scripts. More complex operations can be implemented in compiled C++ code using the classes described above, or on the `ROOT` command line. A full documentation of these options is provided in Ref. [80].

5.3.4 Current Status

The Hfitter program was developed starting in 2006, and was used to produce results for the CSC publication [15], where the usage of categorized unbinned ML fits for $H \to \gamma\gamma$ in ATLAS was first introduced. It was subsequently used for $H \to \gamma\gamma$ studies. The model used for the $H \to \gamma\gamma$ part of the ATLAS Higgs discovery analysis was implemented using `Hfitter`, alongside other implementations. It was used to produce several of the results of the Higgs discovery paper [3] [12], in particular the first Higgs couplings result reproduced in Fig. 6.3b in this document.

The tool was also used to produce the results of a search for $H \to \gamma\gamma$ decays in a fermiophobic Higgs model [97], for the ATLAS Run 1 $HH \to bb\gamma\gamma$ search [98], and for the searches for $\gamma\gamma$ resonances [96, 17] described in Chapter 8. Outside the Higgs group, it was used to produce the results of searches for new exotic resonances [99, 100].

The code base of the project is now mostly stable, with only code maintenance and minor additions as ongoing activities.

Since the time of the code's initial development, several developments in `roofit`, in particular the introduction of *workspaces*, have duplicated some of the code's core model-handling features.

[3] Fig. 12, and auxiliary Figs. 71, 75b and 88

In parallel, the RooStats project within the ROOT framework has provided a standardized version of the functionality provided by the statistical calculators.

For these reasons, future developments will likely orient themselves in the direction of closer integration with RooFit/RooStats.

5.4 Personal Contributions

The use of unbinned likelihood methods and the methods to compute discovery significances presented in Section 5.2.3 above were not widely used in ATLAS Higgs analyses when I joined the experiment in 2006. Together with A. Höcker we introduced the use of these techniques using the `roofit` package with which we had previous experience on the BaBar experiment, where such techniques were standard. The results presented in the CSC document [15] were produced using these techniques, implemented in an early version of the `Hfitter` package. I continued as the main developer of `Hfitter`, implementing the new developments introduced for the Higgs discovery effort. I also used `Hfitter` to implement the statistical models for the successive iterations of the $H \to \gamma\gamma$ analysis [12, 56] and for searches for diphoton resonances [96, 17]. I also provided support for the other efforts where `Hfitter` was used, in particular the analyses of Ref. [99], [100] and [98].

Chapter 6

Discovery of a SM-like Higgs Boson

The discovery of the Higgs boson in 2012 remains to date the highlight of the LHC physics program. It caps a decades-long effort dating back to at least 1979, when detailed studies were initiated for LEP [18], aiming to discover the Higgs boson proposed in 1964.

The first detailed ATLAS study of discovery prospects in the $H \to \gamma\gamma$ channel was the MC-based study of Ref. [101]. This formed the basis of the detailed analysis performed for the CSC document in 2008 [15], which included all the main elements of the final discovery analysis. Starting in 2010, several iterations of the $H \to \gamma\gamma$ search were then performed in data, on increasingly large datasets and using increasingly complex analysis techniques:

- the first data-based analysis was performed using the 2010 dataset, consisting of about $40\,\text{pb}^{-1}$ of data taken at a center of mass energy of 7 TeV [102].
- An updated implementation based on about $1\,\text{fb}^{-1}$ of data collected at $\sqrt{s} = 7$ TeV in early 2011 was then published in August 2011 [103]. This iteration used for the first time on data the categorization techniques proposed in the CSC document. Amusingly, the results featured a 1.6σ local excess at $m_H \sim 127$ GeV, which can probably be recognized *a posteriori* as an early manifestation of the Higgs boson, although the expected significance was only $\sim 0.5\sigma$ at the time.
- A further update with additional improvements was released in December 2011 using the full 2011 dataset of 4.9fb^{-1} [104]. The excess seen in the previous iteration grew to about 2.7σ, with only about 1.2σ expected.
- Finally, the discovery analysis [12] was published in July 2012, using 5.9fb^{-1} of data collected in 2012 at $\sqrt{s} = 8$ TeV in addition to the 2011 dataset.

6.1 Event Selection and Categorization

In the context of the Higgs discovery, two important advantages of the $H \to \gamma\gamma$ analysis were its simplicity and robustness. Photon reconstruction was performed using the method described in Section 3.3.1. The rejection of background, which constituted one of the critical aspects of the analysis, was performed effectively by applying simple rectangular cuts on the shape of the photon cluster and the isolation selections as described in Section 3.3.2. Finally, simple kinematic cuts were applied to the photons: the pseudorapidities were required to be $|\eta| < 2.37$, excluding

the transition region $1.37 < |\eta| < 1.52$ (see Section 3.2.1). The transverse momenta were required to be $E_{T1} > 40$ GeV and $E_{T2} > 30$ GeV[1]: these rather low values allowed to avoid threshold effects in the $m_{\gamma\gamma}$ distribution above 100 GeV to simplify the sideband fits, and asymmetric cuts were found to yield slightly higher sensitivity than symmetric ones. Events were triggered using a diphoton selection with energy thresholds at 20 GeV for 2011 data, and 35 GeV and 25 GeV for the leading and subleading photon in 2012 data, using loose photon identification selections. The overall signal efficiency was about 40%, with kinematic acceptance and detector efficiency factors both $\sim 65\%$ [77]. The fraction of $\gamma\gamma$ events in the data (denoted as the *purity* in the following) was about 74%, but the S/B was only about 3% [12].

To further increase sensitivity, categorizations were implemented as outlined in Section 4.4. The initial $H \to \gamma\gamma$ analysis of 2010 data did not include categories, in part due to the small number of selected events (99), but increasingly complex categorization schemes were used in each subsequent analysis iteration:

- in the first analysis of 2011 data [103], a categorization separating converted and unconverted photons was added. In addition, events were categorized as *central* (both photons within $|\eta| < 0.75$), *transition* (at least one photon in the region $1.3 < |\eta| < 1.75$ adjacent to the transition region, where photon energy calibration is degraded), and the *rest*. For unconverted photons, where the degradation near the transition region is less severe, the *rest* and *transition* categories are merged, leading to a total of 5 categories. This categorization closely follows the scheme defined in the CSC analysis [15].

- A categorization based on the p_{Tt} variable, as described in Section 4.4.2, was introduced in the analysis of the full 2011 dataset of Ref. [104]. The 5 $|\eta|$-conversion categories described above, with the exception of the *transition* category, were split into subsets corresponding to $p_{\mathrm{Tt}} < 60$ GeV and $p_{\mathrm{Tt}} > 60$ GeV, resulting in a total of 9 categories

- Finally, a *dijet* category was included in the discovery analysis to select events in a VBF-like configuration, as described in Section 4.4.3. Two jets with $E_T > 25$ GeV were required within the region $|\eta| < 4.5$ (tightened to $E_T > 30$ GeV in the region $2.8 < |\eta| < 4.5$ for 2012 data), with an invariant mass $m_{jj} > 400$ GeV, and a pseudorapidity difference $|\eta_1 - \eta_2| > 2.8$. In order to suppress events with an additional central jet in the event, which occurs more rarely in VBF production than in background processes, the dijet system and diphoton systems were required to be back-to-back, with a difference in azimuthal angle $\Delta\phi_{\gamma\gamma,\mathrm{jj}} > 2.6$. This selection is very similar to the one investigated in the CSC analysis [15], the main difference being the use of the $\Delta\phi_{\gamma\gamma,\mathrm{jj}}$ to suppress events with extra jets instead of an explicit veto since it is less sensitive to the theory uncertainties associated with extra jet radiation. Separate categories were used for the 2011 data collected at $\sqrt{s} = 7$ TeV, and the 2012 data at 8 TeV. This was not performed to increase sensitivity, but rather to provide an accurate description of each dataset: in particular the background shape was not expected to be identical due to the change in collision energy, and some systematic uncertainties were also different. A total of 20 categories were thus used in the analysis.

Per-category yield, resolution and S/B values are shown in Table 6.1. The central-high-p_{Tt} and dijet categories in particular featured larger S/B than the inclusive selection, especially when accounting for the narrower signal peak: for the high-p_{Tt} categories, the S/B was about

[1] 25 GeV for the first iteration of the $H \to \gamma\gamma$ search on 2010 data [102]

Table 6.1: Number of events in data (N_D), expected number of signal events (N_S) and mass resolution FWHM for the 8 TeV categories of the $H \to \gamma\gamma$ discovery analysis [12], for $m_H = 126.5$ GeV. The S/B relative to the inclusive analysis is computed in two ways: first ("rel. (S/B)") as $(N_S/N_D)_c/(N_S/N_D)_{inc}$, which accounts for overall S/B differences. And secondly ("rel. $(S/B)_{FWHM}$") as $(N_S/N_D/FWHM)_c/(N_S/N_D/FWHM)_{inc}$, which also accounts for broader or narrower peaks in some categories. In both cases, the c subscript refers to per-category quantities, and *inc* to inclusive. Similarly, the ratio $z^{comb}_{c,exp}/z^{incl}_{c,exp}$, defined as in Eqs. 4.3 and 4.4, is computed as $Z_c/\sqrt{B_c}\sqrt{\Sigma_{Z^2}/\Sigma_B}$, where $B_c = [N_D(FWHM/60\text{ GeV})]_c$, $Z_c = (N_S)_c/\sqrt{B_c}$, $\Sigma_B = \sum_{c=1}^{n_{cats}} B_c$ and $\Sigma_{Z^2} = \sum_{c=1}^{n_{cats}} Z_c^2$. The effect of per-category differences in the background shapes is not considered. (Adapted from Table 4 of Ref. [12])

Conversion type	Unconverted				Converted					dijet	Incl.
η region	central		rest		central		rest		trans.		
p_{Tt} bin	low	high	low	high	low	high	low	high			
N_D	2945	173	12136	785	2015	113	11099	706	5140	139	35251
N_S	14.2	2.5	30.9	5.2	8.9	1.6	26.9	4.5	12.8	3.0	110.5
FWHM (GeV)	3.4	3.2	3.7	3.6	3.9	3.5	4.5	3.9	6.1	3.7	3.9
rel. (S/B)	1.5	4.6	0.8	2.1	1.4	4.5	0.8	2.0	0.8	6.9	1.0
rel. $(S/B)_{FWHM}$	1.8	5.6	0.9	2.3	1.4	5.0	0.7	2.0	0.5	7.2	1.0
$z^{comb}_{i,exp}/z^{incl}_{i,exp}$	1.5	4.8	0.7	2.0	1.2	4.3	0.6	1.7	0.4	6.2	1.2

5 times higher than the inclusive value, and 7 times higher for the dijet category. Conversely, the *transition* category featured an S/B only half as large as that of the inclusive selection. In the formalism of Eqs. 4.3 and 4.4, the categories with high S/B also provide larger contributions $z^{comb}_{c,exp}$ to the combined significance as to the inclusive significance $z^{incl}_{c,exp}$, as shown in the last row of the Table. While the ratio $z^{comb}_{i,exp}/z^{incl}_{i,exp}$ was negative for some categories with low S/B, separating these categories overall improved the sensitivity of the analysis as expected from the general arguments of Section 4.4.2. The overall improvement was 16%, with 13% coming from the η-conversion-p_{Tt} categories.

6.2 Signal and Background Modeling

The shape of the signal peak is described by the sum of a Crystal Ball (CB) shape (see Section 4.3) describing the core of the distribution, and a Gaussian component describing the tails.

The shape parameters of the CB shape were parameterized as a function of m_H using analytical functions. The coefficients for these functions were determined from combined fits to signal samples with m_H ranging from 110 GeV to 150 GeV. The procedure was repeated for all 20 categories. This allowed m_H to enter the likelihood as a signal parameter, allowing for instance the measurement of the Higgs boson mass through the procedure described in Section 5.2.4.

The signal shape depends only weakly on the underlying physics, in particular on the production mode. Modes with harder recoils such as $t\bar{t}H$ have a somewhat harder photon p_T spectrum and thus a slightly narrower mass peak. However this effect is found to be negligible compared to the large uncertainty on the mass resolution. In this analysis and its later iterations (see Sections 7 and 8), the signal shape obtained from simulated ggF production is thus used to describe

all $H \to \gamma\gamma$ decays.

The background modeling was determined following the procedure described in Section 4.2.2 in each of the 20 categories, using a *smeared MC* sample to describe the background. The tested functional forms included an exponential shape; a "double exponential" consisting of the sum of two exponentials with different slopes; a Gaussian shape, truncated to a section of its positive tail describing a falling distribution; and polynomials (defined in the Bernstein basis [105], so that the background PDF can be made positive definite by constraining the coefficients to be all positive). In low-statistics categories (high-p_{Tt} and dijet), the simple exponential was found to be sufficient. In other categories, either the Gaussian or a fourth-order polynomial shapes were used.

6.3 Systematic Uncertainties

The systematic uncertainties in the analysis can be classified as

- *Inclusive* uncertainties on the observed signal yield, including photon identification and isolation uncertainties, assumed to be fully correlated across the categories, and uncertainties on the integrated luminosities of the 2011 and 2012 datasets (4 parameters)
- *theory* uncertainties on the reference SM production cross-sections for the 5 production modes considered (ggF, VBF, WH, ZH and $t\bar{t}H$) and on the $H \to \gamma\gamma$ branching fraction. A separate uncertainty was also included on the production of ggF associated with jets in a VBF-like configuration, which contributes to the yield in the dijet category (8 parameters).
- *Migration* uncertainties on the fraction of signal in each category, due to uncertainties on the amount of material upstream of the calorimeter; on the amount of pileup (which affects the converted photon yield); on the photon energy scale (affecting the p_{Tt} spectrum); on the jet energy scale; and on the association of jets with the primary vertex (the latter two affecting the event yield in the dijet category) (5 parameters).
- *Photon energy calibration uncertainties* affecting the diphoton mass scale and mass resolution, implemented as changes in the shape of the signal PDF (1 parameter in addition to those already mentioned).
- *Spurious signal*: determined as described in Section 4.2.2, and assumed to be uncorrelated between categories due to different kinematic selections, but correlated between 2011 and 2012 in spite of the CM energy change (10 parameters).

The leading systematics are the uncertainty on photon identification ($\sim$10%), and the effect of the mass resolution uncertainty on the signal yield. The relative uncertainty on the mass resolution itself was estimated to be 14%, with a relative impact on the signal yield of about half this value (as estimated from the final Run-1 $H \to \gamma\gamma$ analysis of Ref. [55], presented in Chapter 7).

6.4 Statistical Modeling

The statistical model is implemented following Eq. 5.5, using the signal and background shapes described above. The model includes the signal strength μ and the Higgs boson mass m_H as

parameters of interest, and 58 unconstrained nuisance parameters (obtained from the data) describing the background yield and shape in each category. The model also includes 18 parameters describing systematic uncertainties, constrained as described in Section 5.1.3. The full model therefore consists of 88 parameters, combined into 1618 expressions. A graphical representation is shown in Fig. 6.1.

6.5 Results

The $m_{\gamma\gamma}$ spectra of the 2011 analysis of Ref. [104] and the discovery analysis of Ref. [12] are shown in Fig. 6.2. The discovery p-values as a function of m_H for the discovery analysis, computed following the method of Section 5.2.3, are shown in Fig. 6.3. A significance of 4.5σ was observed at $m_H = 126.5$ GeV. This yielded a combined significance of 5.9σ after combination with the $H \to ZZ^*$ and $H \to WW^*$ decay modes, which led ATLAS to claim, together with CMS, the discovery of a Higgs-like boson. The global significance was 5.3σ, considering the range $110 < m_H < 150$ GeV that corresponded approximately to the region of m_H-space that was not excluded at 99% CL by earlier searches. The $H \to \gamma\gamma$ analysis was the leading contributor to the discovery, both due to its large observed significance and the robustness of the result (a 3.4σ significance is obtained without categorization).

The fact that the $H \to \gamma\gamma$ benefited from a much larger $H \to \gamma\gamma$ yield than expected (4.5σ observed vs. 2.5σ expected significance) was a contributing factor in the earlier-than-expected discovery of the Higgs boson with only $\sim 11\,\text{fb}^{-1}$ of data collected at 7 and 8 TeV, compared to the earlier estimation of $30\,\text{fb}^{-1}$ of data at 14 TeV shown in Fig. 2.1b. This rather lucky outcome was foreshadowed by the presence of the clear excesses already visible in 2011 data, as already discussed above.

In addition to the p-value, the signal strength was measured to be $\mu = 1.9 \pm 0.5$ at $m_H = 126.5$ GeV using the method presented in Section 5.2.4. The value was higher than the $\mu = 1$ expected in the SM, but remained in agreement.

Finally, the $H \to \gamma\gamma$ discovery analysis also allowed a first glance into the couplings properties of the newly-discovered boson, thanks to the dijet category. While initially introduced to improve sensitivity for the discovery, this category could also be used to perform a separate measurement of the signal yield in the VBF production mode, which contributed about 70% of the signal in this category. Following the method presented in Section 4.4.3, separate signal strengths $\mu_{ggF+t\bar{t}H}$ and μ_{VBF+VH} were defined respectively for the ggF and $t\bar{t}H$ production modes (which in the SM are associated to the coupling of the Higgs to the top quark) and for the VBF and VH modes (associated to the coupling to vector bosons). The event yield in each category can be parameterized as a function of these two parameters instead of the overall μ. This accounts for the fact that the dijet category includes significant contamination from ggF, and that (to a lesser extent) the high-p_{Tt} categories include a sizable VBF contribution. The result is shown in Fig. 6.3b. The two signal strengths can be seen to be strongly anticorrelated due to the effect of the ggF contamination in the dijet category. This first glance into couplings properties formed the basis of the comprehensive exploration of the topic in the later iteration of the analysis described in the next chapter.

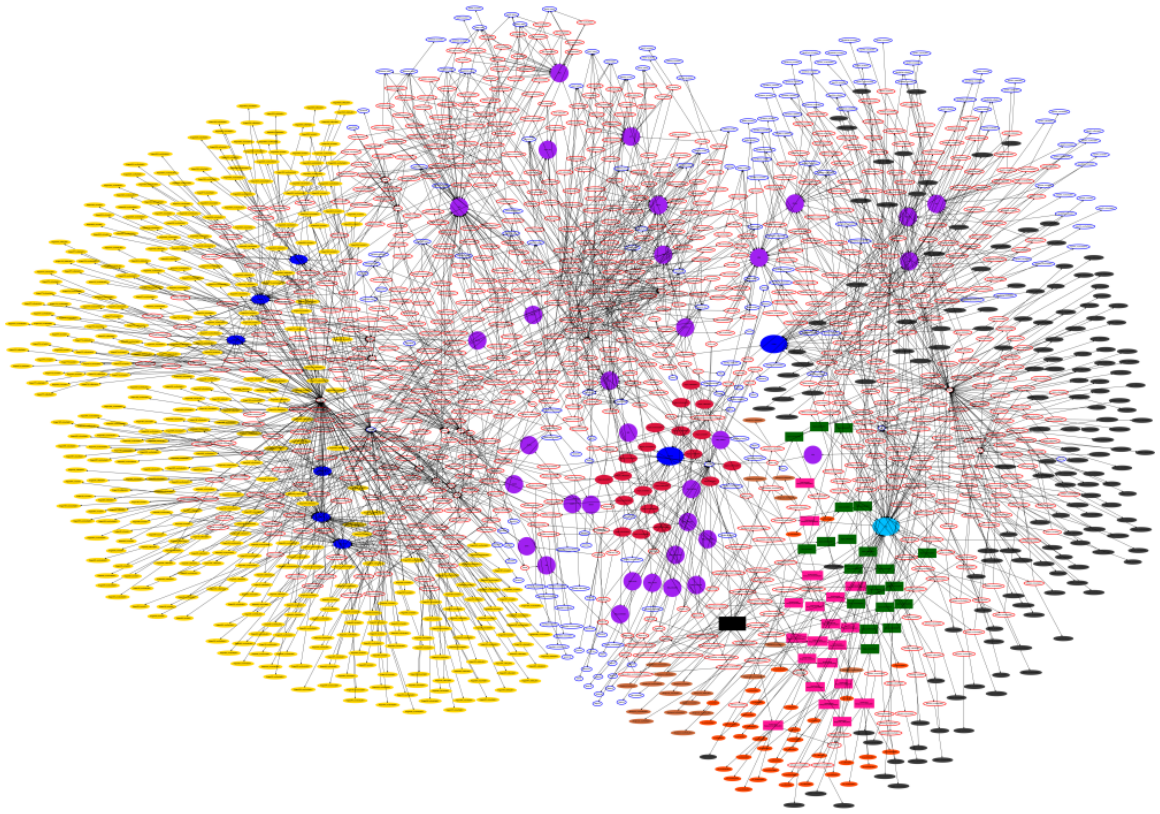

Figure 6.1: Graph representation of the model used in the $H \to \gamma\gamma$ discovery analysis. Each node represents either a numerical value, an expression or a PDF. The black box is the top-level PDF, the green boxes are the signal PDFs for each category, and the pink boxes are the background PDFs. The bottom part of the graph describes the background: the brown ellipses are the background normalization parameters, while the orange ellipses are the shape parameters. The dark red ellipses are the signal normalization expressions, and the blue ellipse in the center represents the μ parameter. The left part of the graph is devoted to the parameterization of SM signal yields: the gold ellipses are the coefficients of the parameterization, while the blue ellipses are per-mode μ parameters. The right side of the plot describes the signal shape: the dark gray boxes are the signal shape parameters, the blue ellipse represents m_H, and the cyan ellipse is $m_{\gamma\gamma}$. Finally, the purple ellipses represent the nuisance parameters associated with systematic uncertainties, and the white boxes with blue outlines are the parameters describing the uncertainties. The red-lined boxes are the expressions that bind the model together.

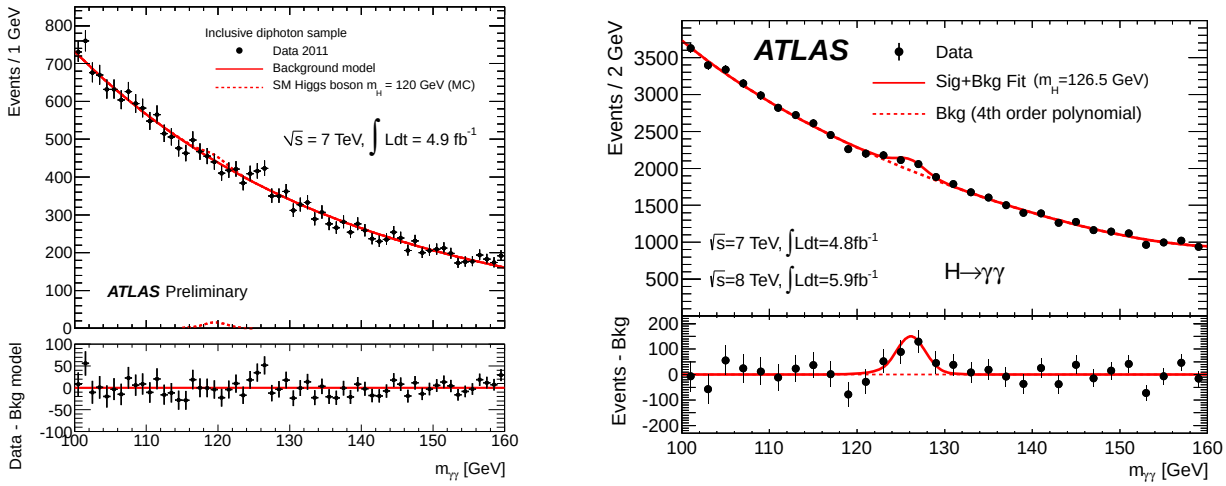

(a) (b)

Figure 6.2: Distributions of the invariant mass of diphoton candidates after selection from (a) the analysis of $4.9\,\mathrm{fb}^{-1}$ of data at $\sqrt{s} = 7$ TeV [104], and (b) the discovery analysis. (From Refs .[104] and [12] respectively)

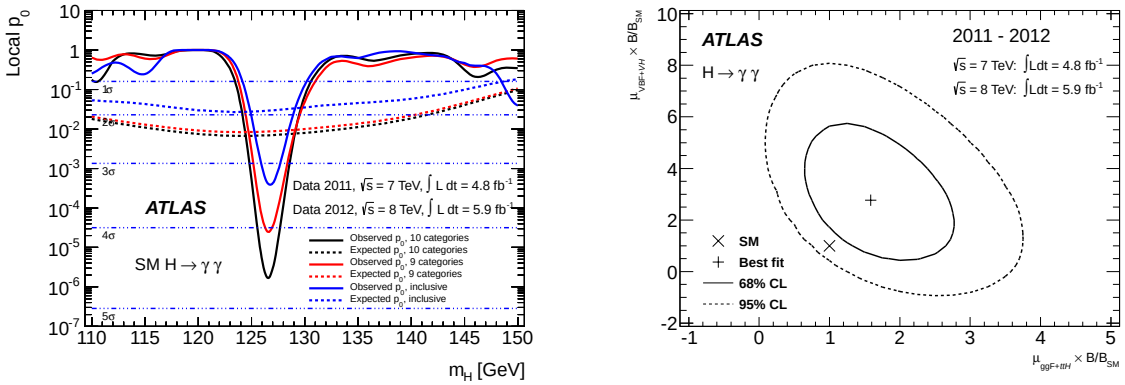

(a) (b)

Figure 6.3: (a) The observed local discovery p-value as a function of m_H for the discovery $H \to \gamma\gamma$ analysis [12] for the nominal categorization (black), a 9-category model without the dijet category (red) and the non-categorized case (blue). Dashed curves show the expected p-values under the hypothesis of a SM Higgs boson at that mass. (b) Likelihood contours in the plane of $(\mu_{gg\mathrm{F}+t\bar{t}H}, \mu_{VBF+VH})$, where $\mu_{gg\mathrm{F}+t\bar{t}H}$ is the signal strength applied to the ggF and $t\bar{t}H$ modes, while μ_{VBF+VH} is applied to the VBF and VH modes. The best fit to the data (+) and 68% (solid) and 95% (dashed) CL contours are also indicated, as well as the SM expectation (×). (From Ref. [12])

6.6 Personal Contributions

Many features of the discovery analysis followed the general strategy discussed in Section 4 which I helped design for the CSC document [15]. The categorization in particular followed closely the CSC strategy outlined in Section 4.4.

At the time of the discovery, I was the co-editor of the internal support notes [106, 107] documenting the statistical modeling of the analysis. I also provided one of the implementations of the statistical model used to produce the final results of the analysis. This model was mostly used as a cross-check, but also to produce some of the results of the analysis, in particular the two plots shown in Fig. 6.3 discussed in the previous section.

Chapter 7

Higgs Property Measurements Using $H \to \gamma\gamma$

7.1 New Physics in the Higgs Sector

The discovery of a new resonance at 125 GeV that was the topic of the previous chapter represented a milestone in particle physics, but it also raised new questions. The most immediate question concerned the nature of the new particle. The discovery analysis already showed that its main production and decay rates were all in rather good agreement with those expected from the SM Higgs boson. Measurements of the spin and parity of the new boson also showed a strong preference for the 0^+ assignment [76], leading to the new resonance being dubbed "*a*[1] Higgs boson" [108].

If however it turns out that the new state is in fact *the* Higgs boson of the SM, its discovery could paradoxically have negative implications for the other main physics objective of the LHC, the search for new physics beyond the SM. As noted earlier, the value of m_H near 125 GeV is in excellent agreement with global fits of SM parameters [109]. It also fulfills stability constraints on the Higgs potential for energies up to the vicinity of the Planck scale [16].

Fortunately this may not be the whole story. The Higgs sector of the SM includes the minimal particle content necessary to break electroweak symmetry, and it could thus simply be the low-energy effective theory [110] of a model with new physics somewhere above the electroweak scale. Common examples include weakly-coupled models such as the Minimal Supersymmetric Standard Model (MSSM), or more generally two-Higgs-doublet models (2HDM) [111], and models with new strong couplings such as the MCHM [112]. These models can all accommodate a Higgs-boson-like particle near 125 GeV, but with couplings that could deviate from their SM expectation.

Some arguments, such as the naturalness of m_H (see Section 9.1) or the presence of a suitable dark matter candidate, suggest that the new physics scale should perhaps lie not far above the electroweak scale. Ideally, at least some of the higher-energy states would thus be accessible at LHC, a possibility that is considered in Chapter 8. If however they are not, measurements of Higgs couplings could (along with other precision measurements, for instance in the flavor sector [113]) be the main probe of new physics in the foreseeable future. Understanding the properties of the new resonance, while a worthy objective in its own right, is therefore also a

[1] emphasis mine

critical piece of the second aspect of the LHC physics program outlined in the introduction, of searching for new physics beyond the Higgs boson.

Higgs boson coupling measurements are ultimately performed by combining information from its various decay channels. The $H \to \gamma\gamma$ analysis alone can however already provide detailed information on couplings. In particular, it allows the separate measurement of Higgs production in all 5 of the main channels at LHC (ggF, VBF, WH, ZH, and $t\bar{t}H$) in a single analysis using categorization techniques. The precision of these measurements is generally competitive with measurements in other decay channels, in particular thanks to the large $H \to \gamma\gamma$ event yield.

The $H \to \gamma\gamma$ measurement of Higgs production yields using the full Run 1 dataset is briefly presented in Section 7.2 below, focusing on the differences with the very similar analysis described in the previous chapter. Section 7.3 shows the combination of these results with those obtained in other decay modes.

7.2 Measurement of Higgs Boson Couplings using $H \to \gamma\gamma$

Following the Higgs boson discovery, the $H \to \gamma\gamma$ analysis was split into separate analyses dedicated to the measurement of the Higgs boson mass [70], spin [76] and couplings [55], the latter of which is briefly presented here. Compared to the discovery analysis, the couplings analysis featured a re-optimized VBF selection, aiming not for higher discovery potential but for higher sensitivity to VBF production. An important aspect of this shift of focus concerned the contribution of ggF production to the VBF selection. This is a background to measurement of the VBF yield, making up about 30% of the Higgs events selected in VBF-like topologies; since the process involves two additional jets compared to the baseline ggF process, it also suffers from large theory uncertainties [114, 115]. Reducing this contamination was therefore one of the main goals of the reoptimization of the VBF selections, which is presented in Section 7.2.1 below.

Separate categories were also introduced to select VH and $t\bar{t}H$ production, using the same techniques as the other analysis categories. These are briefly described in Section 7.2.2

Events not selected by any of the above selections are referred to as *untagged*. These events were categorized using a simpler scheme than the one used in the discovery analysis, retaining only the separation between central and non-central photons at $|\eta| = 0.95$ and between low and high diphoton p_{Tt} at 70 GeV, for a total of 4 categories.

Other changes to the analysis included a switch to *relative* photon E_T cuts, namely $E_{T1} > 0.35 m_{\gamma\gamma}$ and $E_{T2} > 0.25 m_{\gamma\gamma}$ respectively for the leading and subleading photon. The effective cut values for $m_{\gamma\gamma} \sim 125$ GeV remain close to those used in the discovery analysis (see Section 6.1). The switch was initially performed to unify the selection with that of the spin measurement, where such selections are preferable due to the correlation between $E_{Ti}/m_{\gamma\gamma}$ and $\cos\theta^*$[2]. It was also found that the ensuing background shape could be modeled with simpler functions: using simple exponential shapes in most cases, and in the remaining cases using two-parameter Gaussian shapes (truncated to only part of their high-side tails). A secondary effect of this switch was the raising of the lower edge of the $m_{\gamma\gamma}$ range to 105 GeV, so as to keep some margin

[2] The spin measurement is performed from the distribution of $\cos\theta^*$ (see Section 4.4.2). Photon E_T cuts tend to reject events with high $\cos\theta^*$, in which the photon E_T values are asymmetric. This effect is generally $m_{\gamma\gamma}$-dependent, leading to a correlation between $m_{\gamma\gamma}$ and $\cos\theta^*$ after E_T cuts are applied, which complicates the extraction of the $\cos\theta^*$ distribution. However one can see from Eq. 4.8 that cuts on $E_{T,i}/m_{\gamma\gamma}$ have an effect on $\cos\theta^*$ which is largely independent of $m_{\gamma\gamma}$ (up to terms of $O\left(p_T^2/m_{\gamma\gamma}^2\right)$), leading to negligible correlation between $m_{\gamma\gamma}$ and $\cos\theta^*$ after application of these relative cuts [72].

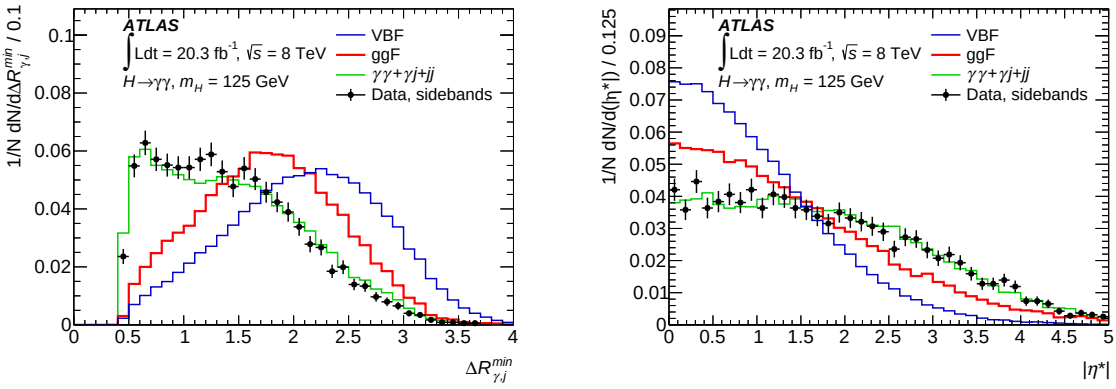

(a) (b)

Figure 7.1: Distributions of the (a) $\Delta R_{\gamma,j}$ and (b) η^* variables defined in the text, for events with $\Delta\eta_{jj} > 2$ and $\eta^* < 5$ in VBF ggF and continuum background simulation as well as data sidebands. (From Ref. [55])

with respect to the trigger E_T cuts of 35GeVand 25 GeV for the leading and subleading photon respectively. Finally, this analysis used the final Run-1 calibration of photon energies presented in Section 3.3.3, leading to reduced uncertainties on the diphoton mass scale and mass resolution. The mass resolution uncertainty, the leading experimental uncertainty for both the early Run 1 analysis and the one presented here, decreased from 21% to 11% when considering the inclusive sample [54, 55].

7.2.1 VBF Selection

In the discovery analysis, the VBF selection used simple cuts on the invariant mass m_{jj} between the two jets, their pseudorapidity difference $\Delta\eta$ and the difference $\Delta\phi_{\gamma\gamma,\mathrm{jj}}$ between the azimuthal directions of the dijet and diphoton systems (see Section 6.1). This was extended to use two additional variables:

- the minimal distance $\Delta R_{\gamma,j}$ between one of the selected photons and one of the tag jets (in R-units), which is expected to have larger values for VBF than for both continuum $\gamma\gamma$ production and ggF due to the presence of the diphoton system in the rapidity gap between the tag jets;

- the so-called *Zeppenfeld variable* [116] $\eta^* = |\eta_{\gamma\gamma} - (\eta_1 + \eta_2)/2|$, where $\eta_{\gamma\gamma}$, η_1 and η_2 are the respective pseudorapidities of the diphoton system and the two tag jets. The kinematics of VBF production lead to an enhancement for small values of η^*, while ggF and non-Higgs background have broader distributions.

These variables were shown to have little correlation with $m_{\gamma\gamma}$, as for those of the original set. Their distributions are shown in Fig. 7.1.

It was found that better sensitivity was obtained by using two VBF categories: a loose selection using the same selection as the discovery analysis, and a tighter one using the new variables as well as more stringent cuts on the other ones, with lower ggF contamination ($< 20\%$).

The cut values for the tight selection were obtained by minimizing the expected uncertainty of the μ_{VBF} measurement, using a realistic implementation of the analysis. For each set of cut values, the appropriate categorization was performed in data and simulation; a signal parameterization was obtained from simulation; the background parameterization was determined using the method of Section 6.2; finally, an Asimov dataset was generated from these parameterizations and fitted using the full analysis model to obtain the expected uncertainty on μ_{VBF}. A multidimensional optimization was then performed to determine the optimal cut values on each variable.

The μ_{VBF} sensitivity using this selection showed an improvement of about 20% [117] compared to the discovery analysis. However a similar selection, using the same two-category setup and the same variables as the study above (as well as p_{Tt}), but implementing a boosted decision tree instead of a cut-based approach showed a larger improvement and was retained for the final publication.

7.2.2 VH and $t\bar{t}H$ Selections

Six new categories were introduced in the couplings analysis to select events from VH and $t\bar{t}H$ production:

- $t\bar{t}H$ *leptonic* selection, targeting $(t\bar{t} \to l\nu jjj$ and $ll\nu\nu jj)H$: require at least one electron or muon and 1 b-jet, and veto events with 84 GeV $< m_{e\gamma} <$ 94 GeV to remove $Z \to ee$ background.
- $t\bar{t}H$ *hadronic* selection, targeting $(t\bar{t} \to 6j)H$: veto electrons or muons, require at least 5 jets with $p_T >$ 25 GeV and at least one b-jet.
- VH *dilepton* selection, targeting $(Z \to ll)H$: require 2 same-flavor, opposite-sign leptons (e or μ) with 70 GeV $< m_{ll} <$ 110 GeV.
- VH *one lepton* selection, targeting $(W \to l\nu)H$: require one electron or muon, and $E_{\mathrm{T}}^{\mathrm{miss}}$ larger than 1.5 times its uncertainty.
- VH E_T^{miss} selection, targeting $(Z \to \nu\nu)$: require missing transverse energy ($E_{\mathrm{T}}^{\mathrm{miss}}$) larger than 5 times its uncertainty, and $p_{\mathrm{Tt}} >$ 20 GeV.
- VH *hadronic* selection, targeting $(W/Z \to jj)H$: require 2 jets with 60 GeV $< m_{jj} <$ 110 GeV, $p_{\mathrm{Tt}} >$ 70 GeV, and $|\eta_{\gamma\gamma} - \eta_{jj}| < 1$.

The selections in each case were obtained by minimizing the uncertainties on the μ_{VH} and $\mu_{t\bar{t}H}$ measurements. With the addition of the two categories targeting VBF production and the 4 untagged categories, a total of 12 categories were defined in the analysis for each of the 7 TeV and 8 TeV datasets, for a total of 24 categories. The fractions of events from each production mode in each category at 8 TeV are shown in Fig. 7.2b: in most cases the selections are quite pure in their targeted production modes.

7.2.3 Results

The statistical model is defined as described in Section 4.4.3, allowing the simultaneous measurement of a separate signal strength parameter in each production mode. This corresponds to an

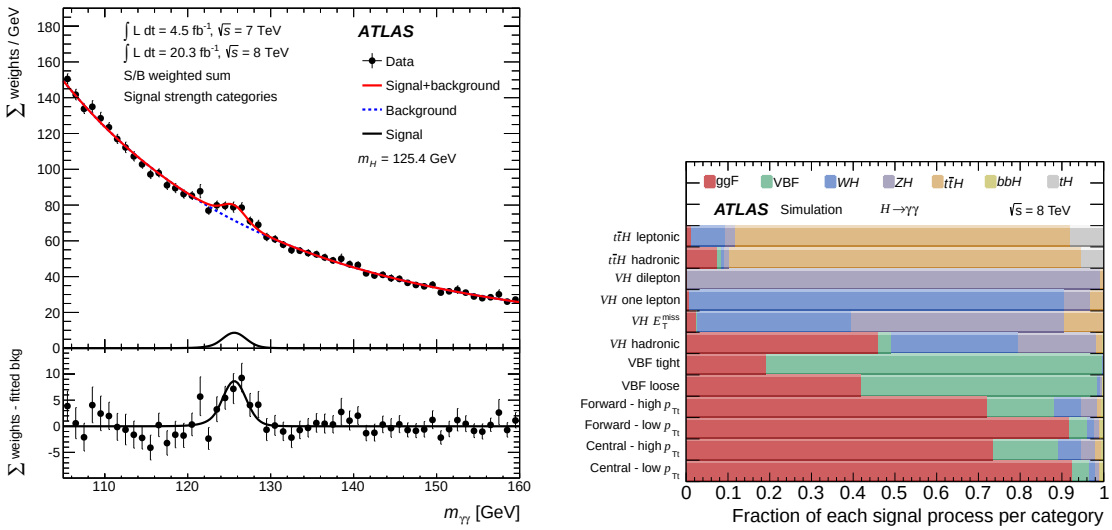

(a) (b)

Figure 7.2: (a) Diphoton invariant mass $m_{\gamma\gamma}$ spectrum observed in the sum of the 7 TeV and 8 TeV data. Each event is weighted by the signal-to-background ratio in the dataset and category it belongs to. The errors bars represent 68% confidence intervals of the weighted sums. The solid red curve shows the fitted signal plus background model when the Higgs boson mass is fixed at 125.4 GeV. The background component of the fit is shown with the dotted blue curve. The signal component of the fit is shown with the solid black curve. Both the signal plus background and background-only curves reported here are obtained from the sum of the individual curves in each category weighted by their signal-to-background ratio. The bottom plot shows the data relative to the background component of the fitted model. (b) Contribution of each production mode to the analysis categories for $m_H = 125.4$ GeV at $\sqrt{s} = 8$ TeV. (From Ref. [55])

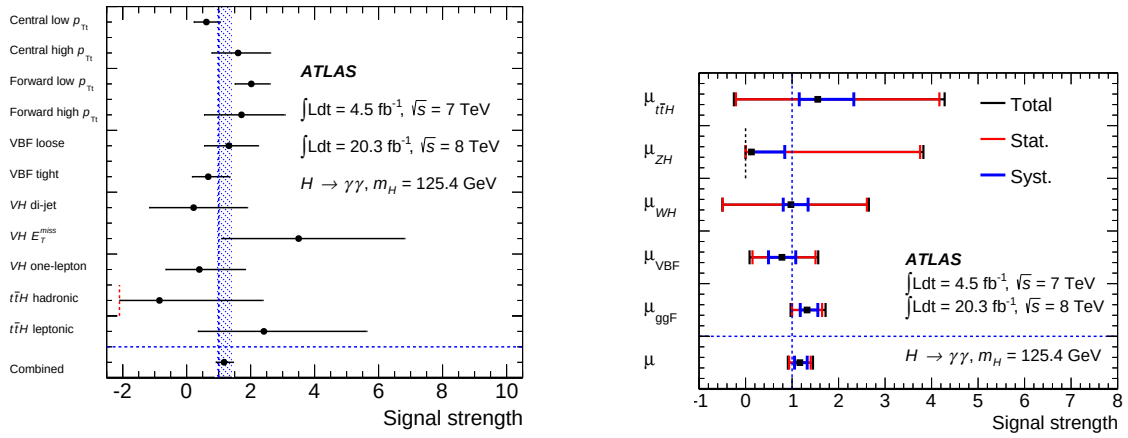

(a) (b)

Figure 7.3: Measured signal strengths, for a Higgs boson of mass $m_H = 125.4$ GeV decaying via $H \to \gamma\gamma$, combining the 7 TeV and 8 TeV data, for (a) the different analysis categories and (b) the different Higgs production modes, taking into account the contribution of each mode to each category illustrated in Fig. 7.2b. The vertical dashed line at $\mu = 1$ indicates the SM expectation. The vertical dashed line at the left end of the μ_{ZH} result indicates the limit below which the fitted signal plus background mass distribution becomes negative for some mass in the fit range. (From Ref. [55])

unfolding of the per-category signal strength measurements shown in Fig. 7.3a, using the category composition information of Fig. 7.2b. The resulting signal strengths are shown in Fig. 7.3b. These results are all in excellent agreement with the SM expectation of $\mu = 1$, with an overall level of agreement of 0.7σ with the SM.

Using a single signal strength parameter μ for all production mode yields

$$\mu = 1.17 \pm 0.23 \text{ (stat.) } {}^{+0.10}_{-0.08} \text{ (syst.) } {}^{+0.12}_{-0.08} \text{ (theory).} \tag{7.1}$$

While the statistical uncertainty is still the largest contribution, it is only a factor 2 higher than both the theory and experimental uncertainties. The theory uncertainty will decrease markedly in Run 2, due to the use of an N^3LO computation for the ggF cross-section [118, 119] and an improved combination of PDF uncertainties. The experimental uncertainty, dominated by the effect of the mass resolution uncertainty, will thus need to be significantly reduced lest it become the leading contribution to the total uncertainty by the end of Run 2.

The $\mu = 1.17 \pm 0.27$ result given above differs markedly from the value $\mu = 1.9 \pm 0.5$ obtained for the discovery analysis, which is however not directly comparable since it only used a fraction of the total 2012 dataset. More problematically, it also differs from the $\mu = 1.55^{+0.33}_{-0.28}$ obtained in Ref. [54] using the same dataset as the current result. The data were processed differently in the two cases, in particular with a change of the photon calibration scheme from the initial to the final Run 1 version (see Section 3.3.3); nevertheless the two datasets largely overlap. A compatibility test between the two results was performed using a bootstrap method, which can be applied even in the presence of such an overlap, and the probability of obtaining results at least as different as these was found to be 23%. This sizable change in the μ value is therefore

not unexpected, and can be attributed to two effects: firstly, the presence of a large positive fluctuation in the discovery dataset, already discussed in Chapter 6; and secondly the fact that even small changes in the event distribution can lead to large changes in the shape and size of the signal peak due to the small S/B ratio.

7.3 Combination with Other Higgs Decay Modes

The final stage of the study of Higgs properties involves the combination of the results presented above with those obtained with other Higgs decay modes, and with those of the CMS experiment [120]. These results are interpreted in terms of Higgs coupling modifiers, reinterpreting the signal strength values within a couplings framework based on leading-order diagrams [121]. In the most general case, a separate modifier κ is assigned to the coupling of the Higgs boson to the Z, W, t, b, τ, and μ. Separate terms κ_g and κ_γ can also be introduced to parameterized BSM contributions in the ggF and $H \to \gamma\gamma$ loops. An unmeasured BSM branching fraction BR_{BSM} can also be included under general hypotheses [122, 123]. The results are illustrated in Fig. 7.4b for the full model, and Fig. 7.4a for a simplified parameterization where only two modifiers are included for couplings to weak vector bosons (κ_V) and fermions (κ_F), following the same rationale as for Fig. 6.3b. Finally, Fig 7.5 shows Higgs coupling values as a function of particle mass, providing a clear illustration of the relations off Eqs. 2.2 and 2.3 presented in Section 2.1.

The agreement of these measurements with the SM is found to range between 11% and 88% depending on the parameterization considered, highlighting again the lack of tension between the measurements and the SM expectation. These results cement the interpretation of the new particle as SM-Higgs-boson-like, and unfortunately provide no compelling pattern of deviations that could hint towards new physics. However the deviations predicted by most realistic models are typically far smaller than the current sensitivity of the measurements. These investigations will thus need to be pursued in Run 2 of the LHC and beyond, as discussed in Chapter 9.

7.4 Personal Contributions

I was responsible for the optimization of the cut-based VBF selection, which although not retained for the final iteration of the analysis introduced some promising improvements. I took part in the investigation of the difference between the results of Ref. [54] and those of the final version of the couplings analysis discussed above. I also contributed to the investigation of the difference between the mass measurements reported in the $H \to \gamma\gamma$ channel and those of the $H \to ZZ^*$ channel in the preliminary results of Ref. [124]. I was involved in the production of results for the Moriond 2013 iteration of the analysis, using the `Hfitter` tool. I also edited the $H \to \gamma\gamma$ section of Ref. [54].

I co-convened the $H \to \gamma\gamma$ physics analysis subgroup from October 2013 to October 2014, corresponding to the finalization of the Run-1 analyses and the publication of the definitive results. Since April 2016, I am co-convening the *HComb* physics analysis subgroup, responsible for the combination of results from the various Higgs decay channels and the associated study of Higgs properties.

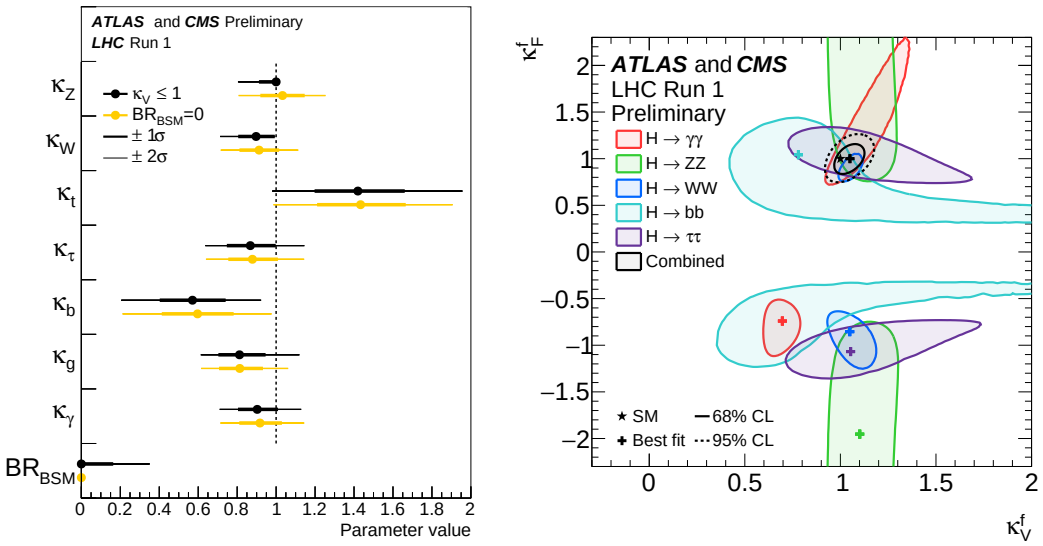

(a) (b)

Figure 7.4: Combined ATLAS and CMS results for the couplings parameterizations described in the text: (a) with separate coupling modifiers for Z, W, t, b and τ, and allowing BSM loop contributions κ_g and κ_γ to the ggF and $H \to \gamma\gamma$ loops. Additional BSM contributions to the Higgs boson width are either not included ($BR_{BSM} = 0$), or constrained by assuming $\kappa_V \leq 1$ (V = W or Z). The error bars indicate the 1σ (thick lines) and 2σ (thin lines) intervals; (b) Negative log-likelihood contours of Higgs couplings to fermions (κ_F) versus couplings to weak vector bosons (κ_V) for the individual decay channels, as well as for their global combination. The other two quadrants (not shown) are symmetric with respect to the point (0,0). (From Ref. [120])

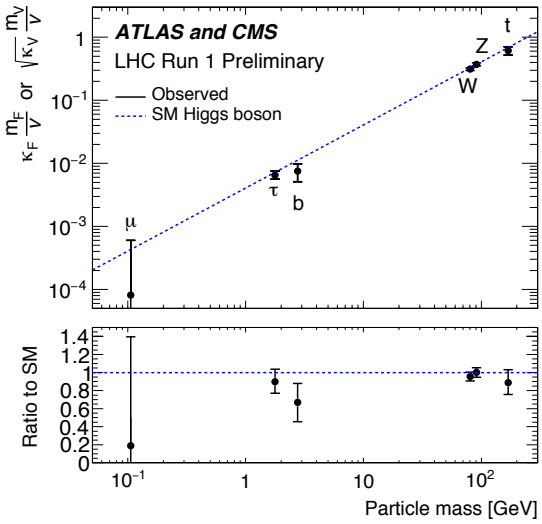

Figure 7.5: Fit results for the combination of ATLAS and CMS in the case of the parameterization with reduced coupling modifiers $y_V = \sqrt{\kappa_V}\frac{g_V}{2v} = \sqrt{\kappa_V}\frac{m_V}{v}$ for the weak vector bosons, and $y_F = \kappa_F\frac{g_F}{\sqrt{2}} = \kappa_F\frac{m_F}{v}$ for the fermions, as a function of the particle mass. The dashed line indicates the predicted dependence on the particle mass for the SM Higgs boson. The bottom panel shows the ratios of the measured values to the SM predictions. (From Ref. [120])

Chapter 8

Search for New Resonances Decaying to Two Photons

8.1 Introduction

As explained in the introduction, there are strong motivations to expect new physics at the TeV scale, in addition to the Higgs boson whose discovery and properties were discussed in Chapters 6 and 7.

No such signals have however been detected so far. Direct searches at the energy frontier using LHC Run 1 data have reached sensitivities to mass scales of about 1.7 TeV for supersymmetric models [125] and several TeV in other models [126], but in all cases no signal has been observed to date. No significant deviations from the SM have been observed either in precision measurements, neither in the Higgs couplings measurements presented in Chapter 7 nor in the flavor sector [113].

In this context, a sensible strategy is to cast the widest possible net by performing general searches based on the available experimental signatures, and expressing the result as model-independent quantities that can then be applied to any new physics model predicting a comparable signal. The search for $\gamma\gamma$ resonances away from the $H \to \gamma\gamma$ peak is a low-hanging fruit in this strategy, due to both the simplicity of the final state, and the fact that the analysis can be performed on a much wider mass range than the one used for the Higgs search without major changes.

Such searches can be motivated in several classes of models of new physics. Models with extended Higgs sectors, such as the MSSM [127, 128, 129], NMSSM [130] or general Two-Higgs-doublet models (2HDM) [111, 131] predict the existence of additional neutral Higgs bosons. These bosons could be either scalar or pseudoscalar, and could have significant branching ratios into two photons in several scenarios:

- Scalars above H: the $\gamma\gamma$ branching ratio of heavy scalar states is generically suppressed by large partial decay widths into WW, ZZ and $t\bar{t}$. However the very SM-like couplings observed so far for the Higgs boson (see Chapter 7) favor the *alignment limit* of 2HDM-type models [132, 133]. In this case Higgs couplings to W and Z, which are shared between all the CP-even Higgs states through a sum rule, are almost entirely confined to the SM-like Higgs so that the WW and ZZ decay widths of the other scalars are correspondingly suppressed. Sizable decay rates to $\gamma\gamma$ for these extra scalars can therefore be expected [134], especially for low values of the $\tan\beta$ parameter, where the $b\bar{b}$ and $\tau\tau$ decay modes are also

suppressed [135]. However this holds only below the $t\bar{t}$ threshold, above which the $t\bar{t}$ decay mode should become dominant [135, 136] (see however Section 8.4).

- Pseudoscalars above H: For pseudoscalars Higgs bosons, decays to WW and ZZ pairs are forbidden by CP conservation. This leads to sizable $\gamma\gamma$ rates in the cases where the fermionic decays are suppressed [134], in the same way as for the scalar case discussed above.

- Scalars and pseudoscalars below H: In the MSSM the presence of Higgs states below the Higgs boson is disfavored [137]. However in the NMSSM, the lightest scalar or pseudoscalar state could be in this situation [138, 139, 140, 141]; the case also occurs in 2HDM models [142, 143]. The mass of the lighter states should typically remain larger than $m_H/2$, to avoid modifications to the Higgs boson decay rates through the opening of the $H \to hh$ channel, although exceptions are possible [144]. As for the case of heavy states considered above, small $\tan\beta$ values are particularly attractive since they lead to a relative suppression of the $b\bar{b}$ and $\tau\tau$ decays channels, enhancing the $\gamma\gamma$ branching ratio [145]. In the NMSSM, the same effect can be obtained even at high $\tan\beta$ through increased singlet-doublet mixing [146]. The $\gamma\gamma$ branching ratio can also be further enhanced in the NMSSM due to new charged particles running in the decay loop [147].

In most cases, the new Higgs states are produced through gluon fusion, but VBF production can also be non-negligible [142]. One can also get sizable contributions from cascade decays of heavier Higgs states, particularly in cases where the new states lie both above and below H [141].

Constraints on low-mass scalars have been set by LEP in the $b\bar{b}$ and $\tau\tau$ decay channels [148] and with a flavor-blind search in hadronic final states [149]. However the first can be evaded in models where the $b\bar{b}$ and $\tau\tau$ decays are suppressed as discussed above, while the second provides looser bounds [146]. The large gluon-fusion production cross-sections for these states at LHC can lead, already with the Run 1 dataset, to either tighter constraints or to the discovery new states, particularly in the low-mass region.

In all the cases discussed above, the $\gamma\gamma$ partial width remains small: sizable branching ratios to $\gamma\gamma$ occur when partial widths into other final states are also small. These cases therefore also typically correspond to narrow resonances. The main focus of the search for scalar signals therefore focused initially on the regime of the narrow-width approximation (NWA), and only secondarily on the large-width case.

Diphoton signals could also occur in the decay of heavy graviton resonances in models with extra dimensions such as Randall-Sundrum (RS) models [150]. In this case the resonance could have a sizable natural width. These signals have however been excluded for masses below about 1 TeV [151].

8.2 Analysis Strategy

Two searches for spin-0 resonances are presented in this chapter: the published analysis of Run 1 data [96], using $20.3\,\text{fb}^{-1}$ of data collected at $\sqrt{s} = 8$ TeV, and a preliminary analysis of $3.2\,\text{fb}^{-1}$ of Run 2 data collected in 2015 at $\sqrt{s} = 8$ TeV [17]. A search for spin-2 resonances was also performed as part of the latter, using the RS graviton model as benchmark; it will be described briefly in Section 8.4.4. A similar search was also performed in Run 1 [151].

Both the Run 1 and Run 2 spin-0 searches were designed to primarily focus on narrow spin-0 resonances, which are well-motivated theoretically and allow to keep the analysis very similar to the $H \to \gamma\gamma$ search. This also allows to perform the search in a fully model-independent way, since the signal shape depends only weakly on the signal kinematics (see Section 6.2). To maintain this model-independence, no categorization is performed (except for the conversion-status categorization described in Section 8.3.1 which does not introduce significant model-dependence). Cross-section limits are likewise reported on fiducial cross-sections, using a fiducial volume defined to minimize model-dependence (see Section 8.3.4). The narrow width also allows to neglect interference effects between the signal and the continuum background, which can be sizable in the $\gamma\gamma$ channel due to the small S/B [152] and is model-dependent. While the main focus is on narrow scalars, the analysis retains some sensitivity to similar signals such as the RS graviton discussed above. As described in Section 8.4, the Run-2 analysis was also extended to cover signals with large natural widths.

For the Run-1 analysis, the mass range extends both above and below the Higgs boson. The lower edge of the range was chosen as the lowest achievable mass value. As discussed in Section 8.3.1, this is limited by the trigger to $m_{\gamma\gamma} > 60$ GeV. The search range can then cover $m_X > 65$ GeV, where X denotes the object of the search, allowing to cover most of the range above $m_H/2$ which is theoretically favored (see Section 8.1). The upper edge of the range is limited by the event yields needed to perform the data-driven background estimate discussed in Section 8.3.2, this allows a search range extending to $m_X = 600$ GeV. Two sources of peaking background need to be considered, in addition to the continuum background. In the low-mass region, the $Z \to ee$ component of Drell-Yan (DY) production constitutes the major background to the analysis, due to the misidentification of electrons into photons (see Section 3.3.1). And for m_X near 125 GeV, $H \to \gamma\gamma$ production must also be considered as a background.

Results are first reported as discovery p-values over the range $65 < m_X < 600$ GeV. Upper limits are reported on the signal cross-section within the fiducial acceptance.

For the Run-2 analysis, only the range $m_X > 200$ GeV was covered for simplicity, avoiding the peaking backgrounds. The upper range is however extended up to $m_X = 1.7$ TeV thanks to an improved background-modeling technique.

8.3 Run 1 Analysis

The Run 1 analysis follows closely that of the $H \to \gamma\gamma$ search presented in Chapters 6 and 7. The analysis however faces the twin additional challenges of describing the electron background from $Z \to ee$ in the low-mass region, and describing the continuum background over a large mass range in the high-mass region. To avoid compounding these difficulties, the analysis is split into two searches: a *low-mass* search targeting the resonance mass range $65 < m_X < 110$ GeV, and fitting the diphoton invariant mass range $60 < m_{\gamma\gamma} < 120$ GeV; and a *high-mass* search, targeting $110 < m_X < 600$ GeV and fitting $100 < m_{\gamma\gamma} < 800$ GeV. The fit ranges of the two analyses partially overlap, since in both cases sidebands are needed on either side of the boundary point at $m_X = 110$ GeV to perform the fits, but this has no impact on the results.

8.3.1 Event Selection and Categorization

The analysis uses the initial Run 1 photon calibration scheme described in Section 3.3.3. For both the low-mass and high-mass analyses, the photon η range is $|\eta| < 2.37$, excluding $1.37 < |\eta| < 1.52$. The *tight* photon identification selection and the track- and calorimeter-based isolation criteria described in Section 3.3.2 are applied. These selections follow closely the ones used for the $H \to \gamma\gamma$ analysis. Subsequent analysis-specific selections are described below.

As discussed above, the only categorization that is applied is the conversion-based classification described below that does not introduce model dependence. While categorizations e.g. in $|\eta|$ or p_{Tt} would increase the sensitivity, they would also spoil the model dependence of the analysis, going against the strategy described above.

Low-mass Analysis

The lower end of the m_X range spanned by the analysis is limited by the trigger: in Run-1, the lowest E_T threshold for diphoton triggers was 20 GeV for both photons. The analysis cuts were therefore set at $E_T > 22$ GeV for each photon, retaining the usual safety margin to avoid sensitivity to the trigger turn-on behavior. Values of $m_{\gamma\gamma}$ down to about 45 GeV could thus be accessible, but the proximity to the kinematic threshold leads to a change of concavity in the $m_{\gamma\gamma}$ spectrum just below 60 GeV (visible on the spectra in Fig. 8.1a) which is difficult to model. The selected mass range is therefore restricted to $60 < m_{\gamma\gamma} < 120$ GeV, as discussed in Section 8.3.2 below.

Photon candidates from the electron background are primarily reconstructed as converted photons, since these are misidentified electrons for which a track pointing towards the cluster is typically present. This feature motivates a separation of the dataset into 3 categories corresponding to both photons being unconverted (UU), both photons converted (CC), or one of each (UC). Finer-grained categorizations were found provide little additional gains in sensitivity. The fraction of events in each category depends only weakly on photon kinematics and therefore on the physics of the signal, so that this categorization does not introduce significant model dependence into the analysis.

A total of 589212 events pass the selection. The UU category provides the largest sensitivity, benefiting from both the highest signal fraction (49% of the total signal) and the lowest level of electron background (15% of total). The $m_{\gamma\gamma}$ spectra in each category are shown in Fig. 8.1a.

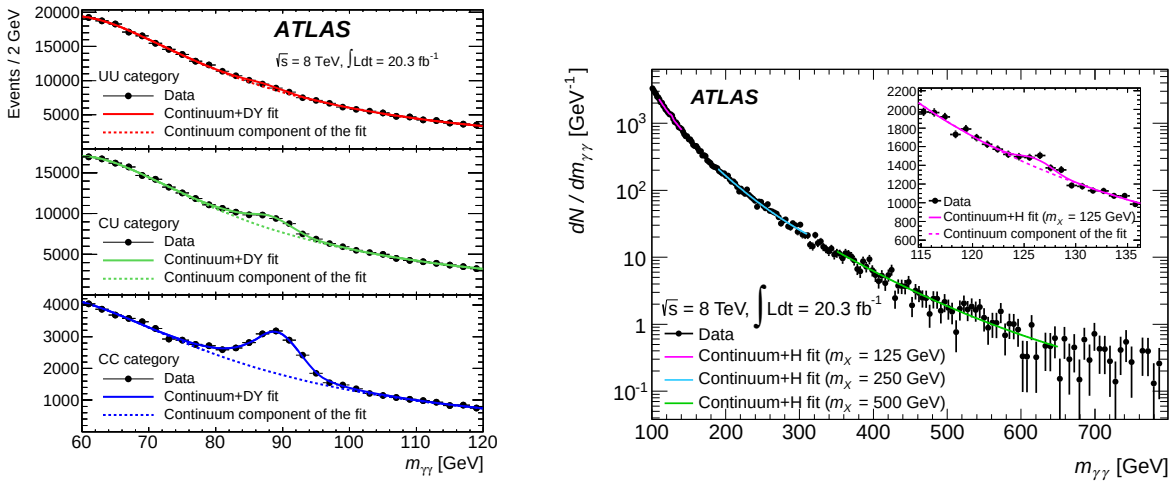

(a) (b)

Figure 8.1: Invariant mass spectra for (a) the low-mass analysis and (b) the high-mass analysis, with background-only fits overlaid. For the low-mass analysis, separate spectra are shown for the three categories defined in the text; the background includes a peaking component from misidentified $Z \to ee$ electrons. For the high-mass analysis, the sliding-window background fits are shown for several values of m_X; the inset shows the region near $m_X = 125$ GeV, highlighting the presence of the $H \to \gamma\gamma$ component of the background model. (From Ref. [96])

High-mass Analysis

For the case of a spin-0 signal, the $\gamma\gamma$ decay is isotropic in the rest frame of the decaying resonance. The E_T values of the two photons are therefore relatively symmetric, with neither differing markedly from $E_T \sim m_X/2$. The relative E_T cuts used in the final Run 1 $H \to \gamma\gamma$ analysis (see Section 7.2) are thus expected to provide better performance than fixed cuts over the wide range of m_X covered by the analysis. An optimization procedure based on the expected discovery significance was performed, leading to the selections $E_{T1} > 0.4m_{\gamma\gamma}$ and $E_{T2} > 0.3m_{\gamma\gamma}$ on the leading and subleading photon respectively.

When applying the calorimeter-based isolation selection of Section 3.3.2, a modified version of the isolation energy is used to compensate for an observed leakage of some of the energy of the photon into the isolation cone at high energy.

A total of 108654 events pass the selection, with the $m_{\gamma\gamma}$ spectrum shown in Fig. 8.1b.

8.3.2 Background Modeling

Low-mass Analysis

In order to model the electron background, both $m_{\gamma\gamma}$ templates and their normalizations are required in each category. The normalization is necessary to disentangle the signal from the electron background, since the peaking shapes of both components are similar and both normalizations cannot be simultaneously obtained from a fit to data.

The $m_{\gamma\gamma}$ templates in each category are obtained from data using events with two identified electrons reconstructed as photons. These templates are however not exactly representative of

the electron background since electrons misidentified as photons are atypical, usually undergoing large bremsstrahlung in the inner detector. A further correction determined from simulation is therefore applied. The normalizations of the templates are estimated using data-driven measurements of the misidentification rate of electrons to photons [96]. The templates are fitted using the double-sided Crystal Ball shape described in Section 8.3.3. Shape uncertainties are obtained by varying the templates within their uncertainties, fitting the resulting shapes to obtain parameterizations for each variations, and interpolating between these parameterizations using constrained nuisance parameters following the general prescription presented in Section 5.1.3.

The continuum background description follows the same method as for the $H \to \gamma\gamma$ analyses. An exponential function is found to fit the spectrum well down to about $m_{\gamma\gamma} = 70$ GeV. Below this value, the concavity of the spectrum shape changes sign due to the effect of the photon E_T cuts. Difficulty in modeling this threshold was the driving factor in raising the lower endpoint of the $m_{\gamma\gamma}$ range to 60 GeV. Above this value, the residual effect of the threshold can be modeled by adding to the exponential a component described by a Landau shape. This functional form is used in all categories and in each case the 4 background parameters (the two Landau parameters, the exponential slope, and the relative fraction of the exponential component) are left free in the fits to data. Modeling systematics are obtained using the same spurious signal method as for the $H \to \gamma\gamma$ analyses, as described in Section 4.2.2. Fits to the background-only model, including both the continuum and electron components, are shown in Fig 8.1a.

High-mass Analysis

In the high-mass analysis, the continuum background must be described over the range $100 < m_{\gamma\gamma} < 800$ GeV. Using the same spurious signal method as the $H \to \gamma\gamma$ analyses, no functional form was found to provide an acceptable description of the background over such a wide range. The analysis is therefore performed within a sliding mass window centered on the tested value of m_X. A Gaussian function (truncated to a section of its high-side tail) was used to model the background in this window. The size of the window was selected to be the largest value compatible with the spurious signal requirements $S_{spur} < 20\%\delta_S$ used in the $H \to \gamma\gamma$ analyses (see Section 4.2.2); the resulting range is parameterized as $\pm[40(m_X - 110\text{ GeV})/110 + 10\text{ GeV}]$. This method is however limited by the requirement that the fit window should contain enough events in data to reliably estimate the background yield, which limits the mass reach of the analysis to $m_X < 600$ GeV. Since the size of the fit window at this point is about ± 200 GeV, this also drives the limit on the upper value of the $m_{\gamma\gamma}$ range at 800 GeV. Modeling uncertainties were computed for each m_X value using the spurious signal method, yielding values ranging from about 20 events at $m_X = 100$ GeV to about 1 event at $m_X = 600$ GeV.

In addition to the continuum background, the analysis needs to account for $H \to \gamma\gamma$ production near $m_X = 125$ GeV as an additional *background* contribution. The shape of the Higgs boson peak was modeled using the same double-sided Crystal Ball shape as that used for the signal, described in Section 8.3.3 below. Systematic shifts in the position and width of the peak were implemented in the same way as for the $H \to \gamma\gamma$ analysis. The value of the Higgs mass was fixed to $m_H = 126.5$ GeV, the best-fit value for the $H \to \gamma\gamma$ mode at the time of the analysis [54]. The normalization of the peak is fixed to the SM expectation, $\mu = 1$. The alternate choice of using the best-fit μ value from the $H \to \gamma\gamma$ analysis was considered, but this would have led to deviations from $\mu = 1$ being absorbed into the Higgs component. The use of $\mu = 1$ allows these deviations to be treated as signals for extra states with $m_X \sim m_H$, which was considered a more

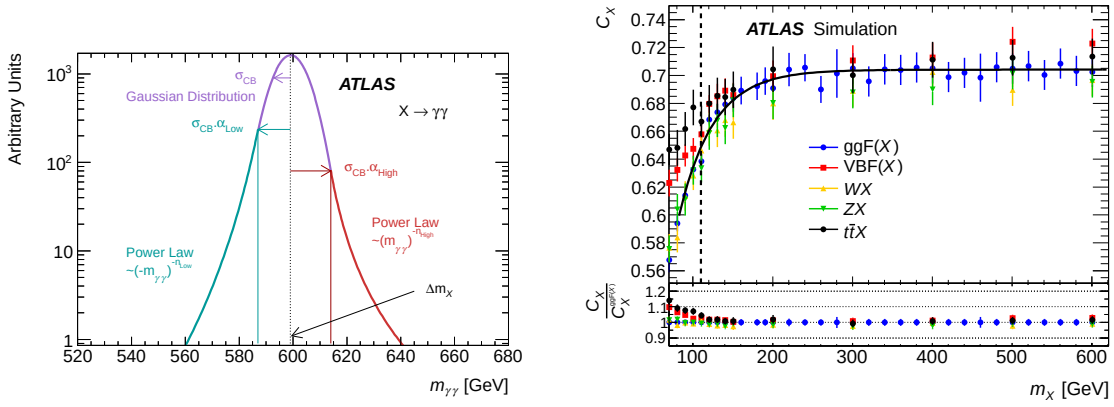

(a) (b)

Figure 8.2: (a) Illustrative diagram of the double-sided Crystal Ball (DSCB) shape. The parameter $\Delta m_X = \mu_{CB} - m_X$ is the offset between the peak position μ_{CB} and the true mass m_X; σ_{CB} is the width of the Gaussian part of the shape; α_{Low} (α_{High}) is the position of the transition between the Gaussian and power-law forms on the low (high) mass side, in units of $(m_{\gamma\gamma} - \mu_{CB})/\sigma_{CB}$; and n_{Low} (n_{High}) is the exponent of the corresponding power-law. (b) Values of the C_X factor described in the text as a function of m_X for various production modes. The solid line shows a fit to the ggF values, and the inset the ratios of the values for other production modes to those for ggF. (From Ref. [96])

interesting interpretation.

A background-only fit to the data, including both the continuum and Higgs components, is shown in Fig. 8.1b.

8.3.3 Signal Modeling

The shape of the signal at high m_X values typically includes a high-side tail in addition to the usual low-side tail modeled in the $H \to \gamma\gamma$ signal. The sum of a Crystal Ball and a Gaussian shape, used in the $H \to \gamma\gamma$ analysis, cannot provide an appropriate modeling of this high-side tail. A double-sided Crystal Ball shape is used instead, consisting of a Gaussian core analytically continued on each side by power law tails. The shape is illustrated in Fig. 8.2a.

As for the $H \to \gamma\gamma$ analysis, the mass dependence of each shape parameter is parameterized as a function of m_X, and the coefficients of the mass-dependence are obtained by a simultaneous fit to signal samples at various m_X values. The samples used correspond to the Higgs-like ggF, VBF, WX, ZX and $t\bar{t}X$ production modes, generated as for the Higgs signal except for a different mass value, and a natural width that is kept constant at $\Gamma_X = 4$ MeV above $m_X = 150$ GeV (below this value, the width of a SM Higgs boson of mass m_X is used). No significant difference in the shape of signal is observed between these modes, and a single parameterization is thus used without incurring model dependence. No uncertainty on the signal peak position is considered. The leading systematic uncertainty on the signal shape is the effect of the photon resolution uncertainty on the peak width, ranging from 10% to about 40% at the upper end of the mass range.

8.3.4 Fiducial Cross-section Definition

The signal yield is reported in terms of a cross-section within a fiducial volume defined at truth level. It is defined as

$$\sigma_{fid} = \frac{N_{obs}}{/} C_X \mathcal{L}, \tag{8.1}$$

where N_{obs} is the number of observed signal events, $\mathcal{L}$ the dataset luminosity, and $C_X = N_{MC}^{sel}/N_{MC}^{fid}$ is the ratio of the number of events passing the event selection to the number of events passing the fiducial selection in a signal MC sample at generator level. Following this definition, σ_{fid} includes a factor for the branching ratio of $X \to \gamma\gamma$.

The fiducial selection is chosen to correspond as closely as possible to the event selection, to minimize the model dependence; it is defined by the conditions $E_{T1}^{true} > 0.4 m_X$ and $E_{T2}^{true} > 0.3 m_X$ on the transverse energies of the leading and subleading photons at truth-particle level, and the condition $|\eta_{1,2}^{true}| < 2.37$ on their pseudorapidities. An isolation energy calculated at truth-level is also required to be less than 12 GeV, the value corresponding to the isolation selection cut at reconstruction level. With this definition, the factor C_X mainly corrects for the photon detection efficiency within the fiducial acceptance, which is approximately model independent. The remaining part of the usual efficiency correction, the model dependent acceptance factor $A_X = N_{MC}^{fid}/N_{MC}^{total}$ can be computed within a purely theoretical setting without experimental input to compare particular models to the cross-section limits.

The residual model dependence is tested using the ggF, VBF, WX, ZX and $t\bar{t}X$ samples described in Section 8.3.3 above, which probe a variety of final state configurations. The corresponding C_X factors are shown in Fig. 8.2b, showing close agreement between the different samples at large m_X, and agreement within 15% at lower m_X. The isolation condition included into the definition of the fiducial volume as described above is critical in ensuring this agreement: the higher levels of jet activity in final states such as $t\bar{t}X$ lead to a lower efficiency for the photon isolation condition, and would lead to a lower C_X value if not for the corresponding lower efficiency of the fiducial isolation condition.

8.3.5 Results

Separate statistical models for the low-mass and high-mass analyses are built in the same way as for the $H \to \gamma\gamma$ analysis using the `Hfitter` framework. In each case the model includes a signal component, and two background components: the electron background in the low-mass region, the $H \to \gamma\gamma$ background in the high-mass region, and the continuum component in both cases. Systematic uncertainties are included as for the $H \to \gamma\gamma$ analysis. Similarly to the latter, the leading systematic uncertainty is the mass resolution systematic discussed in Section 8.3.3. Other sources include the residual model dependence of the C_X factor (up to 15% at low mass) and the uncertainty on the electron background near the Z mass (9% to 25%).

Discovery p-values are computed as a function of m_X in both the low-mass and high-mass region using the `Hfitter` implementation of the techniques described in Section 5.2.3, and shown in Fig. 8.3. Two excesses with a local significance of about 2σ are observed at $m_X = 201$ GeV and $m_X = 530$ GeV. Such an occurrence is however likely due to the combination of the small width of the signal peak and the wide mass range in which the search is performed, leading to a large trials factor. This can usually be accounted for by computing the *global* p-value of the excess using the method of Ref. [90], as discussed in Section 5.2.3. The method cannot however be reliably applied in this case due to the very large value of the trials factor, but the global

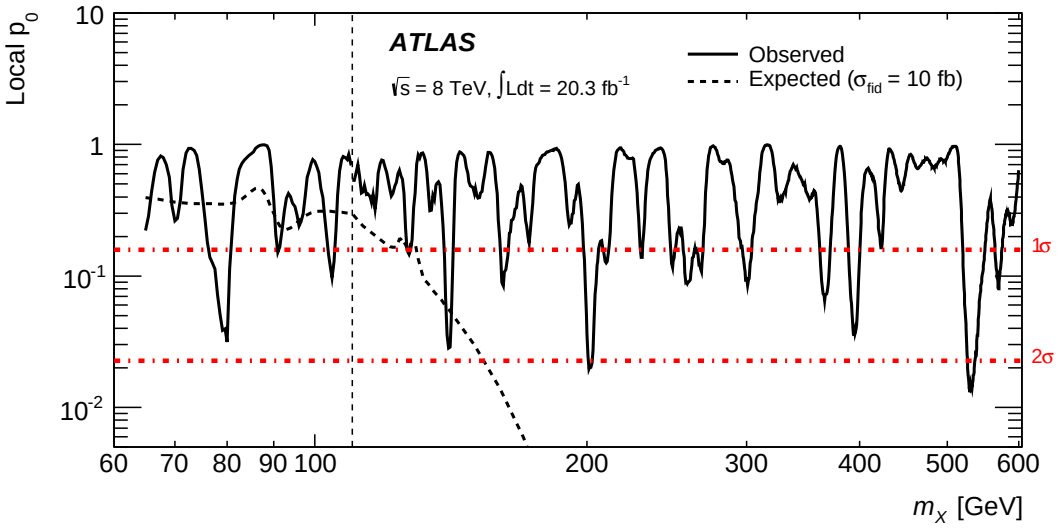

Figure 8.3: Observed (solid line) and expected (dashed line) discovery p-values as a function of m_X, where the expected p-value is computed for $\sigma_{fid} = 10\,\text{fb}$. The dotted line at $m_X = 110$ GeV show the transition between the low-mass and high-mass analyses. (From Ref. [96])

significances of each of the two excesses can in any case be shown to be less than 0.5σ. An m_X-dependent limit is therefore set on the fiducial cross-section σ_{fid}. The method of Section 5.2.4 is used, as implemented within `Hfitter`. The limits range from about 20 fb in the low-mass region to about 1 fb for $m_X = 600$ GeV. The result has already been shown in Fig. 5.3 in Section 5.

These results are used to set constraints on models of BSM physics [153, 154, 155, 156, 157, 158, 159, 160, 161, 155, 134]. In Ref. [134], the excesses observed at $m_X = 201$ GeV and $m_X = 530$ GeV are also interpreted in the context of the aligned 2HDM models discussed in Section 8.1. It can also be noted that the B.1 benchmark point of Ref. [141] is excluded by the results presented here, since the cross-section of the proposed cascade production of A_s through heavy Higgs decays followed by $A_s \to \gamma\gamma$ is several 100 pb, depending on the final state. The results are reported in terms of a total and not fiducial cross-section, but simple truth-level studies yield acceptance factors of $\sim$80% which cannot result in evading the limit.

8.4 Run 2 Analysis

Following the start of the LHC Run 2 in April 2015, about $3.2\,\text{fb}^{-1}$ of data were collected from June to October 2015 at a collision energy of $\sqrt{s} = 13$ TeV. The higher collision energy leads to a higher m_X reach for searches, but also to cross-section increases at lower masses since the same m_X is obtained at smaller parton momentum fractions and thus larger parton luminosities for gluons and sea quarks.

A repeat of the $X \to \gamma\gamma$ search analysis was therefore selected as a high-priority early analysis to be performed on the 2015 dataset. Since the focus was on the high-mass region, it was decided to limit the fit range to $m_{\gamma\gamma} > 150$ GeV, avoiding for simplicity the issues associated with the $H \to \gamma\gamma$ and electron backgrounds. The lower limit of the search range was therefore set at $m_X = 200$ GeV, to ensure a suitable sideband on the left side of the peak position.

With the use of the new background estimation technique described in Section 8.4.3, the fit of the background shape could be performed over a wide $m_{\gamma\gamma}$ window extending up to $m_{\gamma\gamma} = 3.5$ TeV[1]. Prior to unblinding the analysis, it was decided that the search range would extend up to the largest observed $m_{\gamma\gamma}$ value, plus a small safety margin to provide an appropriate high sideband. The highest recorded $m_{\gamma\gamma}$ value was $m_{\gamma\gamma} \approx 1.7$ TeV, and the search was thus performed up to $m_X = 2$ TeV.

As for the Run-1 analysis, the focus of the search was narrow spin-0 resonances. However resonances with non-negligible natural width Γ_X are also possible, for example in the case of the RS graviton states mentioned in Section 8.1. The CMS collaboration has reported results for Γ_X/m_X values up to 10% using Run 1 data [162]. This upper limit on Γ_X/m_X is well motivated for several reasons. Firstly, as discussed in Section 8.1 very broad resonances are expected to be more readily accessible in decay modes other than $\gamma\gamma$. Secondly, large values of Γ_X/m_X lead to model dependent effects, in particular in the shape of the signal lineshape (see Section 8.4.2) and in the interference between the signal and the $\gamma\gamma$ component of the continuum background. The case of large Γ_X/m_X values is therefore more suited to specific model dependent searches rather than the generic search presented here.

In addition to the scalar search, another analysis targeted towards the RS graviton signal was also performed. While it used the same data and similar selections as the search presented here, it also featured significant differences in both the aims and the techniques used. While its results are briefly presented in Section 8.4.4, the rest of the section focuses exclusively on the scalar search.

8.4.1 Event Selection

The same selections $E_{T1} > 0.4m_{\gamma\gamma}$ and $E_{T1} > 0.3m_{\gamma\gamma}$ on the transverse energies of the leading and subleading photon are applied as for the high-mass Run-1 analysis, as well as the condition $|\eta| < 2.37$ on their pseudorapidities, excluding as usual $1.37 < |\eta| < 1.52$. The photon identification selection is the Run 2 version of the tight criterion described in Section 3.3.2, and the photon isolation selection uses the Run 2 criterion described in the same section. In both cases the selections were reoptimized for the ambient conditions expected in Run 2, in particular higher pileup levels. A total of 7391 events were selected in the region $m_{\gamma\gamma} > 150$ GeV.

[1] The fit being unbinned, an upper limit of the $m_{\gamma\gamma}$ range does not need to be specified – the likelihood is simply not evaluated for $m_{\gamma\gamma}$ values larger than that of the last event. The $m_{\gamma\gamma} = 3.5$ TeV value specifies the largest $m_{\gamma\gamma}$ for which the background description was validated using the spurious signal method.

8.4.2 Signal Modeling

The analysis uses several signal models: a narrow width (NW) signal was produced using the same technique as for the Run 1 analysis; several samples with larger natural width (LW) were also produced in the ggF production mechanism using the PowHeg generator, with values of Γ_X/m_X of 2%, 6%, 8% and 10%. Interference effects between the signal and the $\gamma\gamma$ background are neglected. For the NW and each of the LW samples, the same signal modeling procedure as for the Run-1 analysis is applied: the signal is modeled using a double-sided Crystal Ball function; the mass dependence of the shape parameters is parameterized using a set of coefficients whose values are determined through a simultaneous fit to signal samples for various m_X values. Samples ranging from $m_X = 200$ GeV to $m_X = 2$ TeV are used in each case. For the LW cases, the true $m_{\gamma\gamma}$ range is restricted to $|m_{\gamma\gamma}^{true} - m_X| < 2\Gamma_X$, in order to avoid sensitivity to the model dependent shape of the signal peak in the region away from m_X.

Finally, an interpolation is performed between the m_X-dependent parameterizations at different Γ_X/m_X values, using a piecewise-linear parameterization for each of the shape parameters. This resulted in a smooth signal parameterization in both m_X and Γ_X/m_X, allowing to extract from the data the best-fit values of both of these parameters.

The C_X factor is determined from the signal sample in the same way as for the Run-1 analysis. For the LW case, the signal parameterization does not fully account for the tails of the signal lineshape since it is computed using the signal template truncated to the region $|m_{\gamma\gamma}^{true} - m_X| < 2\Gamma_X$ as described above, to ensure the result is model dependent. This is accounted for in the definition of the fiducial volume for the LW case, so that the C_X factor does not strongly depend on the shape or size of the tails of the lineshape. The values of the NW C_X factor rise from about 60% at $m_X = 200$ GeV to a plateau of about 75% at high mass; for LW, the high-mass values reach about 85%. The residual model dependence, obtained by comparing Higgs-like production modes in the same way as for the Run 1 analysis (see Section 8.3.3), is found to be about 3% for the NW case and 6% for LW, and is used as a systematic uncertainty.

8.4.3 Background Modeling

The modeling of the $\gamma\gamma$ background was determined using $m_{\gamma\gamma}$ templates generated with the Sherpa generator. The γjet and jetjet components were determined using a data sample in which some of the photon identification selections were reversed, providing a sample enriched in these components. Since the event yields obtained in this way are not large enough to obtain smooth distributions, the samples are fitted to analytical functions which are then used to describe their shape. A data-driven measurement of the fraction of $\gamma\gamma$ events in the data is then used to combine the three components in the appropriate proportions. A procedure following closely that outlined in Section 4.2 is then followed: the spurious signal for the candidate background descriptions is computed not only in the nominal case, but also after varying the fraction of γjet and jetjet background, and varying the shape of the $\gamma\gamma$ component. The latter is performed by propagating to the $m_{\gamma\gamma}$ spectrum the effect of uncertainties on the parton distribution functions and the variations in the renormalization and factorization scales. The spurious signal is then evaluated as the maximum value over all variations.

Unlike the case of Run 1, a class of functions was found to provide an adequate description of the background over the range 150 GeV $< m_{\gamma\gamma} <$ 3.5 TeV, allowing the fit to be performed to the full mass range without using the sliding window techniques described in Section 8.3.2. The

functions are given by the general form

$$f_d(m_{\gamma\gamma}; a, \{b_i\}_{0\leq i<n}) = \left(1 - x^d\right)^a \exp\left(\sum_{i=1}^{n} b_i \log^i x\right) \tag{8.2}$$

with $x = m_{\gamma\gamma}/\sqrt{s}$. The form $f_{1/3}(m_{\gamma\gamma}; a, b_0)$ is found to fulfill the spurious signal criteria for m_X values above 200 GeV.

To ensure that this MC-driven choice was adequate for the data, an F-test was performed for the use of the alternate form $f_{1/3}(m_{\gamma\gamma}; a, b_0, b_1)$ with one additional parameter compared to the nominal choice. The F-test probability for the nominal choice was found to be 0.95, showing excellent agreement with the nominal and well above the predefined 0.05 threshold below which the form should have been changed to the alternate. The test was performed in mass bins with widths approximately 10 times the mass resolution, in order to ensure that the results were not affected by the potential presence of a narrow signal. The presence of a broad signal excess could however lead to the spurious rejection of a correct background model; for this reason, the F-test is only included as a temporary feature, pending further checks of the robustness of the background modeling. The corresponding spurious signal values range from 20 events at $m_X = 2300$ GeV down to 0.04 at high mass for the LW signal model with $\Gamma_X/m_X = 6\%$.

8.4.4 Results

The statistical model includes two components for the signal and continuum background, using the shapes determined in Sections 8.3.3 and 8.3.2 above. The systematic uncertainties included in the model are close to those of the Run 1 analysis. The diphoton mass calibration procedure is very similar, but the uncertainty on the mass resolution is larger due in part to the uncertainty on the amount of material added by the IBL, ranging from $^{+55\%}_{-20\%}$ at $m_X = 200$ GeV to $^{+110\%}_{-40\%}$ at high values of m_X.

The observed $m_{\gamma\gamma}$ spectrum in data is presented in Fig. 8.4, showing the presence of an excess of events for $m_X \approx 750$ GeV.

Discovery p-values are computed as a function of both m_X and Γ_X/m_X using the method of Section 5.2.3 within the `Hfitter` framework. The result is shown in Fig. 8.5. The excess observed near 750 GeV has a maximum local significance of about 3.9σ, corresponding to $\Gamma_X/m_X \approx 6\%$. A local significance of 2.9σ is observed for the NW case. A second excess is observed at $m_X \approx 1650$ GeV, with a maximum local significance of about 2σ.

The global significance for the excess near 750 GeV in the LW case can be computed as described in Section 5.2.3. This is performed while accounting not only for the range of values of m_X but also for those of Γ_X/m_X, following the procedure of Ref. [91]. The computation is done using the "brute-force" method of Section 5.2.3, scanning over $200 \leq m_X \leq 2000$ GeV and $0 \leq \Gamma_X/m_X \leq 10\%$. A global significance of $(2.0 \pm 0.1)\sigma$ is obtained, where the uncertainty reflects the limited number of pseudoexperiments used in the computation. A limit on the fiducial production cross-section times branching ratio of the new resonance is also shown in Fig. 8.6. The angular shape of the structure created by the excess at 750 GeV in Fig. 8.6a is an expected effect of the uncertainty on the mass resolution: the sharp drop-offs at 700 and 800 GeV correspond to the points where pulling the associated nuisance parameter to "catch" the excess becomes disfavored due to the penalty induced in the likelihood by its constraint term.

As discussed in Section 8.3.5, the ATLAS Run 1 analysis did not cover the mass range beyond $m_X = 600$ GeV. However the spectrum shown in Fig. 8.1b, which extends up to $m_{\gamma\gamma} = 800$ GeV,

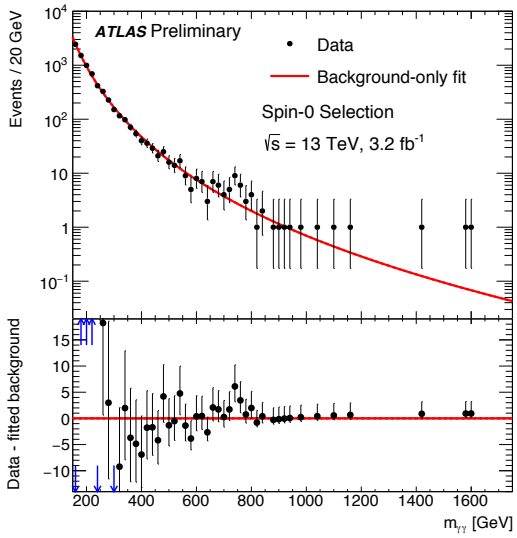

Figure 8.4: Distributions of the invariant mass of diphoton candidates for the Run 2 scalar $\gamma\gamma$ search. The red line shows the best-fit to the background-only model. The lower panel shows the difference between the data spectrum and the fit. Arrows indicate bins where the value is outside the range of the panel. (From Ref. [17])

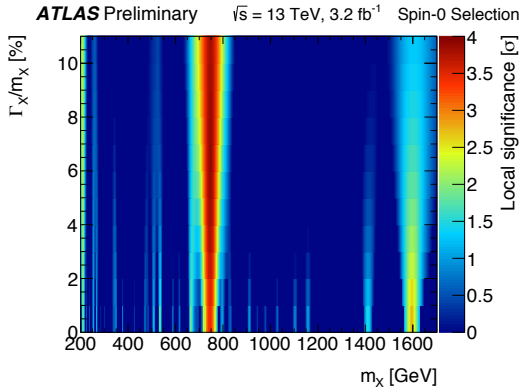

Figure 8.5: Discovery p-values for the Run 2 scalar $\gamma\gamma$ search as a function of the mass m_X and the relative width Γ_X/m_X of the signal.

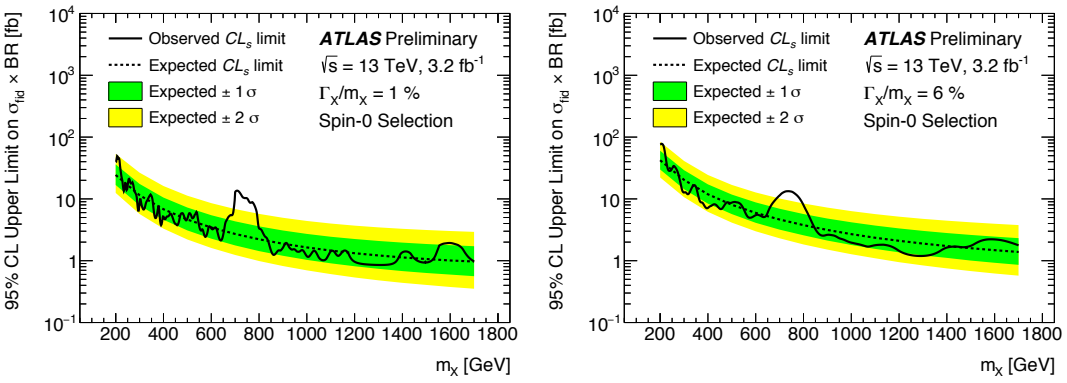

(a) (b)

Figure 8.6: Upper limits at 95% CL on the fiducial production cross-section times branching ratio of a scalar resonance as a function of the resonance mass m_X, for the cases of (a) $\Gamma_X/m_X = 1\%$ and (b) $\Gamma_X/m_X = 6\%$. The solid lines show the observed limits, the dotted lines the expected limits. The green and yellow bands denote the expected $\pm 1\sigma$ and $\pm 2\sigma$ variations of the expected limits. (From Ref. [17])

shows no large excess in this dataset. The Run 1 analysis was also originally performed using the initial Run 1 photon calibration scheme described in Section 3.3.3. In order to allow a more reliable comparison between the Run 1 and Run 2 dataset, the Run 1 analysis was therefore updated to use the final photon calibration scheme. This allows in particular better control of the correlations between the photon energy scale uncertainties in each dataset. The background model was also updated to use the functional forms of Eq. 8.2, allowing to avoid the use of the sliding-window technique and thus extending the reach of the analysis up to $m_X \sim 2000$ GeV. The resulting mass spectrum is shown in Fig. 8.7. An excess with a local significance of 1.9σ is observed for the values $m_X = 750$ GeV and $\Gamma_X/m_X = 0.06$ corresponding to the highest local significance observed in the Run 2 dataset.

As noted at the beginning of Section 8.4, the production cross-section at 13 TeV is expected to be higher than at 8 TeV due to parton-luminosity effects. The compatibility between the cross-sections of this excess observed $\sqrt{s} = 8$ TeV and the one seen at $\sqrt{s} = 13$ TeV cannot be estimated in a model independent way, but depends on the production mechanism. For the case of gluon-gluon-initiated single production, the 13 TeV to 8 TeV ratio is estimated to be 4.7, while for a $q\bar{q}$-initiated process (where $q\bar{q}$ denotes a pair of light quarks) the corresponding factor is 2.7. The continuum background is predominantly $q\bar{q}$-produced, and scales therefore with the latter number. The expected signal significance $S/\sqrt{B}$ is therefore only about 15% higher in Run 2 compared to Run 1 for a resonance singly produced from a gg initial state, and lower in the $q\bar{q}$-initiated case. The absence of a large signal in Run 1 is therefore not inconsistent with expectations in this scenario.

The compatibility of the results at 8 TeV and 13 TeV is estimated from a combined analysis of both datasets, accounting for correlations in systematic uncertainties in particular for the photon energy scale. For the case of a gg initial state, a compatibility at the 1.2σ level is found; for qqbar initial state, the corresponding value is 2.1σ.

A separate analysis of the 2015 dataset is also performed [17], targeting specifically the RS

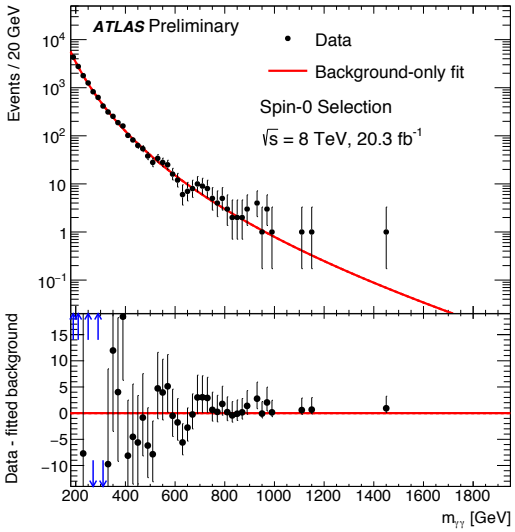

Figure 8.7: Distributions of the invariant mass of diphoton candidates for the updated Run 1 high-mass $\gamma\gamma$ search, as described in the text. The red line shows the best-fit to the background-only model. The lower panel shows the difference between the data spectrum and the fit. Arrows indicate bins where the value is outside the range of the panel.

graviton signal. The p_T spectrum of the subleading photon is softer for such a spin-2 resonance as for the spin-0 case, so the photon p_T cuts were relaxed to $p_T > 55$ GeV on both photons. An excess was also observed for $m_G \sim 750$ GeV and $k/\overline{M}_{\rm Pl} \sim 0.2$, the latter corresponding to the same width as for the spin-0 search[2].

The CMS experiment reported similar results using Run-2 dataset [163]. The search for a narrow signal reported a 2.85σ excess at $m_X = 760$ GeV and $\Gamma_X/m_X = 1.4\%$. The global significance, computed for the range $500 < m_X < 4500$ GeV, is below 1σ. However given the $\sim$0.7% uncertainty on the diphoton mass scale at this mass, the mass and width values for the excesses observed by ATLAS and CMS are in good agreement. Interestingly, a small excess at $m_X \approx 750$ GeV and $\Gamma_X/m_X \approx 6\%$ was also visible in the CMS Run-1 search [162]. A combined analysis of the Run 1 and Run 2 datasets therefore leads to a larger local significance of 3.4σ for $m_X = 750$ GeV and a narrow width, corresponding to a local significance of 1.6σ.

Although these signals are intriguing, no firm conclusion can be drawn from the currently available datasets. As already discussed in Section 8.1, resonances at $m_X = 750$ GeV are not a priori expected to decay primarily to photons. Higgs-like states should generically have much larger branching ratios to heavy fermion pairs [131], while Randall-Sundrum gravitons have been excluded up to m_X values above 1 TeV using Run-1 data [151, 162, 164]. However scenarios for such a configuration exist within the existing NMSSM [165], and many more [166] have been proposed since the appearance of the excess. A further $10\,\text{fb}^{-1}$ of data at $\sqrt{s} = 13$ TeV is expected to be delivered to both experiments by the end of July 2016, which should be able to settle the matter one way or the other. While the excess may well turn out to be due to a statistical fluctuation, it could also be the first glimpse of the physics beyond the SM that the

[2]The width of the graviton resonance can be expressed as $\Gamma_G/m_G \approx 1.44(k/\overline{M}_{\rm Pl})^2$, where $k/\overline{M}_{\rm Pl}$ is a fundamental parameter of the model.

LHC was built to discover.

8.5 Personal Contributions

The Run 1 analysis was performed almost entirely by a team of 5 researchers in which I took part, and I had a strong involvement in the design of the various aspects of the analysis. I completely implemented the building of the statistical model, and its use in producing the final results, the code used to implement the analysis selection and produce the final ntuples, and the systematics on isolation efficiency. I also designed the code used for the signal modeling, and was involved in the design of background model and the fiducial selection. For the Run-2 analysis my role was similar, with strong involvement in the statistical modeling and the production of the results, and the determination of the signal parameterization.

In 2009-2011 I had also performed another diboson resonance search together with my student Louis Helary, this time looking at $W\gamma$ and $Z\gamma$ signatures [99]. This analysis used similar analysis and modeling techniques as the $\gamma\gamma$ analyses described above. I also co-convened the Diboson Exotics (DBX) physics analysis subgroup in which this work was performed from October 2010 to October 2011.

Chapter 9

Prospects for LHC Run 2, Run 3 and Beyond

9.1 Overview

The discovery of the Higgs boson described in Chapter 6 was an important step in the understanding of the mechanism of electroweak symmetry breaking, and in particular the confirmation that it is compatible with the description provided by the SM. This success was however largely expected: as mentioned in the Introduction, a "no-lose" theorem [8] stated that the LHC experiments would likely find either an SM-like Higgs boson, or an entirely new type of physics playing a similar role. Paradoxically, the Higgs discovery thus complicates the search for new physics, since it completes the SM in the minimal way without providing further hints as to what lies beyond.

As completed by the Higgs discovery, the SM is sufficient to explain all known microscopic phenomena, up to the largest energies currently accessible. The SM could even be valid up to energies reaching the vicinity of the Planck scale [16], making the discovery of new physics (NP) far out of reach of currently conceivable collider projects [167, 168].

This suboptimal state of affairs could however be upended if the excess observed in 2015 data near 750 GeV (see Chapter 8.4) leads to a discovery. This would provide at the very least a first handle on BSM physics, and in the best-case scenario a complete new sector of physics with several new states at the TeV scale. This possibility will however be disregarded in the rest of this chapter, pending the confirmation (or disappearance) of the excess using the 2016 dataset.

Even in the absence of such clear signals of new physics, there are suggestions that some form of new physics should emerge at lower energies. One issue stands out in particular: the instability of m_H with respect to radiative corrections from much higher momentum scales, the so-called *hierarchy problem* [169, 170]. This generally leads to an unacceptably large fine-tuning in the value of m_H, if the scale for these corrections is much higher than the electroweak scale (see however Refs. [171, 172]). This issue is specific to the Higgs boson, since these corrections are not softened by underlying symmetries as they are for non-scalar elementary particles (chiral symmetry for fermions, gauge symmetry for gauge bosons). Solutions to this problem therefore typically involve new physics in the Higgs sector that generates a low Higgs mass; popular examples involve introducing a new symmetry to protect m_H (e.g. supersymmetry, as in the MSSM), or making the Higgs boson a composite rather than fundamental state (e.g. minimal

composite Higgs models [173, 174]). In most cases, this new physics must manifest itself at the TeV scale to avoid fine-tuning, and can be observed in two ways:

- Through the direct observation of new states: top partners, heavy gauge bosons, or new Higgs-like states in an extended Higgs sector. This presupposes that the masses of at least some of the new states are accessible at LHC.
- Indirectly through deviations of the properties of the Higgs boson from SM predictions. In this case the properties of the new physics could be derived from precision measurements, in the same way as the masses of the top quark [175] and the Higgs boson [34] were obtained from precision electroweak measurements. Measurements of the Higgs coupling could be similarly sensitive to the presence of new physics at energy scales above the energy reach of LHC, but low enough that they produce measurable corrections to SM predictions.

The LHC physics program aims to address these objectives in three steps:

- Run 2 (2015-2018): collect $100\,\text{fb}^{-1}$ at a center-of-mass energy of $\sqrt{s} = 13$ TeV (possibly rising to 14 TeV) and an instantaneous luminosity of $L = 10^{34}\,\text{cm}^{-2}\text{s}^{-1}$
- Run 3 (2021-2023): collect an additional $200\,\text{fb}^{-1}$ at $\sqrt{s} = 14$ TeV and $L = 2 \times 10^{34}\,\text{cm}^{-2}\text{s}^{-1}$
- HL-LHC (2026-2037): collect up to $3000\,\text{fb}^{-1}$ at $\sqrt{s} = 14$ TeV and $L = 5 \times 10^{34}\,\text{cm}^{-2}\text{s}^{-1}$

The next sections present the main directions of the proposed research program, focusing on Higgs boson couplings measurements (Section 9.2) and the search for new resonances (Section 9.3). Section 9.4 presents the analysis developments that will be needed to reach the required performance. The project is summarized in Section 9.5.

9.2 Measurement of Higgs Boson Couplings

9.2.1 Framework for Measurements

Higgs boson coupling properties have been conducted in Run 1 within the "κ framework" [121, 14]. In this scheme, a modifier κ_X is assigned to the couplings of the Higgs boson to each SM particle type. The dependence of the measured event yields (expressed as μ values as defined in Section 2.4) on the κ_X are then derived from the leading-order contributions; for gluon-fusion and $H \to \gamma\gamma$ decay processes, loops contributions are also considered. The higher-order corrections of the SM are included in the framework, so that the MS case of all κ_X equal to unity matches the best theory predictions. These corrections are however correct only in this particular case, so the framework is only valid for small deviations from the SM.

The Run-1 results in this context have already been briefly described in Section 7.3. Since the measured μ values can be generally expressed as quadratic expressions of the κ_X, the best-measured κ_X have an uncertainty of about 10%, corresponding to the ∼20% precision achieved on the μ, as illustrated in Fig. 7.4b.

In Run 2, this framework is being substantially modified. First, the use of μ values to express the measured event yields has been deprecated in favor of cross-section values. These have the advantage of decorrelating the measurement from the SM predictions which appear in the denominators of the μ, which make the latter dependent on both the specific value of the SM

prediction at the time of the measurement and on its associated uncertainty. These cross-sections may be total cross-sections for particular productions modes, or fiducial cross-sections defined to minimize the associated theory uncertainties and model-dependence (see Section 8.3.4). An intermediate definition denoted as *simplified cross-sections* has also been proposed [176], in which the measured event yields are defined in terms of cross-sections in specific regions of parameter space chosen to minimize theory uncertainties. The inputs may also more generally take the form of pseudo-observables [177, 178] defined to capture both the event yields and kinematics of Higgs production and decay.

Secondly, the higher precision of Run 2 couplings measurements requires a scheme free of the limitations of the κ framework. Two approaches are considered: the use of specific benchmark models, and a consistent treatment of deviations from the SM through an effective field theory (EFT) approach. These schemes are respectively described in Sections 9.2.2 and 9.2.3 below.

9.2.2 Benchmark Models

Benchmark models typically provide definite predictions, in terms of a few model parameters. Among the plethora of models that can be used to parameterize Higgs boson couplings, we highlight as an example the Minimal Composite-Higgs models [173, 174]. In these models, the Higgs boson is a composite pseudo Nambu-Goldstone boson (PGB) of a new strong sector based on an $SO(5)$ gauge group, broken down to the EW gauge group at a high energy scale f. Two main flavors of the models are considered, MCHM4 [173] and MCHM5 [174], differing mainly in the $SO(5)$ representation in which the SM fermions are embedded. Higgs couplings differ from those of the SM by corrections [179] of the order of the ratio $\xi = v^2/f^2$, as shown in Table 9.1. Values of $f \sim 1$ TeV correspond to $\xi \sim 6\%$, which gives a rough estimate of the required precision on the measurements of the couplings.

Table 9.1: Expressions for the modifiers of the Higgs boson couplings to gauge bosons (κ_V), and fermions (κ_F) for two flavors of the MCHM model described in the text.

Model	κ_V	κ_F
MCHM4	$\sqrt{1-\xi}$	$\sqrt{1-\xi}$
MCHM5	$\sqrt{1-\xi}$	$(1-2\xi)/\sqrt{1-\xi}$

The results for other benchmark models, including the 2HDM models already described in Section 8.1 and the hMSSM [180] are given in Ref. [181]. These predictions are easily testable using Higgs coupling measurements. However many such models exist, and are equally well-motivated in the absence of a guiding signal for new physics at the TeV scale, and testing more than a few options is impractical.

9.2.3 The HEFT Framework

If NP states are inaccessible to direct searches $\sqrt{s} = 13$ or 14 TeV, physics at the LHC would be described by the low-energy effective theory obtained by integrating out these heavy degrees of freedom, and would coincide with the SM if the new states are at much higher masses that the LHC collision CM energy. However, if the mass gap between the SM and NP is not too large,

remnants of the high-energy theory would be observable in the form of new, non-renormalizable interactions, in the same way as beta decay, mediated through non-renormalizable four-fermion interactions, is a low-energy manifestation of the W boson. Higher-order terms with the SM particle content can be classified according to their mass dimensions. Terms of lower dimension usually correspond to better prospects, since they are generically less suppressed for higher NP mass scales. Since the dimension-5 terms are irrelevant to LHC physics [182], the first terms to consider are the 59 dimension-6 operators [110, 183, 184][1]. Of these, the 30 involving the Higgs boson [186] can be constrained only at the LHC. Some of these operators induce shifts in the couplings of the Higgs boson to other SM particles. The corresponding coefficients thus constitute a more consistent extension of the κ framework described above. This parameterization also has the advantage of being agnostic with respect to the nature of the new physics, avoiding the issue of the wide range of new physics models discussed in the previous section.

Precise measurements of these couplings could be used to constrain the coefficients of the corresponding operators. Other operators induce deviations in the kinematic properties of the Higgs boson. Their coefficients could be constrained through differential cross-section measurements, in particular in the $H \to \gamma\gamma$ channel. Finally, higher-order contributions to the quartic Higgs couplings, such as that arising from the pure-Higgs $(\phi^\dagger\phi)^3$ operator, can only be probed through the double-Higgs production process. The measurements relevant to the setting of these constraints in the context of $H \to \gamma\gamma$ are discussed in Section 9.2.4 below.

9.2.4 Higgs Couplings Measurements in Run 2 and Beyond

In Run 1, Higgs boson coupling measurements were mainly obtained from measurements of event yields in various production and decay channels. These measurements are set to remain critical up to and including the HL-LHC. Other constraints from the study of the kinematics of Higgs processes, and the specific case of the measurement of the triple-Higgs coupling will also become increasingly important with larger datasets. These various measurements are discussed below.

Inclusive Measurements

Measurements of event yields in various production and decay channels form the basis of the Run 1 couplings results [14] already shown in Section 7.3. Prospects for the extension of these measurements to the HL-LHC dataset have also been studied [187], and could lead to precisions of the order of 2% and 3% on Higgs couplings to vector bosons and fermions respectively. These measurements in turn allow strict constraints on e.g. the MCHM models described in the previous section, as illustrated in Fig. 9.1. These constraints could set indirect limits on the high-mass scale f of the model to about 1 TeV.

The $H \to \gamma\gamma$ channel plays an important role in these results, providing competitive results in all the main production modes (see Table 1 in Ref. [187]). These results however depend critically on the ability to maintain systematic uncertainties at a level significantly lower than the statistical uncertainties. This will be a central part of the project described here, focusing on four main topics:

- Improve the background modeling technique to reduce the associated uncertainties (currently $2-8\%$ for the Run-1 analysis [55]) [Section 9.4.1].

[1] assuming a single generation of fermions. For 3 generations, the number grows to 2499 operators [185]

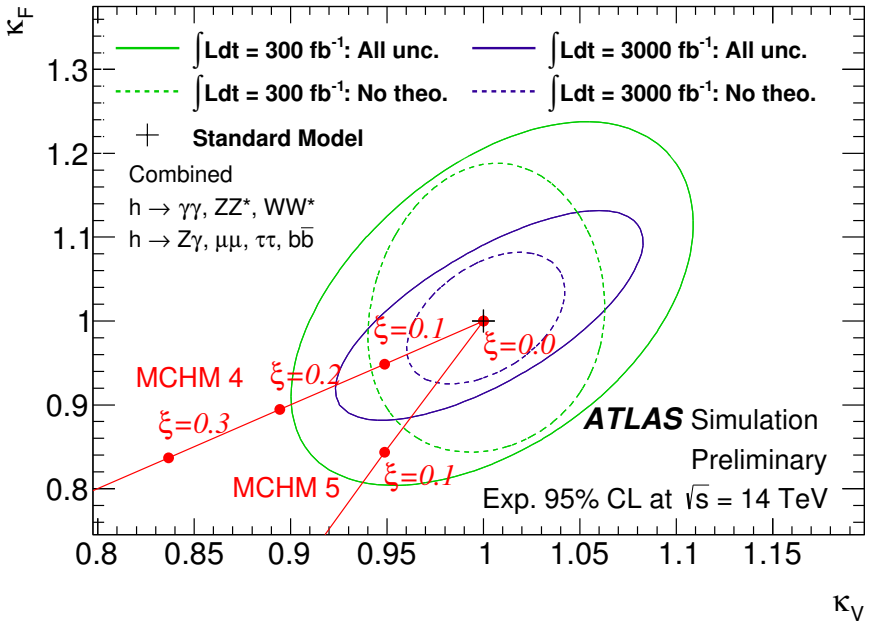

Figure 9.1: Expected two-dimensional 95% CL likelihood contours in the (κ_V, κ_F) plane for projected combination of Higgs coupling measurements. The coupling predictions in the MCHM4 and MCHM5 models (see Table 9.1) are overlaid. (Figure taken from Ref. [187])

- Improve the diphoton mass resolution and its uncertainty, currently ∼10% for the Run-1 analysis [Section 9.4.3].
- Maintain the performance of the photon identification selection in higher-luminosity environments [Section 9.4.4].
- Maintain the performance of the VBF selection at high pileup [Section 9.4.2].

The listed topics are discussed in more detail below in the sections indicated in brackets. Measurements of ratios of Higgs couplings could also be performed. These could provide better precision than the individual couplings measurements, especially in the cases where common systematic uncertainties cancel out in the ratio. Such measurements were already included in the ATLAS+CMS Run 1 couplings combination of Ref. [14].

Measurement of $HH \to \gamma\gamma b\bar{b}$ and Production in Association with b-quarks

Double-Higgs production is a critical part of the HL-LHC program, since it is the only process with direct sensitivity to the λ parameter of the SM Lagrangian (see Section 2.1). The measurement is however challenging due to the small expected event yield even at HL-LHC [188, 189, 190].

The $HH \to \gamma\gamma b\bar{b}$ mode offers the best sensitivity among the various pairs of Higgs decay modes, thanks to the clean signature of the $\gamma\gamma$ decay and the large branching ratio of $H \to b\bar{b}$. However this process is extremely rare and the expected significance of the SM signal with the full HL-LHC dataset is only 1.3σ [191] (although it can be noted that CMS expects a 1.9σ with

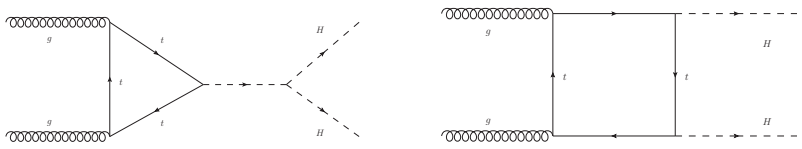

(a) (b)

Figure 9.2: Leading-order diagrams for Higgs-pair production at LHC.

the same dataset [192], when combining the $bb\gamma\gamma$ and $bb\tau\tau$ modes). The improvement of the sensitivity in this mode will be part of the project described here, focusing on two main topics:

- Improving the diphoton mass resolution and its uncertainty to increase the sensitivity of the analysis [Section 9.4.3].
- Making use of the b-tagging performance provided by the ITK to improve the reconstruction of the $H \to b\bar{b}$ decay [Section 9.4.2].
- Improving the rejection of non-photon background such as $pp \to t\bar{t}$, which represented $15-20\%$ of the total background to the analysis at $\sqrt{s} = 8$ TeV [193], and up to 30% at $\sqrt{s} = 13$ TeV due to the increased $t\bar{t}$ production cross-section [Section 9.4.4].

The primary goal of measuring λ is however complicated by the fact that the HH process of interest involving the triple-Higgs vertex (represented at leading order in Fig. 9.2a) is accompanied by a "box" HH production process (shown at leading order in Fig. 9.2b) with no sensitivity to λ. The box process has a larger amplitude and interferes destructively with the process of Fig. 9.2a, which reduces both the sensitivity to λ and the expected event yield. The uncertainty on $\lambda/\lambda_S M$ with the full HL-LHC dataset is expected to be about 5 [191]. This could however make the process sensitive to BSM effects, since modifications in the Higgs boson couplings could lead to large increases in the expected even yields by mitigating the effect of the destructive interference [190].

The objectives will be the same as those already pursued in the Run 1 analysis [98]: search for resonances decaying to two Higgs bosons ($X \to HH \to \gamma\gamma b\bar{b}$), targeting for instance heavy Higgs boson decays in 2HDM models; and in parallel search for non-resonant enhancements similar to the SM signal but with larger yields. This program thus spans a timeframe ranging from Run 2 to the end of the HL-LHC program.

Another related topic of work will involve the production of $H \to \gamma\gamma$ in association with one or more b-quarks. As noted in Section 2.2.1, this process is similar to the $t\bar{t}H$ mode shown in Fig. 2.2d, with b-quarks instead of tops. This process can provide an independent measurement of the Higgs coupling to b-quarks. Since it is the leading background to the $HH \to \gamma\gamma b\bar{b}$ process and uses similar experimental techniques, its measurement is also an intermediate step for the $HH \to \gamma\gamma b\bar{b}$ analysis. The $Hb\bar{b}$ process has a cross-section of 490 fb at $\sqrt{s} = 13$ TeV [121], yielding $\sim$113 events per 100fb^{-1}. The b-jets have typically low p_T, leading to low acceptance for these events, but this production mode should be accessible during LHC Run 3. Due to its relevance to $HH \to \gamma\gamma b\bar{b}$, this mode is also included in the project described here.

Measurements of Differential Cross-sections

The measurements of the kinematic properties of Higgs boson production have been performed using the $H \to \gamma\gamma$ in Run 1, as already mentioned in Section 4.4.4. These measurements have

been used [194] to set strong constraints on BSM physics within the HEFT framework described in Section 9.2.3. They provide natural extensions of the event yield measurements presented in Sections 9.2.4 above. The analysis technique involves a category for each bin of the targeted distribution, for which the `Hfitter` tool described in Section 5 is well-adapted. For these reasons, these measurements are included as part of the research project. A particular topic of interest is the study of associated Higgs production with one or more b-quarks, which as discussed above should have enough statistics available already in Run-3 for first measurements.

9.3 Search for New $\gamma\gamma$ Resonances

A more direct avenue of search for NP is to search directly for new resonances on the energy frontier, where the ATLAS and CMS experiments play a key role. This search is complementary to the indirect searches in two ways: firstly, the effective-theory framework in which the latter is described probes resonances beyond the mass reach of the LHC, and it is still necessary to look directly for particles with masses below this limit. Secondly, as described above the indirect searches are to reach their full potential only in the HL-LHC phase, while direct searches may yield more immediate results.

As noted above, this search may have already yielded its first prize in the 2015 dataset with the observed excess at 750 GeV. If the signal is genuine, the confirmation of the discovery could come on the timescale of the review of this document since a 5σ observation should be possible with an extra $2-3\text{fb}^{-1}$ of data in the 2016 run. The same amount of data should also allow to disprove the presence of a new resonance, if no significant excess is observed.

However the outcome of this observation will have only a limited impact on the strategy described here: the search will be pursued, motivated as described in Section 8.1, for either new states or *additional* new states. The focus will remain on the $\gamma\gamma$ final state. The search range will be extended at higher masses as the integrated luminosity of the dataset increases. The search will focus on the high end of the mass spectrum, and also in the intermediate-mass region where small excesses could have been missed with smaller datasets.

The low-mass region below the Higgs boson mass, where the presence of diphoton resonances is theoretically more favorable (see Section 8.1) will be re-investigated, following the search already performed using the Run 1 dataset. In addition to the inclusive, model-independent search already performed with Run-1 and Run-2 data, additional searches would target specific production modes. VBF-like configurations, associated production with gauge bosons or heavy quarks would be particularly interesting topics to pursue.

The associated topics of investigation, which largely overlap with those of the previous section, include:

- Improve the background modeling technique, in particular at high mass. This would aim to reduce the associated uncertainties and making the modeling robust for searches at very high masses and with possibly wide signal shapes. [Section 9.4.1]

- Improve the diphoton mass resolution and its uncertainty (currently $\sim$55% at high mass) [Section 9.4.3]

- Maintain the performance of the photon identification selection in higher-luminosity environments, in particular in the very-high-p_T regime [Section 9.4.4].

- Maintain the performance of the VBF selection at the high pileup levels of HL-LHC [Section 9.4.2].

- Make use of the improved b-tagging performance provided by the ITk [Section 9.4.2].

9.4 Work Areas

9.4.1 Improvements in Analysis Technique

Most of the analysis techniques described in Section 4, which forms the basis of all the analyses presented in this document, can be reused for further developments described in this chapter. In particular, the likelihood-based statistical treatment, as implemented in `Hfitter`, should not need any major changes. The same also applies to the signal modeling, and the implementation of signal systematics. However the background modeling technique described in Section 4.2 could be difficult to apply for datasets larger than the $100\,\text{fb}^{-1}$ available at the end of Run 2.

Two main issues could be problematic: first, the method relies on large samples of background MC to assess the true shape of the $m_{\gamma\gamma}$ distribution. This sample must by definition be much larger than the data itself, so that the residual biases (measured by the spurious signal) due to limited MC statistics are negligible compared to the statistical uncertainty in data. In Run 3, this would require samples of over a billion events, which would be difficult to process. One could consider adopting the alternative methods used in the CMS $H \to \gamma\gamma$ [195] and high-mass diphoton [163] analyses, which do not depend on large MC samples but instead use the data itself. However these methods do not seem to completely address the problem of biases with respect to the *true* $m_{\gamma\gamma}$ spectrum shape, which by definition cannot be obtained only from the data. Another approach is to rely on incremental improvements to the method: for instance computing the spurious signal at a single mass point instead of taking the maximum value over a range (see Section 4.2.2) would reduce the statistical fluctuations on the value and therefore the amount of MC required. The ratio of MC to data could be reduced to a factor $\sim$100 (down from the factor 2500 in Section 4.2.2). Given the overall scaling in computing resources expected for Run 3 and HL-LHC, maintaining such a ratio could be feasible.

The second issue concerns the functions used to model the background shape: as more data is collected, this shape will need to grow increasingly more complex in order to describe the shape with sufficient precision. Such shapes may become difficult to build from simple functions; their parameterizations may also require many free parameters, leading to increased statistical uncertainty on the signal yield. These effects may be mitigated by decreasing the fit range. The current value was chosen in part to span the full interval where the $H \to \gamma\gamma$ mode could lead to discovery. It has already been shown that now that m_H is known, the $H \to \gamma\gamma$ search could be performed on a reduced interval with no increase in total uncertainty. The interval could be further reduced as the size of the fitted datasets increase. If this is not sufficient, one could move to a background description based on MC templates, following the method used in the graviton search of Ref. [151]. This method has disadvantages, as discussed in Section 4.2.1, and also relies on large MC statistics. However it does not rely on the use of an appropriate functional form to fit the background, which may be a critical for HL-LHC. It also relies on a set of nuisance parameters that is "physics driven", each associated to a particular theory or experimental uncertainty, that would not grow in size with increasing data statistics except if new sources of uncertainty need to be considered.

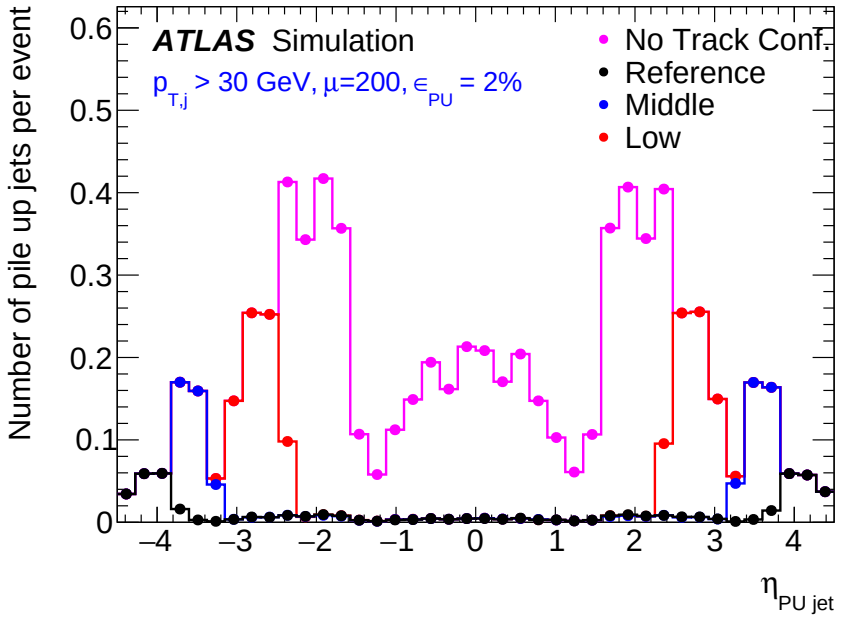

Figure 9.3: Distribution of the number of pileup jets per region of η, for the case where the jet vertex tagging described in the text is not applied (pink dots), and where it is applied using tracking coverage extending up to $|\eta| = 2.7$ (red points), $|\eta| = 3.2$ (blue points), and $|\eta| = 4.0$ (black points). (From Ref. [196]).

9.4.2 Upgrade of the Silicon Tracking System

The entire ATLAS inner tracker will be upgraded during the Phase-II upgrade. The replacement will be an all-silicon inner tracker (ITk) designed for HL-LHC conditions [196]. The main challenge is coping with the larger pileup levels, with an average of 200 expected interactions per beam crossing. The main improvements will include the use of a more radiation-hard semiconductor technology, smaller sensor sizes to mitigate the increased sensor occupancy and larger data readout and transfer rates to match increased trigger rates.

In the course of the design, it has been realized [197] that an extension of the $|\eta|$ coverage of the tracker could bring significant benefits. The current baseline design [196] extends the coverage to $|\eta| < 4.0$, from $|\eta| < 2.5$ currently. A particular benefit of this extension covers pileup rejection for the tagging of VBF jets. Pileup can be efficiently mitigated using jet vertex tagging [198], which associates jets to one of the interaction vertices in the event using tracking information. Retaining only jets compatible with the vertex of the $\gamma\gamma$ system (as determined from photon tracks and pointing information, see Section 3.3.3) thus reduces pileup contributions within the tracking volume. Since the forward jets from VBF production peak at $|\eta| \sim 3$, the extension of the tracking coverage $|\eta| = 4$ allows the reduction of pileup contamination in the VBF jet selection. This effect is illustrated in Fig. 9.3, where the pileup contributions for various values of the η acceptance are compared. The impact on the tracking coverage on the measurement of the VBF production cross-section has not been studied for the $H \to \gamma\gamma$ mode, but studies have been performance for the $H \to ZZ \to 4l$ and $H \to WW \to l\nu l\nu$ modes (see Sections IX.3.2 and XI.3.3 of Ref. [196]), showing respectively a 10% and factor 2 improvement in the sensitivity.

Another important aspect of the ITk is the improved performance of b-jet identification, which is critical in particular for the study of the $Hb\bar{b}$ mode and the search for $HH \to \gamma\gamma b\bar{b}$, as described in Section 9.2.4 above. The current ITk design is currently foreseen to give similar performance at $\mu = 200$ to the current detector during Run 1, and somewhat better performance at $\mu = 140$. (see Section IX.2.9 of Ref. [196]). However these projections are still very preliminary and depend in part on the design that will be selected.

The LAPP group is strongly involved in this upgrade through the design of a novel layout for the tracker, the Alpine stave design [199], making use of a geometry with inclined sensors to reduce the amount of silicon required to fully cover the required acceptance. It was also the first design to consider an extended coverage in the forward directions. The group is committed to contributing significantly to the design and construction of the new tracker, regardless of the choice of the final design; this effort is one of the main future directions of work for the group. Contributing to this effort is one of the aims of this project, with the objective of making use of the improvements brought by the new tracker for physics analysis at HL-LHC.

9.4.3 Improvement of Photon Energy and Resolution Measurements

The current photon energy calibration was obtained from the Run-1 dataset [53]. It is based on a multivariate calibration algorithm, using cluster energy and position information but also information on the depth of the shower. Other critical inputs include measurements of the amount of material upstream of the calorimeter, in order to properly model shower development particularly in the longitudinal direction; the intercalibration of the energy measurements in the various layers; and corrections of non-uniformities in the calorimeter response.

For $H \to \gamma\gamma$ photons with typical transverse momentum of 60 GeV, the uncertainty on the energy scale ranges from about 0.2% in the central barrel, to about 1.2% in the region neighboring the barrel-endcap transition. The corresponding relative uncertainty on the mass resolution is about 10% for $H \to \gamma\gamma$ and up to ∼50% in the high-mass region. Both the resolution itself and its uncertainty play critical roles in diphoton analyses: the first determines the width of the peaks of narrow resonances, while the second has a direct impact on the signal yield through changes in the width of the peak and constitutes the leading uncertainty on the latter. The resolution uncertainty may be constrained in data using the increasingly well-measured shape of the $H \to \gamma\gamma$ peak, but even with the HL-LHC dataset the uncertainty is expected to still reach $\sim 2 - 3\%$, and will remain a leading contribution to the total uncertainty on the signal yield.

The current calibration was the result of a significant effort and further improvements are expected to be small and incremental. However these would still be worthwhile due to their impact on the analysis. They could focus on five main areas:

- Improved understanding of the material in front of the calorimeter, using the larger datasets from Run-2 and beyond.
- Improved understanding of the cross-talk between calorimeter cells, which can affect the cell-level response.
- Use of more advanced cluster reconstruction methods than the current sliding-window algorithm [52], in particular to reduce out-of-cluster energy leakage.
- Improved MVA calibration algorithm, in particular using a more precise description of the shower shape if the corresponding variables can be well-described in the simulation

following the point below.

- Improvement of the simulation of the interaction of photons with the calorimeter, either through better tuning of the shower models or through a more precise description of the material layout of the calorimeter.

9.4.4 Improvement of Photon Identification

The current photon identification selection is based on simple rectangular cuts on energy and shower-shape variables, with cut values that depend on the photon η but not on its E_T.

The current uncertainties on the selections are already small compared to other sources ($< 1\%$) thanks to the use of data-driven methods to estimate the identification efficiencies, and will need to be reduced only with the very large datasets from HL-LHC.

Gains could however be made in the performance of the selection itself, for instance by increasing the efficiency on signal photons while maintaining the current levels of background rejection. This could be achieved using a more complex selection: the current cut-based selection could for instance be replaced by a multivariate algorithm, and the cut values could be made dependent on photon E_T to better optimize the performance in specific energy ranges.

The use of multivariate algorithms was already attempted in Run-1, but the use of data-driven efficiency measurement techniques proved more difficult than for the cut-based case. Since these techniques are critical in order to achieve sufficiently small systematics uncertainties, adapting them to the multivariate case is an important objective.

In parallel to these improvements, the selection algorithms will need to cope with increasing levels of pileup as one moves towards Run-3 and HL-LHC. Since some of the shower shape variables used in the current selections have distributions sensitive to pileup levels, maintaining the current level of performance will require either appropriate corrections, or the use of alternate variables that are less sensitive.

Very similar issues also affect the photon isolation selections, which could also be improved along similar lines.

Finally, the relatively large fake rate of electrons into photons of $O(1\%)$ (see Section 3.3.2) could be reduced, which could have an impact in particular for complex final states such as $t\bar{t}$ background to $HH \to \gamma\gamma b\bar{b}$. This could be achieved in particular through the optimization of the information relative to the reconstructed tracks pointing towards the electromagnetic cluster.

9.5 Summary

In summary, the project described here is structured along three main directions:

- Measurement of Higgs couplings using the $H \to \gamma\gamma$ channel: the work will involve measurements of both inclusive cross-sections and differential distributions of kinematic variables. It will include incremental improvements to the existing $H \to \gamma\gamma$ analysis, in particular on background modeling, photon calibration and photon identification. The work will start in Run-2 and ultimately extend to the end of the HL-LHC program, but should decrease with time as the analysis reaches a mature stage.

- Search for new resonances in the $\gamma\gamma$ channel: the work will involve extending the existing searches for $\gamma\gamma$ resonances, making use of the same improvements to background modeling,

photon calibration and photon identification as for the previous item. The effort can in principle extend to the end of the HL-LHC but will be most relevant for Run-2, when the accumulation of the first data at 13 TeV will offer immediate prospects for discoveries.

- Search for $HH \to \gamma\gamma b\bar{b}$: the work will initially center on the development of the ITk, and after the Phase-II upgrade shift to the use of the new tracker to isolate the $HH \to \gamma\gamma b\bar{b}$ process. The search for $Hb\bar{b}$ production will constitute an intermediate goal achievable during Run-2. The search for BSM enhancements to $HH \to \gamma\gamma b\bar{b}$ will also be pursued during Run 2 and Run 3.

While the $\gamma\gamma$ signature remains the central focus of the project, it will be utilized along multiple directions that provide complementary ways to probe the presence of new physics at LHC, which should provide at the very least strong constraints on the nature of this new physics by the end of the HL-LHC program.

Bibliography

[1] Flacher, Henning and Goebel, Martin and Haller, Johannes and Hocker, Andreas and Monig, Klaus and Stelzer, Joerg, *Revisiting the Global Electroweak Fit of the Standard Model and Beyond with Gfitter*, Eur. Phys. J. **C60** (2009) p. 543, [Erratum: Eur. Phys. J.C71,1718(2011)], arXiv: 0811.0009 [hep-ph].

[2] Peter W. Higgs, *Broken Symmetries and the Masses of Gauge Bosons*, Phys. Rev. Lett. **13** (1964) p. 508.

[3] F. Englert and R. Brout, *Broken Symmetry and the Mass of Gauge Vector Mesons*, Phys. Rev. Lett. **13** (1964) p. 321.

[4] G. S. Guralnik, C. R. Hagen, and T. W. B. Kibble, *Global Conservation Laws and Massless Particles*, Phys. Rev. Lett. **13** (1964) p. 585.

[5] Lyndon Evans and Philip Bryant, *LHC Machine*, JINST **3** (2008) S08001.

[6] Yves Baconnier et al., *LHC: the Large Hadron Collider accelerator project*, Geneva: CERN, 1993, URL: https://cds.cern.ch/record/257706.

[7] Stephen Holmes, Ronald S Moore, and Vladimir Shiltsev, *Overview of the Tevatron collider complex: goals, operations and performance*, Journal of Instrumentation **6** (2011) T08001, URL: http://stacks.iop.org/1748-0221/6/i=08/a=T08001.

[8] Michael S. Chanowitz, "Probing electroweak symmetry breaking at the SSC (Superconducting Super Collider): A no-lose corollary", *Salt Lake City Meeting. Proceedings: 3rd Regular Meeting (New Series) of the Division of Particles and Fields of the American Physical Society, Salt Lake City, USA, Jan 14-17, 1987*, 1987 p. 593, URL: http://ccdb5fs.kek.jp/cgi-bin/img/allpdf?198704153.

[9] Christopher Hubert Llewellyn Smith, "Physics Prospects at Future colliders", *Proceedings of the XIII International Conference on Physics in Collision, Heidelberg, Germany, June 16-18, 1993*, 1994 p. 291, URL: https://cds.cern.ch/record/397215.

[10] G. Aad et al., *The ATLAS Experiment at the CERN Large Hadron Collider*, JINST **3** (2008) S08003.

[11] S. Chatrchyan et al., *The CMS experiment at the CERN LHC*, JINST **3** (2008) S08004.

[12] Georges Aad et al., *Observation of a new particle in the search for the Standard Model Higgs boson with the ATLAS detector at the LHC*, Phys. Lett. **B716** (2012) p. 1, arXiv: 1207.7214 [hep-ex].

[13] Serguei Chatrchyan et al., *Observation of a new boson at a mass of 125 GeV with the CMS experiment at the LHC*, Phys. Lett. **B716** (2012) p. 30, arXiv: 1207.7235 [hep-ex].

[14] "Measurements of the Higgs boson production and decay rates and constraints on its couplings from a combined ATLAS and CMS analysis of the LHC pp collision data at $\sqrt{s}$ = 7 and 8 TeV", tech. rep. ATLAS-CONF-2015-044, CERN, 2015, URL: https://cds.cern.ch/record/2052552.

[15] The ATLAS Collaboration, *Expected performance of the ATLAS experiment: detector, trigger and physics*, Geneva: CERN, 2009, URL: https://cds.cern.ch/record/1125884.

[16] Giuseppe Degrassi et al., *Higgs mass and vacuum stability in the Standard Model at NNLO*, JHEP **08** (2012) p. 098, arXiv: 1205.6497 [hep-ph].

[17] Morad Aaboud et al., *Search for resonances in diphoton events at $\sqrt{s}$=13 TeV with the ATLAS detector* (2016), arXiv: 1606.03833 [hep-ex].

[18] G. Barbiellini et al., "The Production and Detection of Higgs Particles at LEP", tech. rep. DESY-79-27, ECFA/LEP SSG/9/4, 1979.

[19] John Ellis, Mary K. Gaillard, and Dimitri V. Nanopoulos, *A Historical Profile of the Higgs Boson* (2012), arXiv: 1201.6045 [hep-ph].

[20] John R. Ellis, Mary K. Gaillard, and Dimitri V. Nanopoulos, *A Phenomenological Profile of the Higgs Boson*, Nucl. Phys. **B106** (1976) p. 292.

[21] D. Decamp et al., *ALEPH: A detector for electron-positron annnihilations at LEP*, Nucl. Instrum. Meth. **A294** (1990) p. 121, [Erratum: Nucl. Instrum. Meth.A303,393(1991)].

[22] P. A. Aarnio et al., *The DELPHI detector at LEP*, Nucl. Instrum. Meth. **A303** (1991) p. 233.

[23] K. Ahmet et al., *The OPAL detector at LEP*, Nucl. Instrum. Meth. **A305** (1991) p. 275.

[24] The L3 Collaboration, *The Construction of the L3 Experiment*, Nucl. Instrum. Meth. **A289** (1990) p. 35.

[25] R. Barate et al., *Search for the standard model Higgs boson at LEP*, Phys. Lett. **B565** (2003) p. 61, arXiv: hep-ex/0306033 [hep-ex].

[26] F. Abe et al., *The CDF Detector: An Overview*, Nucl. Instrum. Meth. **A271** (1988) p. 387.

[27] V. M. Abazov et al., *The Upgraded D0 detector*, Nucl. Instrum. Meth. **A565** (2006) p. 463, arXiv: physics/0507191 [physics.ins-det].

[28] "Updated Combination of CDF and D0 Searches for Standard Model Higgs Boson Production with up to 10.0 fb^{-1} of Data", 2012, arXiv: 1207.0449 [hep-ex], URL: http://lss.fnal.gov/cgi-bin/find_paper.pl?conf-12-318.

[29] S. Schael et al., *Precision electroweak measurements on the Z resonance*, Phys. Rept. **427** (2006) p. 257, arXiv: hep-ex/0509008 [hep-ex].

[30] LEP Electroweak Working Group, *Precision Electroweak Measurements and Constraints on the Standard Model* (2010), arXiv: 1012.2367 [hep-ex].

[31] The SLD Collaboration, "SLD Design Report", tech. rep. SLAC-0273, SLAC-273, SLAC-R-0273, SLAC-R-273, 1984.

[32] Tevatron Electroweak Working Group, *Updated Combination of CDF and D0 Results for the Mass of the W Boson* (2009), arXiv: 0908.1374 [hep-ex].

[33] *Combination of CDF and D0 Results on the Width of the W boson* (2010), arXiv: 1003.2826 [hep-ex].

[34] M. Baak et al., *Updated status of the global electroweak fit and constraints on new physics*, The European Physical Journal C **72** (2012) p. 1, ISSN: 1434-6052, URL: http://dx.doi.org/10.1140/epjc/s10052-012-2003-4.

[35] *April 2011 Gfitter results*, URL: http://project-gfitter.web.cern.ch/project-gfitter/Standard_Model/2011_04_30_index.html.

[36] The ATLAS Collaboration, *ATLAS detector and physics performance: Technical Design Report, 2*, Technical Design Report ATLAS, Geneva: CERN, 1999, URL: https://cds.cern.ch/record/391177.

[37] D. Binosi and L. Theussl, *JaxoDraw: A graphical user interface for drawing Feynman diagrams*, Computer Physics Communications **161** (2004) p. 76 , ISSN: 0010-4655, URL: http://www.sciencedirect.com/science/article/pii/S0010465504002115.

[38] Stefan Dittmaier, Michael Kramer 1, and Michael Spira, *Higgs radiation off bottom quarks at the Tevatron and the CERN LHC*, Phys. Rev. **D70** (2004) p. 074010, arXiv: hep-ph/0309204 [hep-ph].

[39] S. Dawson et al., *Exclusive Higgs boson production with bottom quarks at hadron colliders*, Phys. Rev. **D69** (2004) p. 074027, arXiv: hep-ph/0311067 [hep-ph].

[40] R. N. Cahn and Sally Dawson, *Production of Very Massive Higgs Bosons*, Phys. Lett. **B136** (1984) p. 196, [Erratum: Phys. Lett.B138,464(1984)].

[41] Abdelhak Djouadi, *The Anatomy of electro-weak symmetry breaking. I: The Higgs boson in the standard model*, Phys. Rept. **457** (2008) p. 1, arXiv: hep-ph/0503172 [hep-ph].

[42] S. Dittmaier et al., *Handbook of LHC Higgs Cross Sections: 1. Inclusive Observables* (2011), arXiv: 1101.0593 [hep-ph].

[43] M Capeans et al., "ATLAS Insertable B-Layer Technical Design Report", tech. rep. CERN-LHCC-2010-013. ATLAS-TDR-19, CERN, 2010, URL: https://cds.cern.ch/record/1291633.

[44] *ATLAS: letter of intent for a general-purpose pp experiment at the large hadron collider at CERN*, Letter of Intent, Geneva: CERN, 1992, URL: https://cds.cern.ch/record/291061.

[45] D. Banfi, M. Delmastro, and M. Fanti, *Cell response equalisation of the ATLAS electromagnetic calorimeter without the direct knowledge of the ionisation signals*, JINST **1** (2006) P08001.

[46] W. Cleland and E. Stern, *Signal processing considerations for liquid ionization calorimeters in a high rate environment*, Nucl.Instrum.Meth. **A338** (1994) p. 467.

[47] N Berger, L Tran, and J De Vivie, "Improved Q-factor Definition Using Pulse Shape Residuals", tech. rep. ATL-LARG-INT-2014-002, CERN, 2014, URL: https://cds.cern.ch/record/1711188.

[48] Marco Delmastro, *Quality factor analysis and optimization of digital filtering signal reconstruction for liquid ionization calorimeters*, Nucl.Instrum.Meth. **A600** (2009) p. 545, arXiv: 0812.3486 [physics.ins-det].

[49] Georges Aad et al., *Measurement of the photon identification efficiencies withthe ATLAS detector using LHC Run 1 data* (in preparation).

[50] Matteo Cacciari, Gavin P. Salam, and Gregory Soyez, *The Catchment Area of Jets*, JHEP **04** (2008) p. 005, arXiv: 0802.1188 [hep-ph].

[51] Matteo Cacciari, Gavin P. Salam, and Sebastian Sapeta, *On the characterisation of the underlying event*, JHEP **04** (2010) p. 065, arXiv: 0912.4926 [hep-ph].

[52] Georges Aad et al., *Electron performance measurements with the ATLAS detector using the 2010 LHC proton-proton collision data*, Eur. Phys. J. **C72** (2012) p. 1909, arXiv: 1110.3174 [hep-ex].

[53] Georges Aad et al., *Electron and photon energy calibration with the ATLAS detector using LHC Run 1 data*, Eur. Phys. J. **C74** (2014) p. 3071, arXiv: 1407.5063 [hep-ex].

[54] Georges Aad et al., *Measurements of Higgs boson production and couplings in diboson final states with the ATLAS detector at the LHC*, Phys. Lett. **B726** (2013) p. 88, [Erratum: Phys. Lett.B734,406(2014)], arXiv: 1307.1427 [hep-ex].

[55] Georges Aad et al., *Measurement of Higgs boson production in the diphoton decay channel in pp collisions at center-of-mass energies of 7 and 8 TeV with the ATLAS detector*, Phys. Rev. **D90** (2014) p. 112015, arXiv: 1408.7084 [hep-ex].

[56] "Measurements of the properties of the Higgs-like boson in the two photon decay channel with the ATLAS detector using 25 fb^{-1} of proton-proton collision data", tech. rep. ATLAS-CONF-2013-012, CERN, 2013, URL: https://cds.cern.ch/record/1523698.

[57] *The* `LArSampesMon` *Package*, URL: https://twiki.cern.ch/twiki/bin/view/LAr/LArSamplesMon.

[58] *The* `LArCafJobs` *Package*, URL: https://twiki.cern.ch/twiki/bin/view/LAr/LarCafJobs.

[59] Georges Aad et al., *Monitoring and data quality assessment of the ATLAS liquid argon calorimeter*, JINST **9** (2014) P07024, arXiv: 1405.3768 [hep-ex].

[60] Zvi Bern, Lance J. Dixon, and Carl Schmidt, *Isolating a light Higgs boson from the diphoton background at the CERN LHC*, Phys. Rev. **D66** (2002) p. 074018, arXiv: hep-ph/0206194 [hep-ph].

[61] John M. Campbell et al., *Predictions for diphoton production at the LHC through NNLO in QCD*, JHEP **07** (2016) p. 148, arXiv: 1603.02663 [hep-ph].

[62] Stefano Catani et al., *Diphoton production at hadron colliders: a fully-differential QCD calculation at NNLO*, Phys. Rev. Lett. **108** (2012) p. 072001, arXiv: 1110.2375 [hep-ph].

[63] T. Gleisberg et al., *Event generation with SHERPA 1.1*, JHEP **02** (2009) p. 007, arXiv: 0811.4622 [hep-ph].

[64] Torbjorn Sjostrand, Stephen Mrenna, and Peter Z. Skands, *A Brief Introduction to PYTHIA 8.1*, Comput. Phys. Commun. **178** (2008) p. 852, arXiv: 0710.3820 [hep-ph].

[65] Torbjorn Sjostrand, Stephen Mrenna, and Peter Z. Skands, *PYTHIA 6.4 Physics and Manual*, JHEP **05** (2006) p. 026, arXiv: hep-ph/0603175 [hep-ph].

[66] M. Oreglia, "A Study of the Reactions $\psi' \to \gamma\gamma\psi$", PhD thesis: SLAC, 1980, URL: http://www-public.slac.stanford.edu/sciDoc/docMeta.aspx?slacPubNumber=slac-r-236.html.

[67] J. Gaiser, "Charmonium Spectroscopy From Radiative Decays of the J/ψ and ψ'", PhD thesis: SLAC, 1982, URL: http://www-public.slac.stanford.edu/sciDoc/docMeta.aspx?slacPubNumber=slac-r-255.html.

[68] Tomasz Skwarnicki, "A study of the radiative CASCADE transitions between the Upsilon-Prime and Upsilon resonances", PhD thesis: Cracow, INP, 1986, URL: http://lss.fnal.gov/cgi-bin/find_paper.pl?other/thesis/skwarnicki.pdf.

[69] Richard Partridge et al., *The Decay $J/\psi \to 3\gamma$ and a Search for the η_c*, Phys. Rev. Lett. **44** (1980) p. 712.

[70] Georges Aad et al., *Combined Measurement of the Higgs Boson Mass in pp Collisions at $\sqrt{s} = 7$ and 8 TeV with the ATLAS and CMS Experiments*, Phys. Rev. Lett. **114** (2015) p. 191803, arXiv: 1503.07589 [hep-ex].

[71] John C. Collins and Davison E. Soper, *Angular Distribution of Dileptons in High-Energy Hadron Collisions*, Phys. Rev. **D16** (1977) p. 2219.

[72] Georges Aad et al., *Evidence for the spin-0 nature of the Higgs boson using ATLAS data*, Phys. Lett. **B726** (2013) p. 120, arXiv: 1307.1432 [hep-ex].

[73] K. Ackerstaff et al., *Search for anomalous production of dilepton events with missing transverse momentum in e+ e- collisions at $\sqrt{s}$ = 161-GeV and 172-GeV*, Eur. Phys. J. **C4** (1998) p. 47, arXiv: hep-ex/9710010 [hep-ex].

[74] M. Vesterinen and T. R. Wyatt, *A Novel Technique for Studying the Z Boson Transverse Momentum Distribution at Hadron Colliders*, Nucl. Instrum. Meth. **A602** (2009) p. 432, arXiv: 0807.4956 [hep-ex].

[75] Serguei Chatrchyan et al., *Measurement of differential cross sections for the production of a pair of isolated photons in pp collisions at $\sqrt{s} = 7$ TeV*, Eur. Phys. J. **C74** (2014) p. 3129, arXiv: 1405.7225 [hep-ex].

[76] Georges Aad et al., *Observation of a new particle in the search for the Standard Model Higgs boson with the ATLAS detector at the LHC*, Phys. Lett. **B716** (2012) p. 1, arXiv: 1207.7214 [hep-ex].

[77] Georges Aad et al., *Measurements of fiducial and differential cross sections for Higgs boson production in the diphoton decay channel at $\sqrt{s} = 8$ TeV with ATLAS*, JHEP **09** (2014) p. 112, arXiv: 1407.4222 [hep-ex].

[78] J. R. Klein and A. Roodman, *Blind analysis in nuclear and particle physics*, Ann. Rev. Nucl. Part. Sci. **55** (2005) p. 141.

[79] Marco Pieri et al., "Inclusive Search for the Higgs Boson in the $H \to \gamma\gamma$ Channel", tech. rep. CMS-NOTE-2006-112, CERN, 2006, URL: https://cds.cern.ch/record/973112.

[80] Nicolas Berger, Andreas Hoecker, and Bruno Lenzi, "Hfitter : a Statistical Framework for High-Energy Physics Analysis", tech. rep. ATL-COM-PHYS-2016-442, CERN, 2016, URL: https://cds.cern.ch/record/2151063.

[81] Glen Cowan et al., *Asymptotic formulae for likelihood-based tests of new physics*, Eur. Phys. J. **C71** (2011) p. 1554, [Erratum: Eur. Phys. J.C73,2501(2013)], arXiv: 1007.1727 [physics.data-an].

[82] J. Neyman, *Outline of a Theory of Statistical Estimation Based on the Classical Theory of Probability*, Philosophical Transactions of the Royal Society of London. Series A, Mathematical and Physical Sciences **236** (1937) p. 333, ISSN: 00804614, URL: http://www.jstor.org/stable/91337.

[83] L. Lyons, "A Particle Physicist's Perspective on Astrostatistics", *Statistical Challenges in Modern Astronomy IV*, ed. by G. J. Babu and E. D. Feigelson, vol. 371, Astronomical Society of the Pacific Conference Series, Nov. 2007 p. 361.

[84] Plato, *The Republic*.

[85] Harold Jeffreys, *An Invariant Form for the Prior Probability in Estimation Problems*, Proceedings of the Royal Society of London A: Mathematical, Physical and Engineering Sciences **186** (1946) p. 453, ISSN: 0080-4630, eprint: http://rspa.royalsocietypublishing.org/content/186/1007/453.full.pdf, URL: http://rspa.royalsocietypublishing.org/content/186/1007/453.

[86] J. Neyman and E. S. Pearson, *On the Problem of the Most Efficient Tests of Statistical Hypotheses*, Philosophical Transactions of the Royal Society of London A: Mathematical, Physical and Engineering Sciences **231** (1933) p. 289, ISSN: 0264-3952, eprint: http://rsta.royalsocietypublishing.org/content/231/694-706/289.full.pdf, URL: http://rsta.royalsocietypublishing.org/content/231/694-706/289.

[87] M. G. Kendall, A. Stuart, and J. K. Ord, eds., *Kendall's Advanced Theory of Statistics*, New York, NY, USA: Oxford University Press, Inc., 1987, ISBN: 0-195-20561-8.

[88] S. S. Wilks, *The Large-Sample Distribution of the Likelihood Ratio for Testing Composite Hypotheses*, Annals Math. Statist. **9** (1938) p. 60.

[89] Abraham Wald, *Tests of Statistical Hypotheses Concerning Several Parameters When the Number of Observations is Large*, Transactions of the American Mathematical Society **54** (1943) p. 426.

[90] Eilam Gross and Ofer Vitells, *Trial factors or the look elsewhere effect in high energy physics*, Eur. Phys. J. **C70** (2010) p. 525, arXiv: 1005.1891 [physics.data-an].

[91] Ofer Vitells and Eilam Gross, *Estimating the significance of a signal in a multi-dimensional search*, Astroparticle Physics **35** (2011) p. 230 , ISSN: 0927-6505, URL: http://www.sciencedirect.com/science/article/pii/S0927650511001630.

[92] Frederick E James, *Statistical Methods in Experimental Physics; 2nd ed.* Singapore: World Scientific, 2006, URL: https://cds.cern.ch/record/1019859.

[93] Alexander L. Read, *Presentation of search results: The CL(s) technique*, J. Phys. **G28** (2002) p. 2693.

[94] R. Brun and F. Rademakers, *ROOT: An object oriented data analysis framework*, Nucl. Instrum. Meth. **A389** (1997) p. 81.

[95] Bernard Aubert et al., *The BaBar detector*, Nucl. Instrum. Meth. **A479** (2002) p. 1, arXiv: hep-ex/0105044 [hep-ex].

[96] Georges Aad et al., *Search for Scalar Diphoton Resonances in the Mass Range* $65 - 600$ *GeV with the ATLAS Detector in pp Collision Data at* $\sqrt{s} = 8$ *TeV*, Phys. Rev. Lett. **113** (2014) p. 171801, arXiv: 1407.6583 [hep-ex].

[97] Georges Aad et al., *Search for a fermiophobic Higgs boson in the diphoton decay channel with the ATLAS detector*, Eur. Phys. J. **C72** (2012) p. 2157, arXiv: 1205.0701 [hep-ex].

[98] Georges Aad et al., *Search For Higgs Boson Pair Production in the* $\gamma\gamma b\bar{b}$ *Final State using pp Collision Data at* $\sqrt{s} = 8$ *TeV from the ATLAS Detector*, Phys. Rev. Lett. **114** (2015) p. 081802, arXiv: 1406.5053 [hep-ex].

[99] Georges Aad et al., *Measurements of* $W\gamma$ *and* $Z\gamma$ *production in pp collisions at* $\sqrt{s} = 7$ *TeV with the ATLAS detector at the LHC*, Phys. Rev. **D87** (2013) p. 112003, [Erratum: Phys. Rev.D91,no.11,119901(2015)], arXiv: 1302.1283 [hep-ex].

[100] Georges Aad et al., *Search for heavy lepton resonances decaying to a Z boson and a lepton in pp collisions at* $\sqrt{s} = 8$ *TeV with the ATLAS detector*, JHEP **09** (2015) p. 108, arXiv: 1506.01291 [hep-ex].

[101] M Escalier et al., "Search for a Standard Model Higgs boson in the ATLAS experiment on the $H \to \gamma\gamma$ channel", tech. rep. ATL-PHYS-INT-2006-002. ATL-COM-PHYS-2005-054, CERN, 2005, URL: https://cds.cern.ch/record/884673.

[102] Georges Aad et al., *Limits on the production of the Standard Model Higgs Boson in pp collisions at* $\sqrt{s} = 7$ *TeV with the ATLAS detector*, Eur. Phys. J. **C71** (2011) p. 1728, arXiv: 1106.2748 [hep-ex].

[103] Georges Aad et al., *Search for the Standard Model Higgs boson in the two photon decay channel with the ATLAS detector at the LHC*, Phys. Lett. **B705** (2011) p. 452, arXiv: 1108.5895 [hep-ex].

[104] "Search for the Standard Model Higgs boson in the diphoton decay channel with 4.9 fb-1 of ATLAS data at sqrt(s)=7TeV", tech. rep. ATLAS-CONF-2011-161, CERN, 2011, URL: https://cds.cern.ch/record/1406356.

[105] S N Bernstein, *Sur les recherches récentes relatives à la meilleure approximation des fonctions continues par les polynomes*, Comm. Soc. Math. Kharkov **13** (1912/13) p. 1.

[106] HSG1 HSG1 Working Group, "Statistics studies for H to gamma gamma search with 2012 dataset and combined results with the full 2011 dataset", tech. rep. ATL-COM-PHYS-2012-757, CERN, 2012, URL: https://cds.cern.ch/record/1453773.

[107] HSG1 HSG1 Working Group, "Statistics studies for H to gamma gamma search in the full 2011 dataset", tech. rep. ATL-COM-PHYS-2012-732, CERN, 2012, URL: https://cds.cern.ch/record/1453249.

[108] CERN, *New results indicate that new particle is a Higgs boson*, URL: http://home.cern/about/updates/2013/03/new-results-indicate-new-particle-higgs-boson.

[109] M. Baak et al., *The Electroweak Fit of the Standard Model after the Discovery of a New Boson at the LHC*, Eur. Phys. J. **C72** (2012) p. 2205, arXiv: 1209.2716 [hep-ph].

[110] W. Buchmuller and D. Wyler, *Effective Lagrangian Analysis of New Interactions and Flavor Conservation*, Nucl. Phys. **B268** (1986) p. 621.

[111] T. D. Lee, *A Theory of Spontaneous T Violation*, Phys. Rev. D **8** (4 1973) p. 1226, URL: http://link.aps.org/doi/10.1103/PhysRevD.8.1226.

[112] Kaustubh Agashe, Roberto Contino, and Alex Pomarol, *The Minimal composite Higgs model*, Nucl. Phys. **B719** (2005) p. 165, arXiv: hep-ph/0412089 [hep-ph].

[113] J. Charles et al., *Current status of the Standard Model CKM fit and constraints on $\Delta F = 2$ New Physics*, Phys. Rev. **D91** (2015) p. 073007, arXiv: 1501.05013 [hep-ph].

[114] Iain W. Stewart and Frank J. Tackmann, *Theory Uncertainties for Higgs and Other Searches Using Jet Bins*, Phys. Rev. **D85** (2012) p. 034011, arXiv: 1107.2117 [hep-ph].

[115] Shireen Gangal and Frank J. Tackmann, *Next-to-leading-order uncertainties in Higgs+2 jets from gluon fusion*, Phys. Rev. **D87** (2013) p. 093008, arXiv: 1302.5437 [hep-ph].

[116] David L. Rainwater, R. Szalapski, and D. Zeppenfeld, *Probing color singlet exchange in Z + two jet events at the CERN LHC*, Phys. Rev. **D54** (1996) p. 6680, arXiv: hep-ph/9605444 [hep-ph].

[117] The HSG1 Group, "Supporting note for coupling measurements in diphoton channel, for Moriond 2013", tech. rep. ATL-COM-PHYS-2013-094, CERN, 2013, URL: https://cds.cern.ch/record/1510143.

[118] Charalampos Anastasiou et al., *Higgs Boson Gluon-Fusion Production in QCD at Three Loops*, Phys. Rev. Lett. **114** (2015) p. 212001, arXiv: 1503.06056 [hep-ph].

[119] Charalampos Anastasiou et al., *High precision determination of the gluon fusion Higgs boson cross-section at the LHC*, JHEP **05** (2016) p. 058, arXiv: 1602.00695 [hep-ph].

[120] "Measurements of the Higgs boson production and decay rates and constraints on its couplings from a combined ATLAS and CMS analysis of the LHC pp collision data at $\sqrt{s}$ = 7 and 8 TeV", tech. rep. ATLAS-CONF-2015-044, CERN, 2015, URL: https://cds.cern.ch/record/2052552.

[121] J R Andersen et al., *Handbook of LHC Higgs Cross Sections: 3. Higgs Properties* (2013), ed. by S Heinemeyer et al., arXiv: 1307.1347 [hep-ph].

[122] D. Zeppenfeld et al., *Measuring Higgs boson couplings at the CERN LHC*, Phys. Rev. **D62** (2000) p. 013009, arXiv: hep-ph/0002036 [hep-ph].

[123] M. Duhrssen et al., *Extracting Higgs boson couplings from CERN LHC data*, Phys. Rev. **D70** (2004) p. 113009, arXiv: hep-ph/0406323 [hep-ph].

[124] "Observation and study of the Higgs boson candidate in the two photon decay channel with the ATLAS detector at the LHC", tech. rep. ATLAS-CONF-2012-168, CERN, 2012, URL: https://cds.cern.ch/record/1499625.

[125] ATLAS Collaboration, *Historic versions of ATLAS SUSY Summary Plots*, URL: https://atlas.web.cern.ch/Atlas/GROUPS/PHYSICS/CombinedSummaryPlots/SUSY/ATLAS_SUSY_Summary/history.html.

[126] ATLAS Collaboration, *Historic versions of ATLAS Exotics Summary Plots*, URL: https://atlas.web.cern.ch/Atlas/GROUPS/PHYSICS/CombinedSummaryPlots/EXOTICS/ATLAS_Exotics_Summary/history.html.

[127] H.P. Nilles, *Supersymmetry, supergravity and particle physics*, Physics Reports **110** (1984) p. 1 , ISSN: 0370-1573, URL: http://www.sciencedirect.com/science/article/pii/0370157384900085.

[128] H.E. Haber and G.L. Kane, *The search for supersymmetry: Probing physics beyond the standard model*, Physics Reports **117** (1985) p. 75 , ISSN: 0370-1573, URL: http://www.sciencedirect.com/science/article/pii/0370157385900511.

[129] Riccardo Barbieri, *Looking Beyond the Standard Model: The Supersymmetric Option*, Riv. Nuovo Cim. **11N4** (1988) p. 1.

[130] Ulrich Ellwanger, Cyril Hugonie, and Ana M. Teixeira, *The Next-to-Minimal Supersymmetric Standard Model*, Phys. Rept. **496** (2010) p. 1, arXiv: 0910.1785 [hep-ph].

[131] G. C. Branco et al., *Theory and phenomenology of two-Higgs-doublet models*, Phys. Rept. **516** (2012) p. 1, arXiv: 1106.0034 [hep-ph].

[132] John F. Gunion and Howard E. Haber, *The CP conserving two Higgs doublet model: The Approach to the decoupling limit*, Phys. Rev. **D67** (2003) p. 075019, arXiv: hep-ph/0207010 [hep-ph].

[133] Marcela Carena et al., *Impersonating the Standard Model Higgs Boson: Alignment without Decoupling*, JHEP **04** (2014) p. 015, arXiv: 1310.2248 [hep-ph].

[134] Jeonghyeon Song and Yeo Woong Yoon, *Gigantic diphoton rate of heavy Higgs bosons in the aligned two Higgs doublet models with small* $\tan\beta$, Phys. Rev. **D91** (2015) p. 113012, arXiv: 1412.5610 [hep-ph].

[135] A. Djouadi et al., *Fully covering the MSSM Higgs sector at the LHC*, JHEP **06** (2015) p. 168, arXiv: 1502.05653 [hep-ph].

[136] Jeremy Bernon et al., *Scrutinizing the alignment limit in two-Higgs-double models:* m_h *= 125 GeV*, Phys. Rev. **D92** (2015) p. 075004, arXiv: 1507.00933 [hep-ph].

[137] Alexandre Arbey et al., *An update on the constraints on the phenomenological MSSM from the new LHC Higgs results*, Phys. Lett. **B720** (2013) p. 153, arXiv: 1211.4004 [hep-ph].

[138] Genevieve Belanger et al., *Higgs Bosons at 98 and 125 GeV at LEP and the LHC*, JHEP **01** (2013) p. 069, arXiv: 1210.1976 [hep-ph].

[139] Ulrich Ellwanger, *Enhanced di-photon Higgs signal in the Next-to-Minimal Supersymmetric Standard Model*, Phys. Lett. **B698** (2011) p. 293, arXiv: 1012.1201 [hep-ph].

[140] S. F. King, M. Muhlleitner, and R. Nevzorov, *NMSSM Higgs Benchmarks Near 125 GeV*, Nucl. Phys. **B860** (2012) p. 207, arXiv: 1201.2671 [hep-ph].

[141] S. F. King et al., *Discovery Prospects for NMSSM Higgs Bosons at the High-Energy Large Hadron Collider*, Phys. Rev. **D90** (2014) p. 095014, arXiv: 1408.1120 [hep-ph].

[142] Giacomo Cacciapaglia et al., *Searching for a lighter Higgs boson: Parametrization and sample tests*, Phys. Rev. **D91** (2015) p. 015012, arXiv: 1311.5132 [hep-ph].

[143] Jeremy Bernon et al., *Scrutinizing the alignment limit in two-Higgs-doublet models. II.* m_H*=125 GeV*, Phys. Rev. **D93** (2016) p. 035027, arXiv: 1511.03682 [hep-ph].

[144] Jeremy Bernon et al., *Light Higgs bosons in Two-Higgs-Doublet Models*, Phys. Rev. **D91** (2015) p. 075019, arXiv: 1412.3385 [hep-ph].

[145] Jia-Wei Fan et al., *Study of diphoton decays of the lightest scalar Higgs boson in the Next-to-Minimal Supersymmetric Standard Model*, Chin. Phys. **C38** (2014) p. 073101, arXiv: 1309.6394 [hep-ph].

[146] Marcin Badziak, Marek Olechowski, and Stefan Pokorski, *New Regions in the NMSSM with a 125 GeV Higgs*, JHEP **06** (2013) p. 043, arXiv: 1304.5437 [hep-ph].

[147] Kai Schmidt-Hoberg and Florian Staub, *Enhanced $h \to \gamma\gamma$ rate in MSSM singlet extensions*, JHEP **10** (2012) p. 195, arXiv: 1208.1683 [hep-ph].

[148] S. Schael et al., *Search for neutral MSSM Higgs bosons at LEP*, Eur. Phys. J. **C47** (2006) p. 547, arXiv: hep-ex/0602042 [hep-ex].

[149] "Flavor independent search for hadronically decaying neutral Higgs bosons at LEP", *Lepton and photon interactions at high energies. Proceedings, 20th International Symposium, LP 2001, Rome, Italy, July 23-28, 2001*, 2001, arXiv: hep-ex/0107034 [hep-ex], URL: http://weblib.cern.ch/abstract?CERN-L3-NOTE-2703.

[150] Lisa Randall and Raman Sundrum, *A Large mass hierarchy from a small extra dimension*, Phys. Rev. Lett. **83** (1999) p. 3370, arXiv: hep-ph/9905221 [hep-ph].

[151] Georges Aad et al., *Search for high-mass diphoton resonances in pp collisions at $\sqrt{s} = 8$ TeV with the ATLAS detector*, Phys. Rev. **D92** (2015) p. 032004, arXiv: 1504.05511 [hep-ex].

[152] Lance J. Dixon and M. Stewart Siu, *Resonance continuum interference in the diphoton Higgs signal at the LHC*, Phys. Rev. Lett. **90** (2003) p. 252001, arXiv: hep-ph/0302233 [hep-ph].

[153] Stephen Godfrey and Heather E. Logan, *Probe of new light Higgs bosons from bottomonium χ_{b0} decay*, Phys. Rev. **D93** (2016) p. 055014, arXiv: 1510.04659 [hep-ph].

[154] Filippo Sala, *Higgs and flavour as doors to new physics*, Eur. Phys. J. Plus **131** (2016) p. 79, arXiv: 1509.08655 [hep-ph].

[155] Sanghyeon Chang et al., *Higgs potential and hidden light Higgs scenario in two Higgs doublet models*, Phys. Rev. **D92** (2015) p. 075023, arXiv: 1507.03618 [hep-ph].

[156] Duarte Fontes et al., *Undoubtable signs of CP-violation in Higgs boson decays at the LHC run 2*, Phys. Rev. **D92** (2015) p. 055014, arXiv: 1506.06755 [hep-ph].

[157] Ayres Freitas, Susanne Westhoff, and Jure Zupan, *Integrating in the Higgs Portal to Fermion Dark Matter*, JHEP **09** (2015) p. 015, arXiv: 1506.04149 [hep-ph].

[158] Nathaniel Craig et al., *The Hunt for the Rest of the Higgs Bosons*, JHEP **06** (2015) p. 137, arXiv: 1504.04630 [hep-ph].

[159] Brian Batell and Sunghoon Jung, *Probing Light Stops with Stoponium*, JHEP **07** (2015) p. 061, arXiv: 1504.01740 [hep-ph].

[160] Debtosh Chowdhury and Otto Eberhardt, *Global fits of the two-loop renormalized Two-Higgs-Doublet model with soft Z_2 breaking*, JHEP **11** (2015) p. 052, arXiv: 1503.08216 [hep-ph].

[161] Stefan Liebler, *Neutral Higgs production at proton colliders in the CP-conserving NMSSM*, Eur. Phys. J. **C75** (2015) p. 210, arXiv: 1502.07972 [hep-ph].

[162] Vardan Khachatryan et al., *Search for diphoton resonances in the mass range from 150 to 850 GeV in pp collisions at $\sqrt{s} = 8$ TeV*, Phys. Lett. **B750** (2015) p. 494, arXiv: 1506.02301 [hep-ex].

[163] "Search for new physics in high mass diphoton events in 3.3 fb^{-1} of proton-proton collisions at $\sqrt{s} = 13$ TeV and combined interpretation of searches at 8 TeV and 13 TeV", tech. rep. CMS-PAS-EXO-16-018, CERN, 2016, URL: http://cds.cern.ch/record/2139899.

[164] "Search for High-Mass Diphoton Resonances in pp Collisions at sqrt(s)=8 TeV with the CMS Detector", tech. rep. CMS-PAS-EXO-12-045, CERN, 2015, URL: http://cds.cern.ch/record/2017806.

[165] Ulrich Ellwanger and Cyril Hugonie, *A 750 GeV Diphoton Signal from a Very Light Pseudoscalar in the NMSSM* (2016), arXiv: 1602.03344 [hep-ph].

[166] *Publications referring to ATLAS-CONF-2015-081*, URL: http://inspirehep.net/search?ln=en&p=refersto%3Arecid%3A1410174.

[167] John Peoples, *Future Directions of High Energy Physics* (1998), URL: http://cds.cern.ch/record/909241.

[168] Bruce J. King, *Prospects for colliders and collider physics to the 1-PeV energy scale*, AIP Conf. Proc. **530** (2000) p. 86, [,86(1999)], arXiv: hep-ex/0005008 [hep-ex].

[169] Leonard Susskind, *Dynamics of Spontaneous Symmetry Breaking in the Weinberg-Salam Theory*, Phys. Rev. **D20** (1979) p. 2619.

[170] H.P. Nilles, *Supersymmetry, supergravity and particle physics*, Physics Reports **110** (1984) p. 1 , ISSN: 0370-1573, URL: http://www.sciencedirect.com/science/article/pii/0370157384900085.

[171] William A. Bardeen, "On naturalness in the standard model", *Ontake Summer Institute on Particle Physics Ontake Mountain, Japan, August 27-September 2, 1995*, 1995, URL: http://lss.fnal.gov/cgi-bin/find_paper.pl?conf-95-391.

[172] Marco Farina, Duccio Pappadopulo, and Alessandro Strumia, *A modified naturalness principle and its experimental tests*, JHEP **08** (2013) p. 022, arXiv: 1303.7244 [hep-ph].

[173] Kaustubh Agashe, Roberto Contino, and Alex Pomarol, *The Minimal composite Higgs model*, Nucl. Phys. **B719** (2005) p. 165, arXiv: hep-ph/0412089 [hep-ph].

[174] Roberto Contino, Leandro Da Rold, and Alex Pomarol, *Light custodians in natural composite Higgs models*, Phys. Rev. **D75** (2007) p. 055014, arXiv: hep-ph/0612048 [hep-ph].

[175] D Albaneo, "Combined preliminary data on Z parameters from the LEP experiments and constraints on the Standard Model", *27th International Conference on High-energy Physics (ICHEP 94) Glasgow, Scotland, July 20-27, 1994*, 1994, URL: http://preprints.cern.ch/cgi-bin/setlink?base=preprint&categ=cern&id=ppe94-187.

[176] Frank Tackmann et al., *Simplified template cross sections* (2016), URL: https://cds.cern.ch/record/2138079.

[177] Gino Isidori et al., *Pseudo-observables in Higgs physics* (2016), URL: https://cds.cern.ch/record/2138023.

[178] Giampiero Passarino, *Higgs Pseudo-Observables*, Nuclear Physics B - Proceedings Supplements **205-206** (2010) p. 16 , Loops and Legs in Quantum Field Theory: Proceedings of the 10th {DESY} Workshop on Elementary Particle Theory, ISSN: 0920-5632, URL: http://www.sciencedirect.com/science/article/pii/S0920563210001957.

[179] Giuliano Panico and Andrea Wulzer, *The Composite Nambu-Goldstone Higgs*, Lect. Notes Phys. **913** (2016) pp.1, arXiv: 1506.01961 [hep-ph].

[180] A. Djouadi et al., *The post-Higgs MSSM scenario: Habemus MSSM?*, Eur. Phys. J. **C73** (2013) p. 2650, arXiv: 1307.5205 [hep-ph].

[181] Georges Aad et al., *Constraints on new phenomena via Higgs boson couplings and invisible decays with the ATLAS detector*, JHEP **11** (2015) p. 206, arXiv: 1509.00672 [hep-ex].

[182] Steven Weinberg, *Baryon- and Lepton-Nonconserving Processes*, Phys. Rev. Lett. **43** (21 1979) p. 1566, URL: http://link.aps.org/doi/10.1103/PhysRevLett.43.1566.

[183] B. Grzadkowski et al., *Dimension-Six Terms in the Standard Model Lagrangian*, JHEP **10** (2010) p. 085, arXiv: 1008.4884 [hep-ph].

[184] Adam Falkowski et al., *Higgs Basis: Proposal for an EFT basis choice for LHC HXSWG* (2015), URL: https://cds.cern.ch/record/2001958.

[185] Rodrigo Alonso et al., *Renormalization Group Evolution of the Standard Model Dimension Six Operators III: Gauge Coupling Dependence and Phenomenology*, JHEP **04** (2014) p. 159, arXiv: 1312.2014 [hep-ph].

[186] K. A. Olive et al., *Review of Particle Physics*, Chin. Phys. **C38** (2014) p. 090001.

[187] "Prospects for New Physics in Higgs Couplings Studies with the ATLAS Detector at the HL-LHC", tech. rep. ATL-PHYS-PUB-2014-017, CERN, 2014, URL: https://cds.cern.ch/record/1956711.

[188] O.J.P. Ã[[[ERROR FOR PACKAGE inputenc]]]boli et al., *Twin Higgs-boson production*, Physics Letters B **197** (1987) p. 269 , ISSN: 0370-2693, URL: http://www.sciencedirect.com/science/article/pii/0370269387903819.

[189] E.W.N. Glover and J.J. van der Bij, *Higgs boson pair production via gluon fusion*, Nuclear Physics B **309** (1988) p. 282 , ISSN: 0550-3213, URL: http://www.sciencedirect.com/science/article/pii/0550321388900831.

[190] S. Dawson, S. Dittmaier, and M. Spira, *Neutral Higgs-boson pair production at hadron colliders: QCD corrections*, Phys. Rev. D **58** (11 1998) p. 115012, URL: http://link.aps.org/doi/10.1103/PhysRevD.58.115012.

[191] "Prospects for measuring Higgs pair production in the channel $H(\rightarrow \gamma\gamma)H(\rightarrow b\bar{b})$ using the ATLAS detector at the HL-LHC", tech. rep. ATL-PHYS-PUB-2014-019, CERN, 2014, URL: https://cds.cern.ch/record/1956733.

[192] "Higgs pair production at the High Luminosity LHC", tech. rep. CMS-PAS-FTR-15-002, CERN, 2015, URL: https://cds.cern.ch/record/2063038.

[193] The HSG1 Group, J Saxon, and J Adelman, "Search for resonant dihggs and enhanced non-resonant dihiggs production in the $\gamma\gamma b\bar{b}$ channel with 20.3 fb^{-1} of data at $\sqrt{s} = 8$TeV: Supporting Documentation", tech. rep. ATL-COM-PHYS-2014-009, CERN, 2014, URL: https://cds.cern.ch/record/1642374.

[194] Georges Aad et al., *Constraints on non-Standard Model Higgs boson interactions in an effective Lagrangian using differential cross sections measured in the $H \rightarrow \gamma\gamma$ decay channel at $\sqrt{s} = 8TeV$ with the ATLAS detector*, Phys. Lett. **B753** (2016) p. 69, arXiv: 1508.02507 [hep-ex].

[195] Vardan Khachatryan et al., *Observation of the diphoton decay of the Higgs boson and measurement of its properties*, Eur. Phys. J. **C74** (2014) p. 3076, arXiv: 1407.0558 [hep-ex].

[196] "ATLAS Phase-II Upgrade Scoping Document", tech. rep. CERN-LHCC-2015-020. LHCC-G-166, CERN, 2015, URL: https://cds.cern.ch/record/2055248.

[197] *ECFA High Luminosity LHC Experiments Workshop: Physics and Technology Developments Summary submitted to ECFA. 96th Plenary ECFA meeting* (2015), URL: https://cds.cern.ch/record/1983664.

[198] Georges Aad et al., *Performance of pile-up mitigation techniques for jets in pp collisions at $\sqrt{s} = 8$ TeV using the ATLAS detector* (2015), arXiv: 1510.03823 [hep-ex].

[199] P Delebecque et al., "Alpine Pixel Detector Layout", tech. rep. ATL-UPGRADE-PUB-2013-009, CERN, 2013, URL: https://cds.cern.ch/record/1516529.